博士論文

Non-Fermi liquid transport properties near the nematic quantum critical point of $\mathbf{FeSe_{1-x}S_x}$

令和 3 年 9 月

京都大学大学院理学研究科　物理学・宇宙物理学専攻

Huang, WenKai

Abstract

A quantum phase transition is one of the central problems with strongly correlated materials. It has been discussed that quantum fluctuations can become significant when the system is near a quantum critical point (QCP), a point in which a zero-temperature transition occurs through the control of certain nonthermal parameters. It is believed that these quantum fluctuations give rise to the non-Fermi liquid (NFL) behaviors and are responsible for an unconventional superconductivity. Thus, understanding the physics associated with quantum fluctuations is of primary importance.

One canonical example of such QCP is an antiferromagnetic (AFM) QCP, which has been realized in a variety of correlated materials, including heavy fermion compounds, iron-pnictides, and cuprates. Notably, near the putative AFM QCP, the following set of anomalous charge transport behaviors have been universally observed and discussed in terms of NFL behaviors: (i) The resistivity ρ deviates from a typical Fermi liquid behavior ($\rho \propto T^2$, where T is the temperature). Instead, it varies as $\rho \propto T$. Moreover, the T-linear scattering rate $1/\tau$ is often found to be close to the Planckian limit, i.e., $\hbar/\tau = \alpha k_B T$ with $\alpha \sim 1$. (ii) The Hall coefficient exhibits an anomalous temperature dependence. In addition, in certain cases, the cotangent of the Hall angle, $\cot\theta_{\rm H}=\rho_{xx}/\rho_{xy}$, has a simpler temperature dependent form, i.e., $\cot\theta_{\rm H} \propto T^2$. (iii) The magnetoresistance cannot be scaled using the conventional Kohler's rule ($\Delta\rho_{xx}/\rho_{xx}(0) = F(H/\rho_{xx}(0))$, where $\Delta\rho_{xx}(T,H) \equiv \rho_{xx}(T,H) - \rho_{xx}(T,0)$ and the function $F(x)$ is related to the Fermi surface). Instead, modified Kohler's scaling is observed, i.e., $\Delta\rho_{xx}/\rho_{xx}(0) \propto \tan^2\theta_{\rm H}$.

In this study, we focus on another type of QCP, i.e., a QCP of a nematic order that breaks the rotational symmetry of the underlying crystal lattice. The presence of the nematic order in many families of unconventional superconductors has been

extensively reported, implying the close relationship between the nematic order and superconductivity. However, in most materials, the nematic order coexists with the other forms of ordered phase, such as the AFM order, making it difficult to determine the effect of nematic fluctuations under both normal and superconducting states.

From this perspective, the iron-based superconductor $FeSe_{1-x}S_x$ is unique. The $FeSe_{1-x}S_x$ is a multiband compound without a magnetic order. For $x = 0$, a nematic order appears at below $T_s \sim 90$ K. As the sulfur doping increases, the transition temperature T_s decreases, and finally reaches zero at the critical doping $x_c \sim 0.17$. At approximately x_c, the elastoresistance measurements reveal that nematic fluctuations diverge toward $T = 0$ K, indicating the presence of a nematic QCP. In addition, the nuclear magnetic resonance measurements on the spin-lattice relaxation rate suggest that the AFM fluctuations are suppressed by the S-doping and no sizable AFM fluctuations are observed near the nematic QCP.

To investigate how the nematic fluctuations affect the transport properties, we measured the dc-resistivity, Hall effect, and magnetoresistance at various doping levels across the nematic QCP of $FeSe_{1-x}S_x$. At approximately $x_c \sim 0.17$, we found that the resistivity shows a linear dependence at low temperatures, and the associated scattering rate is close to the Planckian limit. The cotangent of the Hall angle, $\cot\theta_{\rm H}=\rho_{xx}/\rho_{xy}$, is proportional to T^2. Moreover, the low-field magnetoresistance obeys a modified version of Kohler' s rule. Because this set of transport behaviors are pronounced near the nematic QCP and cannot be reproduced through a conventionally compensated two-band model, we speculate that the critical nematic fluctuations are responsible for the observed behaviors. It should be noted that the AFM fluctuations can also lead to similar anomalous transport behaviors. However, different from the AFM fluctuations with finite momentum $\boldsymbol{q}_{\rm AF}$, the nematic fluctuations are peaked at $\boldsymbol{q}_{\rm nem} \approx 0$. It remains an open question how the critical fluctuations with $\boldsymbol{q}_{\rm nem} \approx 0$ result in this set of NFL behaviors. A common set of anomalous charge transport properties observed in strongly correlated electron systems having essentially different types of critical fluctuations appear to capture a universal feature of the NFL transport properties near the QCP.

Contents

1

Introduction

1.1 Fermi liquids

Understanding the behavior of interacting electrons at low temperature is an important subject in condensed matter physics. In 1957, Landau proposed a phenomenological theory to describe the properties of liquid ^{3}He [1]. It was soon realized that this theory can also be applied to the electrons in solids. It has since become our basis for understanding metals. As one successful aspect of this theory, it explains why the interacting electrons in conventional metals can be treated as free electrons.

The answer rests on the concept of quasiparticles [2–4]. In this theory, Landau imagined an adiabatic evolution from a non-interacting to an interacting electron system. He argued that there will be a one-to-one correspondence between the low-energy excited states of non-interacting and interacting systems. Therefore, the elementary excitations of an interacting system can be marked with quantum numbers (such as the moment $\boldsymbol{k}$) of corresponding non-interacting excitations. These low-energy elementary excitations are called quasiparticles.

As a result of interactions between electrons, a single quasiparticle has a set of renormalized parameters, such as the mass of a quasiparticle, which is renormalized from the band mass to the value of m^*. In addition, excited quasiparticles can interact

with each other, which Landau included in an effective two-particle interaction function $f(\boldsymbol{k}, \boldsymbol{k}')$. Hence, the energy of a single quasiparticle is now expressed as

$$\tilde{\epsilon}_{\boldsymbol{k}} = \epsilon_{\boldsymbol{k}} + \sum_{\boldsymbol{k}'} f(\boldsymbol{k}, \boldsymbol{k}')\delta n_{\boldsymbol{k}'}. \tag{1.1}$$

Here, $\epsilon_{\boldsymbol{k}} = \hbar^2\boldsymbol{k}^2/2m^*$, and $\delta n_{\boldsymbol{k}} = n_{\boldsymbol{k}} - n^0_{\boldsymbol{k}}$ is the change in the distribution function with respect to the ground state (where $n^0_{\boldsymbol{k}}$ is the Fermi distribution function).

Eq. 1.1 can be used to calculate many different thermodynamic properties, including the electronic specific heat C_e and Pauli susceptibility χ, which are given by

$$C_e = \frac{\pi^2 N^*(E_F)}{3} k_B^2 T = \gamma_e T, \tag{1.2}$$

$$\chi_{\text{Pauli}} = \frac{\mu_B^2 N^*(E_F)}{1 + F_0^a}, \tag{1.3}$$

respectively. Here, $N^*(E_F) = m^* k_F/(\pi^2\hbar^2)$ is the normalized density of state at the Fermi energy, and F_0^a is a Landau parameter related to the interaction function $f(\boldsymbol{k}, \boldsymbol{k}')$. These expressions are similar to those for a free electron gas but have modified parameters that reflect the effects of the interactions.

One scaling relation can be derived from Eqs. 1.2 and 1.3, namely, the ratio of specific heat coefficient γ_e to Pauli susceptibility χ_{Pauli}, which is often referred to as the Wilson ratio:

$$R = \frac{\chi_{\text{Pauli}}}{\gamma_e} \frac{\pi^2 k_B^2}{\mu_0 \mu_{eff}^2} = \frac{1}{1 + F_0^a}. \tag{1.4}$$

As seen from the formula, this ratio reflects the strength of quasiparticle interactions. In the case of non-interacting metals, the ratio R is close to 1. By contrast, for the correlated Fermi liquids, R can be larger than unity. For example, in heavy fermion compounds, $R \sim 2$ is widely observed.

1.2 Quantum phase transition

Despite the success in describing many conventional metals, Fermi liquid theory fails to apply in many strongly correlated materials. In particular, this breakdown of a Fermi liquid description has often been observed within the vicinity of a quantum phase transition (QPT). Therefore, the physics of such a transition have been extensively studied [5–8].

Unlike the classical finite temperature phase transition, the QPT is a zero-temperature transition that occurs by varying a non-thermal parameter g (e.g., pressure or chemical doping). In this case, the ordered phase is destroyed by quantum rather than thermal fluctuations. For a continuous QPT, the point where it takes place is called the quantum critical point (QCP). Near the QCP, the critical quantum fluctuations of the ordered parameter are expected to be large. The associated order parameter correlation length ξ and correlation time ξ_τ diverge as

$$\xi \propto |g - g_c|^{-\nu}, \xi_\tau \propto |g - g_c|^{-\nu z}, \tag{1.5}$$

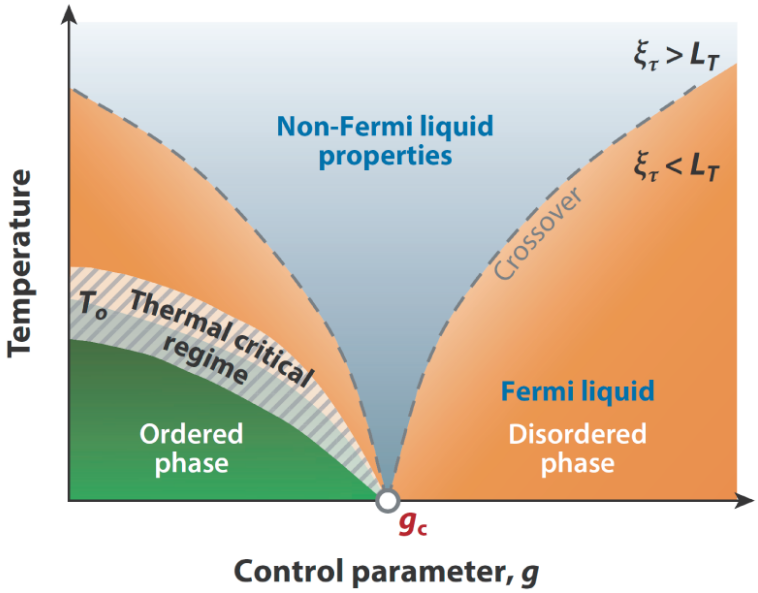

Figure 1.1: Phase diagram near a QCP [5].

where v and z are the correlation length and dynamical exponent of the quantum phase transition, respectively.

Although the QCP is located at absolute zero, its influence can extend up to a finite temperature. Fig. 1.1 shows the typical phase diagram. The disordered phase is divided into two regimes: $\xi_\tau > L_\tau$ and $\xi_\tau < L_\tau$. Here, $L_\tau = \hbar/k_B T$ is the thermal timescale, which characterizes the thermal fluctuations (i.e., thermal length along the imaginary time axis). As ξ_τ diverges when approaching the QCP, it is clear that the boundary line can have a funnel-like shape. The two separate regimes are characterized by distinct temperature dependent behaviors. In the regime where $\xi_\tau < L_\tau$, the physical quantities can be described by the ground state wave function. The metallic systems in this region show conventional Fermi liquid behaviors. By contrast, in the regime where $\xi_\tau > L_\tau$, i.e., the so-called quantum critical regime, the physical quantities exhibit unusual power law temperature dependencies which are influenced by the QCP. For example, in a two-dimensional system, the electronic specific heat coefficient γ_e shows a divergent behavior, $\gamma_e = C_e/T \propto \log T$.

The problem of quantum criticality has been studied in many correlated materials, including heavy fermion compounds, iron-pnictides and cuprates. Fig. 1.2 shows several examples, most of which are related to the AFM phase. For both $CeRhIn_5$ and $BaFe_2(As_{1-x}P_x)_2$, the NFL properties are observed near the end point of the AFM order, indicating the development of critical AFM fluctuations near the QCP. More significantly, the superconducting phase is stabilized when the AFM order is suppressed. This fact suggests the unconventional superconductivity caused by the AFM fluctuations.

For the cuprate superconductors, the situation is somehow different. In most phase diagrams of hole-doped cuprates (Fig. 1.2c), the AFM phase is outside the superconducting dome. Instead, the highest T_c and NFL behaviors are often observed near the end of the so-called pseudogap regime, which is characterized by a reduction of the density of states (DOS). Although the origin of a pseudogap is still controversial, some experiments have shown evidence of the rotational or time-reversal symmetries breaking inside this regime. These results appear to support the idea that some sort of QCP

is present inside the superconducting dome.

Figure 1.2d shows the phase diagram of the system studied in this thesis, i.e., iron chalcogenides $FeSe_{1-x}S_x$. Differing from previous examples, this system has a nematic phase without a magnetic order at ambient pressure. By substituting with sulfur, one can access the nematic QCP at $x_c \sim 0.17$. This fact promotes the interest in investigating the physics related to the critical nematic fluctuations. In the following sections, iron-based superconductors will be briefly reviewed. We will then discuss the physical properties of $FeSe_{1-x}S_x$.

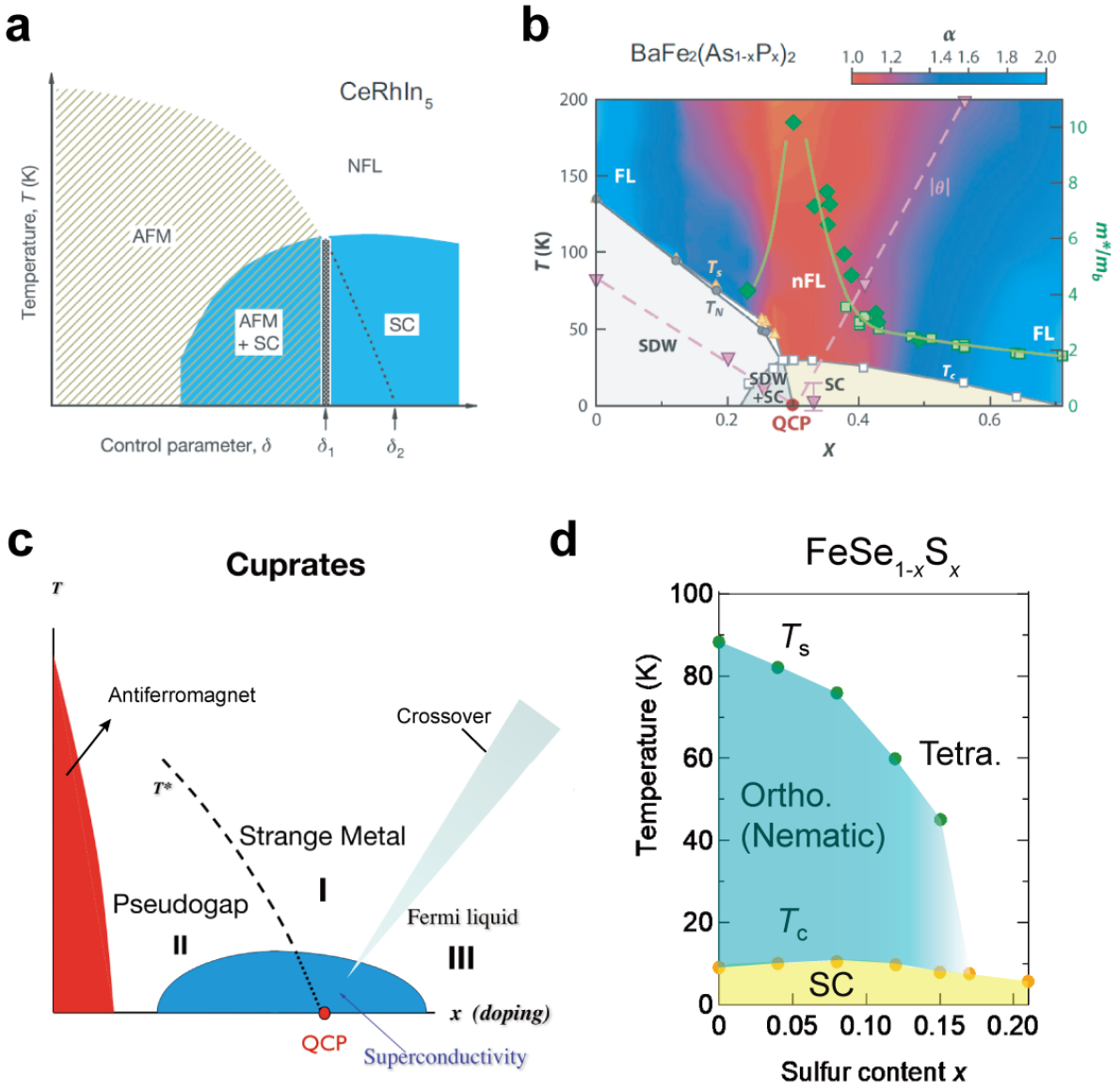

Figure 1.2: Phase diagrams of $CeRhIn_5$ [9], $BaFe_2(As_{1-x}P_x)_2$ [5], cuprates [10], and $FeSe_{1-x}S_x$ [11].

1.3 Iron-based superconductors

The first iron-based superconductor, iron-pnictide LaFePO ($T_c \approx 6$ K), was reported by Hosono's group in 2006 [12]. However, it was the discovery of high T_c in LaFeAs(O,F) in 2008 that attracted significant interest, particularly when it was found that T_c can reach 43 K by applying pressure, and an even higher temperature ($T_c \approx 56$ K) by substituting La with another lanthanoid element. Since then, this class of materials has become a new family of high-T_c superconductor.

1.3.1 Crystal structure

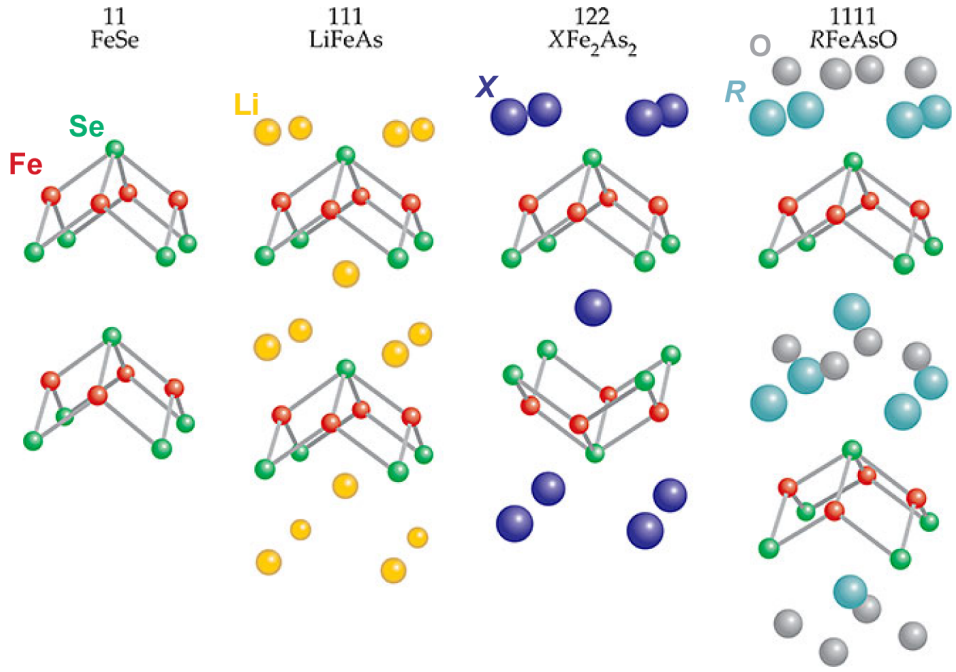

Figure 1.3: Crystal structures of four typical families of iron-based superconductors [13]. Here, X and R represent alkali earth and rare earth elements, respectively.

Thus far, a number of iron-based superconductors have been reported. These materials commonly contain Fe-pnictide(Pn)/chalcogenide(Ch) layers, in which the Pn or Ch atoms sit alternatively above and below the Fe square lattice centers. Fig. 1.3 shows four major types of iron-based superconductors, which are referred to as the 11, 111,

122, or 1111 series based on the ratio of the constituent elements of their parent compounds. The main structural difference between these families comes from the spacer layers added between the Fe-Pn/Ch layers. For example, for 122 families, the spacer layers consist of a single X atomic layer, whereas for 111 families, the spacer layers are the double layers of alkali ions. Note that the 11 family has no spacer layer. Therefore, this family is structurally the simplest among iron-based superconductors.

1.3.2 Electronic structure

The electronic structures of iron-based superconductors at low energies have been well investigated both theoretically and experimentally. For most iron-based superconductors, the Fermi surfaces are similar. They consist of hole pockets at the BZ center (Γ point) and electron pockets at the BZ corner (M point). The dominant orbital characters near the Fermi energy come from the $3d$ orbitals of the Fe^{2+} ions with a $3d^6$ configuration. As an example, we show the electronic structure of NaFeAs predicted by the local density approximation (LDA) calculations in Fig. 1.4. As with other iron pnictides, the hole and electron pockets are well separated and their main orbital characters are d_{xz}, d_{yz}, and d_{xy}. Depending on the materials, the shape, number, and orbital characteristics of the pockets can differ.

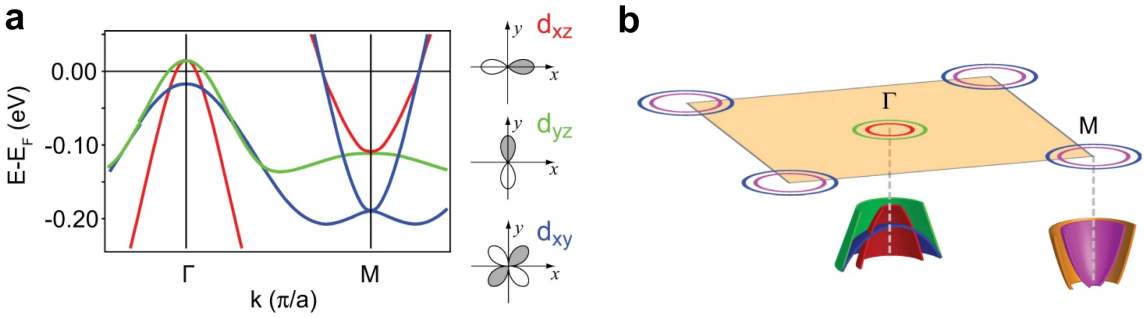

Figure 1.4: Electronic structures of NaFeAs calculated using LDA method [14].

One notable feature of this band structure is the quasi-nesting of the hole and electron pockets. If the hole pockets are inverted and then shifted by a vector $\boldsymbol{Q} = (\pi, \pi)$

(2-Fe BZ), we expect that the hole and electron pockets will partially overlap, i.e.,

$$\varepsilon_e(\boldsymbol{k}_{hs}) = -\varepsilon_h(\boldsymbol{k}_{hs} + \boldsymbol{Q}). \tag{1.6}$$

This situation is called Fermi surface nesting, and Fermi surface spots satisfying such condition are called hot spots. It has been pointed out that such nesting can enhanced the susceptibility at wave vector $\boldsymbol{Q}$ at low temperatures. To qualitatively understand this point, one can consider the limit of perfect nesting, in which one hole and one electron pocket have the relation $\varepsilon_e(\boldsymbol{k}) = -\varepsilon_h(\boldsymbol{k} + \boldsymbol{Q}) = \boldsymbol{k}^2/2m^*$. The real part of the spin susceptibility (without interactions) can then be given by

$$\chi_0'(\boldsymbol{q}, \omega = 0) = \frac{m^*}{\pi} \log|\frac{\Lambda}{\boldsymbol{q} - \boldsymbol{Q}}|, \tag{1.7}$$

where Λ is the bandwidth [15]. The spin susceptibility diverges as $\boldsymbol{q}$ approaches $\boldsymbol{Q}$. It has been pointed out that such an enhancement of the spin susceptibility can give rise to an AFM phase and is a candidate for providing unconventional superconducting pairing interaction [16, 17].

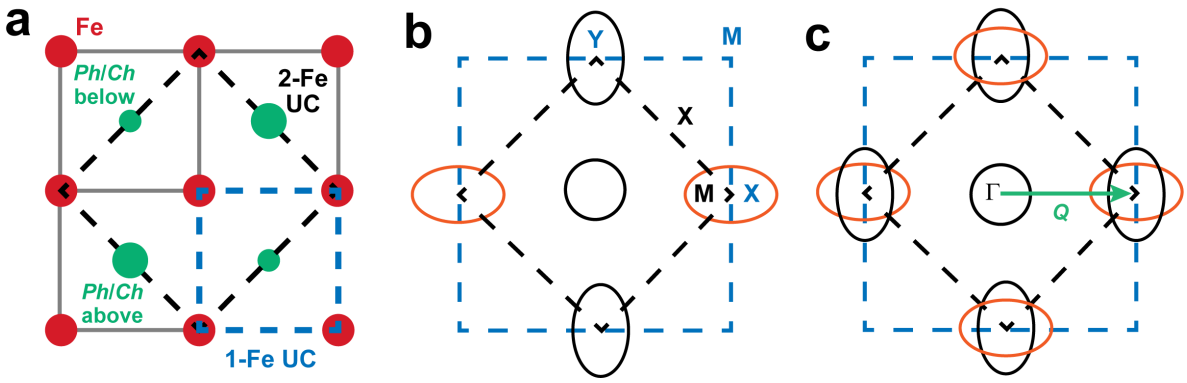

Figure 1.5: **a** Top view of Fe-Pn/Ch plane. The 1-Fe and 2-Fe unit cells are outlined with blue and black dotted lines, respectively. **b** The Fermi pockets in 1-Fe BZ. The X point of 1-Fe BZ corresponds to the M point of 2-Fe BZ. **c** The Fermi pockets in 2-Fe BZ. The green arrow indicates the nesting wave vector $\boldsymbol{Q}$=(π,π).

Finally, we discuss two BZs frequently used when describing the electronic structure in iron-based superconductors. Fig. 1.5a shows a top view of a common Fe-Pn/Ch layer.

The crystallographic unit cell will have two Fe atoms because of the two inequivalent positions of Pn/Ch atoms. Typically, one should employ the BZ corresponding to this 2-Fe unit cell. However, for simplicity, many theoretical calculations employ a BZ corresponding to 1-Fe unit cell (see Fig. 1.5a). This is allowed because only Fe d states dominate the low-energy excitations. In such a case, the BZ becomes twice as large as the 2-Fe BZ. The reproduced Fermi surfaces are shown in Fig. 1.5.

1.3.3 Phase diagram

The iron-based superconductors show the complex interplay between various ordered states by chemical doping or pressure. Fig. 1.6 shows the typical phase diagram for the iron-pnictides, which includes the three most common phases, i.e., magnetic, nematic, and superconducting phases. Most parent compounds of iron-based superconductors have an AFM phase. Slightly above or at the AFM transition temperature T_{N}, a tetragonal to orthorhombic structural transition always occurs. Both phases can be tuned by chemical doping or applying pressure. Superconductivity emerges when the AFM and structural transitions are suppressed.

Magnetic order

For most iron-based superconductors, the magnetic structure is a stripe type, i.e., the spins on the Fe sites are arranged ferromagnetically along one Fe-Fe bond direction and antiferromagnetically along the other. This AFM order has a wave vector (π,π) in the tetragonal (2-Fe) unit cell, which coincides with the nesting wave vector $\boldsymbol{Q}$ (see subsection 1.3.2). In itinerant electrons, the magnetic state arises from the instability caused by this (π,π) Fermi surface nesting.

Nematic order

The electronic state associated with the structural tetragonal-to-orthorhombic transition is another interesting phase in iron-based superconductors. The results of transport, angle resolved photoemission spectroscopy (ARPES), and scanning tunnelling

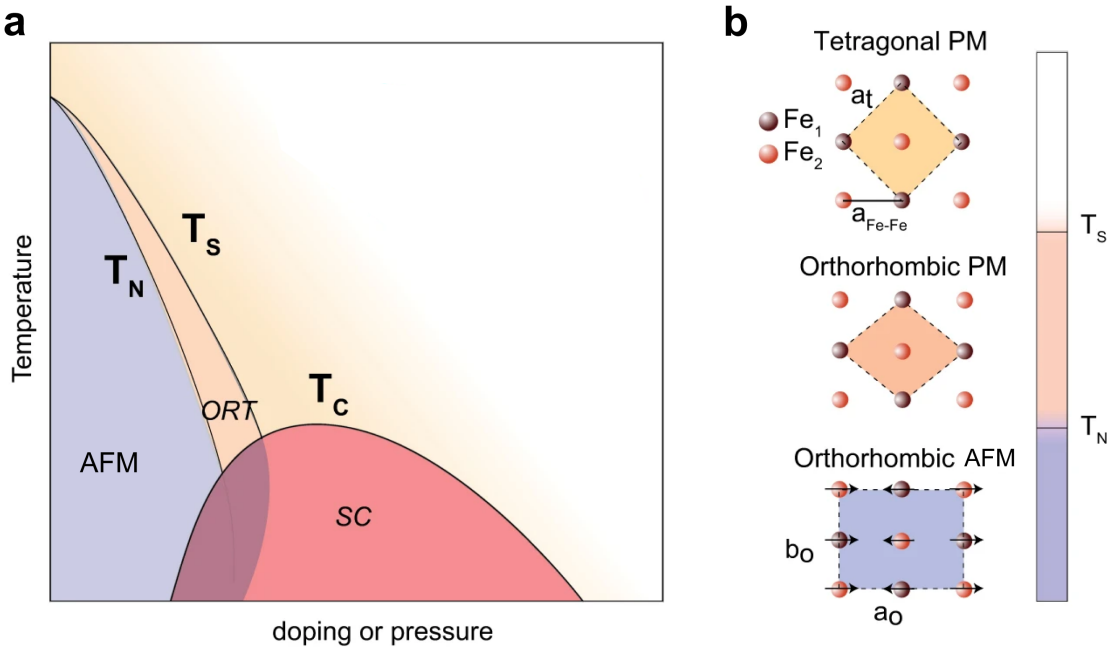

Figure 1.6: **a** Typical phase diagram for iron-pnictides. **b** The crystal and magnetic structures in each phase. Two inequivalent positions of Fe atoms are marked with different colors. For convenience, the Ph/Ch atoms are not shown. In the orthorhombic AFM order, the spins on the Fe sites are arranged ferromagnetically along the b_o direction and antiferromagnetically along the a_o direction ($a_o > b_o$). Adapted from Ref. [14].

microscopy (STM) measurements have revealed large in-plane electronic anisotropy in an orthorhombic structure [18, 19]. This anisotropy breaks the rotational symmetry while preserving the translation symmetry of the tetragonal crystal lattice and is thus called an electronic nematic state. It has been argued that a small lattice distortion cannot explain the large electronic anisotropy observed through experiments. Furthermore, the magnetic torque measurements in a series of isoelectronic substituted $BaFeAs_{1-x}P_x$ samples showed evidence of electronic nematicity well above the structural transition temperature T_s [20]. These observations suggest that the structural transition in most iron-based superconductors is actually driven by the electronic degree of freedom. This is important because the same electron-electron correlation mechanism might also lead to superconductivity and magnetism.

The origin of the electronic nematic order has been discussed in terms of the critical

magnetic and orbital fluctuations [21]. In the former image, the nematic order is the result of an unequal development of thermal spin fluctuations, which peaks unequally at two possible stripe ordering wave vectors $\boldsymbol{Q}_X = (\pi, 0)$ and $\boldsymbol{Q}_Y = (0, \pi)$ (1-Fe BZ) within the temperature range $T_{\rm nem} < T < T_{\rm N}$. It has been argued that this is the most likely scenario for iron-pnictides, where $T_{\rm s}$ and $T_{\rm N}$ are close to each other in the phase diagram [22, 23]. By contrast, in an orbital-driven image, the nematic state is a consequence of orbital ordering [24], in which the occupations of d_{xz} and d_{yz} orbitals differ. This scenario has been suggested for the nematicity in FeSe [23, 25], which does not exhibit a magnetic order at ambient pressure.

Critical fluctuation mediated superconductivity

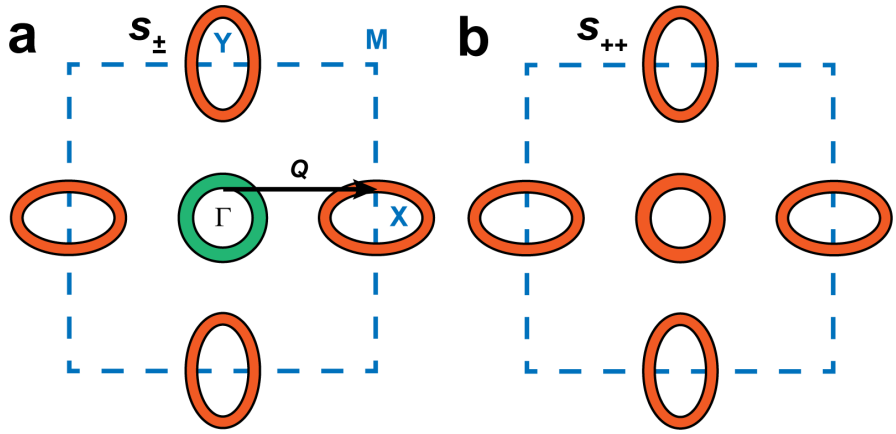

Figure 1.7: The superconducting gap structures of **a** $s_{\pm}$-wave and **b** s_{++}-wave represented in 1-Fe BZ. The green and orange colors are used to emphasize that the signs of these gaps differ.

As shown in the phase diagram, the superconductivity emerges when the AFM and nematic order are suppressed. In addition, the maximum $T_{\rm c}$ is located near the putative AFM and nematic QCPs. These imply that the AFM and the nematic fluctuations will have an important impact on the superconducting pairing. Indeed, most of the discussed superconducting gap structures are related to these fluctuations. Fig. 1.7 shows two typical examples, i.e., $s_{\pm}$ and s_{++} gap structures. In the case of the $s_{\pm}$ state, the spin-fluctuations enhanced through the nesting effect provide strong repulsive interpocket

interactions with wave vector $\boldsymbol{Q} = (\pi, \pi)$ (2-Fe BZ), leading to a gapped $s_{\pm}$ structure with the opposite signs between the hole and electron pockets. By contrast, the s_{++} gap structure arises from orbital fluctuations that are enhance by the Fe phonons. In this case, an interpocket interaction is attractive. One important characteristic of this gap structure is its robustness against impurities. It has been discussed that an impurity-sensitive $s_{\pm}$ state can evolve smoothly into an s_{++} state as the doping concentration increases [26].

In this context, experimentally identifying the role of the nematic and AFM fluctuations is crucial to unveiling the unconventional superconductivity in iron-based superconductors. From this perspective, studying the nature of pure nematic fluctuations in the $FeSe_{1-x}S_x$ system is important.

1.4 Physical properties of FeSe

We now turn to the parent compound of the $FeSe_{1-x}S_x$ system, i.e., FeSe. The nematicity in FeSe has many distinct features compared to iron-pnictides. As the most pronounced aspect, the nematic phase in FeSe is not accompanied by the magnetic order. Moreover, the superconductivity in FeSe shows orbital selective characteristics. In this section, the physical properties of this interesting material are introduced.

1.4.1 Crystal structure

The high-temperature crystal structure of FeSe is shown in Fig. 1.8. It consists of stacked Se-Fe-Se triple layers without any spacer layer between them. The unit cell (Fig. 1.8a) contains two Fe and two Se atoms and has the tetragonal symmetry with space group $P4/nmm$. The lattice constants are $a_{\mathrm{T}} = b_{\mathrm{T}} = 3.77$ Å $< c_{\mathrm{T}} = 5.52$ Å at room temperature [27]. As the temperature decreases, FeSe exhibits a tetragonal-to-orthorhombic structure (space group $Cmma$, $a \neq b$) transition at $T_{\mathrm{s}} \sim 90$ K. The associated lattice distortion $\delta = (a_{\mathrm{OR}} - b_{\mathrm{OR}})/(a_{\mathrm{OR}} + b_{\mathrm{OR}})$ evolves continuously when crossing T_{s}, suggesting a second-order phase transition (Fig. 1.9a) [28]. In the orthorhombic phase, a larger unit cell containing 4 Fe atoms is adopted (Fig. 1.8b). The lattice constants are $a_{\mathrm{OR}} = 5.31$ Å, $b_{\mathrm{OR}} = 5.33$ Å and $c_{\mathrm{OR}} = 5.48$ Å at 5 K [29]. Fig. 1.9b shows an STM image of the FeSe surface measured at ~ 0.4 K [30]. The bright spots are the topmost Se atoms. However, because the orthorhombic distortion is too small ($\delta < 0.3\%$), it is difficult to distinguish the structure anisotropy from the image.

One important feature associated with the tetragonal-to-orthorhombic structure transition is the formation of twin domains. Fig. 1.9c shows the schematic atomic structure near a boundary where the two orthorhombic domains meet (twin boundary). As shown, one domain is rotated by $\pi/2$ when crossing the boundary. For the non-local probes, such as the ARPES and resistivity measurements, the measured quantities are averaged over these domains. Therefore, care must be taken when explaining these data.

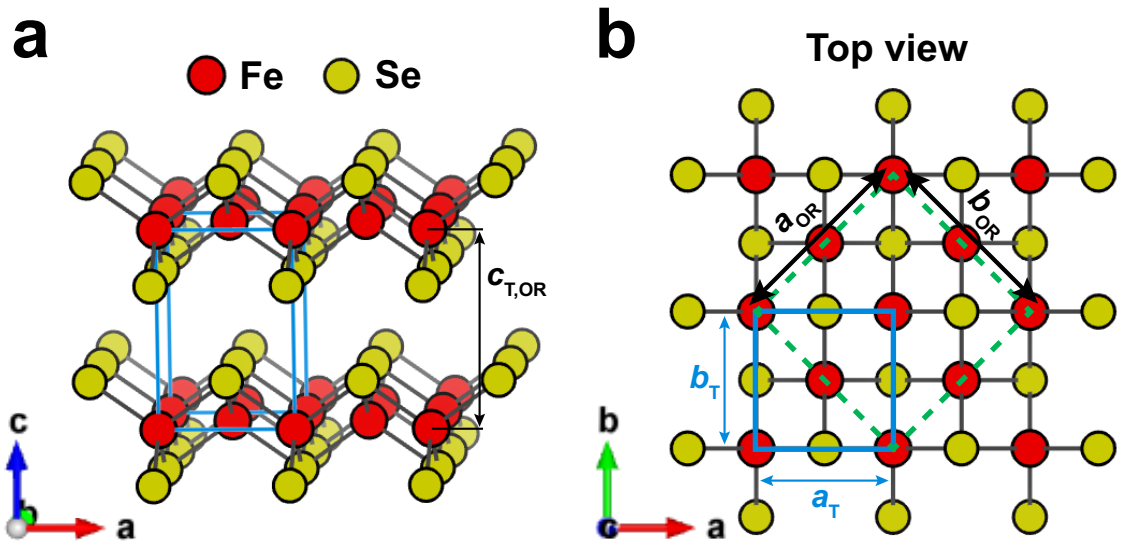

Figure 1.8: Crystal structure of FeSe in the tetragonal phase. **a** Three-dimensional view of FeSe. The tetragonal unit cell is outlined with the blue line. The lattice constants are $a_{\mathrm{T}} = b_{\mathrm{T}} = 3.77$ Å $< c_{\mathrm{T}} = 5.52$ Å. **b** Top view of FeSe. The green dashed line outlines the $Cmma$ unit cell used in the orthorhombic phase. The corresponding lattice constants are $a_{\mathrm{OR}} = 5.31$ Å, $b_{\mathrm{OR}} = 5.33$ Å and $c_{\mathrm{OR}} = 5.48$ Å at 5 K.

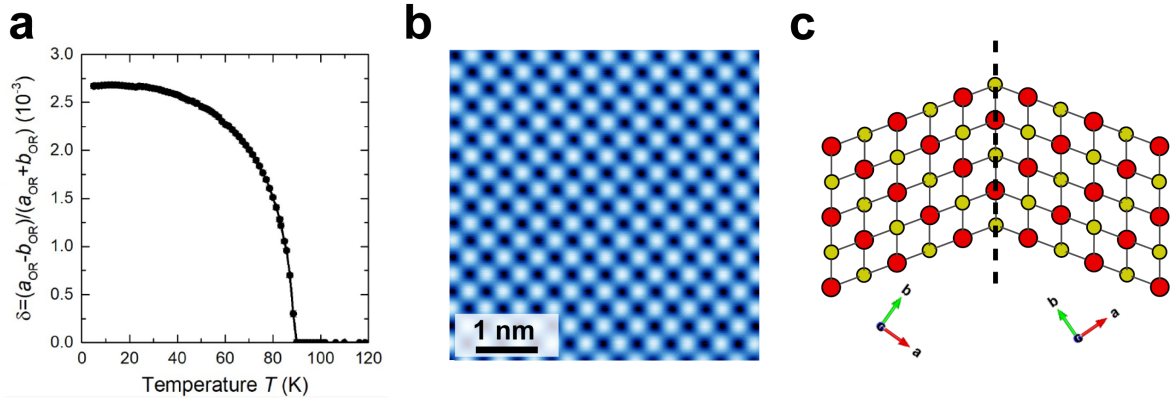

Figure 1.9: **a** The lattice distortion $\delta = (a_{\mathrm{OR}} - b_{\mathrm{OR}})/(a_{\mathrm{OR}} + b_{\mathrm{OR}})$ of FeSe, determined from the X-ray diffraction data, plotted as a function of the temperature [28]. **b** STM images of the FeSe surface measured at ~ 0.4 K [30]. The bright spots represent the Se atoms. **c** Crystal structure near the twin boundary.

1.4.2 Band structure

Broadly speaking, the electronic structure of FeSe is similar to the iron-pnictides in the following ways: (i) It consists of hole pockets at the BZ center and compensating electron pockets at the BZ corner. (ii) The bands within the vicinity of the Fermi level have mainly d_{xy},d_{yz} and d_{xz} orbital characters. The notable characteristics are its extremely small Fermi surface size and Fermi energy. Compared with the density functional theory (DFT) calculation, the measured Fermi surface size is much smaller, and the band dispersion is significantly renormalized. In addition, the small Fermi energy is often found to be on par with the other energy scales, such as the superconducting gap, leading to many exotic states, such as the superconducting state in the Bardeen-Cooper-Schrieffer (BCS) to Bose-Einstein condensation (BEC) crossover regime [30]. In this subsection, experimental evidence regarding these electronic structure properties is introduced.

The Fermi surface of FeSe has been demonstrated in a number of ARPES measurements. Fig. 1.10a-d shows the ARPES data for the twinned FeSe [31]. In the tetragonal phase, there are two circular hole pockets and two elliptical electron pockets. When entering the orthorhombic phase, these pockets heavily distort. The cross-section area of each pocket is extremely small, which equals 1%−3% of the total BZ [11, 32]. Figs. 1.10c and d show the dispersion of the electron and hole pockets along the k_z-direction, respectively. The cylinder-like k_z-dependence of both pockets indicates the quasi-two-dimensional nature of the Fermi surface. Note that the Fermi surface shown here are averaged over two orthorhombic domains (Fig. 1.9c), leading to uncertainty in explaining the data. Hence, ARPES measurements have also been conducted on detwinned samples [33–35]. As shown in Fig. 1.10e, elongated hole and electron pockets are observed at the Γ and Y points, respectively, breaking the 4-fold symmetry. Interestingly, the other electron pocket at point Y, which has been proposed to exist within various schemes (Figs. 1.10f and 1.16d), is not detected. This is an open question at present, and the shape of the pocket at both points Y and X also remains uncertain. Fig. 1.10f shows one proposed Fermi surface in the nematic phase. It has been pointed

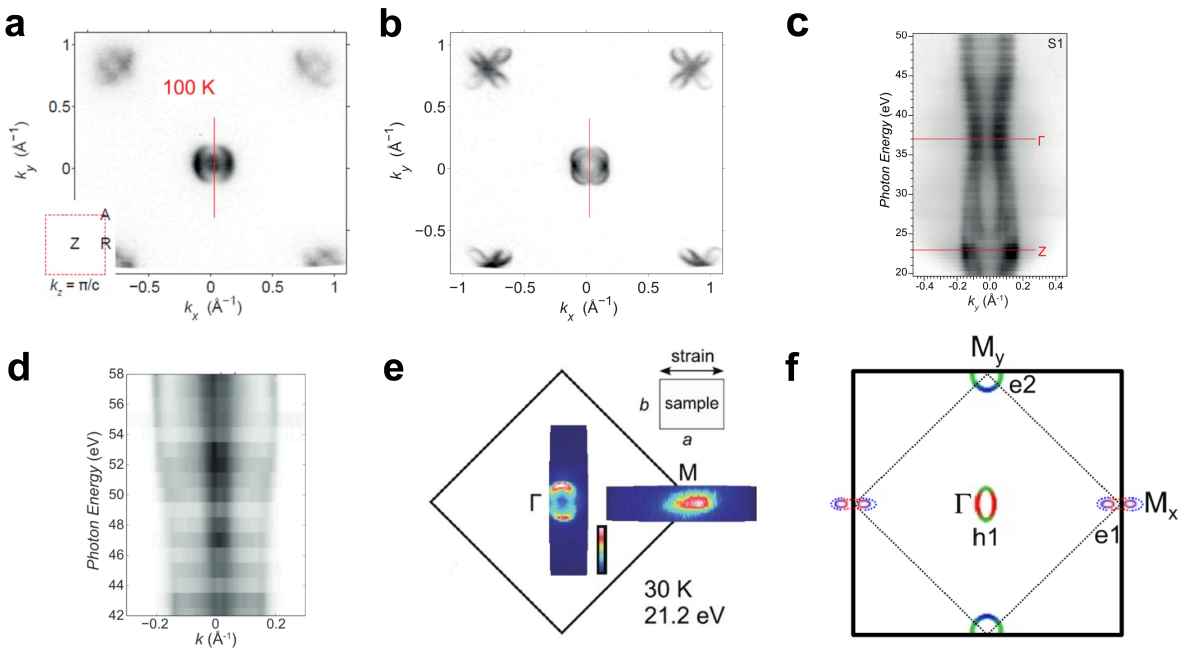

Figure 1.10: **a**−**d** Electronic structure of twinned FeSe investigated by ARPES [37]. **e** ARPES data for the Fermi surface of FeSe detwinned by the external strain [35]. **f** One proposed Fermi surface during the nematic phase [36].

out that the peanut-like pocket at point X can be divided into two Dirac points if the orbital splitting is large [36].

Qualitatively, the ARPES results are in agreement with the observations in the quantum oscillations [32, 38]. Fig. 1.11 shows the field dependence of transverse magnetoresistance ($\boldsymbol{H}//c$) measured at $\sim$ 40 mK [38]. The oscillations in the resistivity, the so-called the Shubnikov-de Haas (SdH) effect, are observed at above 16 T. By taking the fast Fourier transformation (FFT), four characteristic frequencies at below 1 kT are identified, as shown in Fig. 1.11. The extremal cross-section areas A of the Fermi surface, which are related to the frequencies F by the so-called Onsager relation $F = (\hbar/2\pi e)A$, are estimated to equal only 0.2−2.3% of the BZ. The FFT spectrum for different field angles are also plotted in Fig. 1.11b. As expected from the quasi-two-dimensional Fermi surface, the characteristic peak positions are weakly angle dependent. In addition, in Ref. [38], the Fermi energies E_F have also been estimated. This can be achieved by using the formula $E_F = \hbar^2 k_F^2/2m^* = \hbar^2 A/2\pi m^*$, where the effective mass

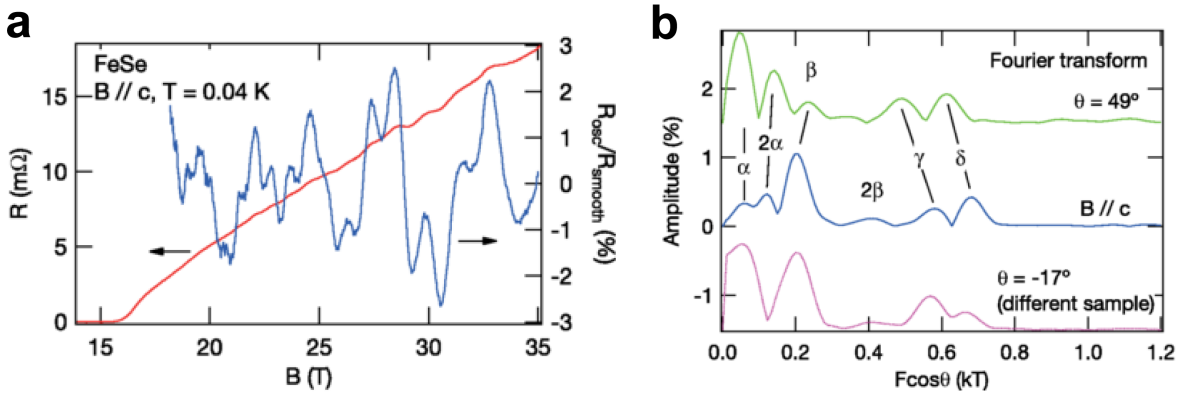

Figure 1.11: SdH oscillations observed in twinned FeSe [38]. **a** Field dependence of transverse magnetoresistance. **b** FFT spectrum of SdH oscillations for different field angles.

m^* is determined from the temperature dependence of the oscillation amplitude. The Fermi energies obtained are 3.6−18 meV, which are much smaller than that of $10^3 \sim 10^4$ meV in normal metals.

Quasiparticle interference (QPI) measured by STM provides another way to detect the underlying band structure. The QPI patterns are the electronic standing waves induced by defects or impurities. The scattering wave vector $\boldsymbol{q}$ determined from the QPI pattern connects two quasiparticle states that have the same energies, allowing us to infer the information about the electronic structure. Fig. 1.12b and c show the energy dispersion of the Fourier-transformed QPI patterns along the crystallographic directions b and a, respectively [30]. The magnetic field of 12 T is applied to suppress the superconductivity. The observed hole-like dispersion in Fig. 1.12b and electron-like dispersion in Fig. 1.12c can be ascribed to the intrapocket scattering (Fig. 1.12a) in the hole and electron pockets, respectively. In such case, the Fermi energy of the hole and electron pocket can be estimated from the top of the hole branches and the bottom of the electron branches. The estimated values are $\epsilon_F^h \sim 10$ meV for the hole pocket and $\epsilon_F^e \sim 2-3$ meV for the electron pocket, in agreement with the SdH results.

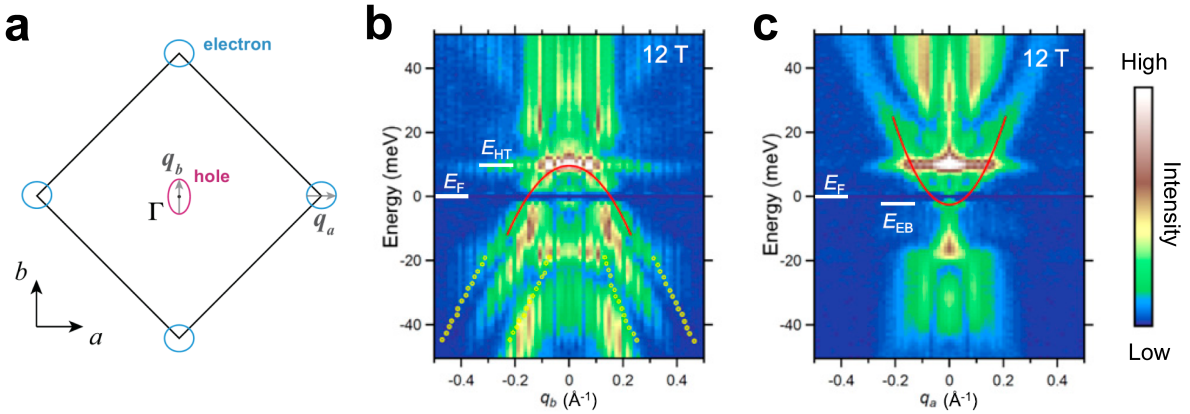

Figure 1.12: **a** Fermi surface of FeSe proposed by QPI. **b,c** QPI dispersions taken at 12 T along $\boldsymbol{q}_b$ and $\boldsymbol{q}_a$ directions, respectively. Peak positions of the representative branches are fitted with a quadratic function to obtain Fermi energies (red lines). Adapted from Ref. [30].

1.4.3 Electronic nematic order

As described above, in FeSe, the structural transition at T_s is accompanied by electronic structure anisotropy. A natural question is whether the transition is driven by the electronic or lattice degree of freedom. Similar to the iron-pnictides, the electronically driven scenario is preferred. One important experimental piece of evidence is from the elastoresistance measurements [39–42]. In this experiment, the nematic susceptibility $\chi_{\rm nem}$ is understood to be proportional to the derivative of the resistivity anisotropy $\psi = (\rho_a - \rho_b)/(\rho_a + \rho_b)$ with respect to the lattice strain ϵ, i.e., $\chi_{\rm nem} \propto {\rm d}\psi/{\rm d}\epsilon$. Here, ρ_a and ρ_b represent the resistivity along the a and b orthorhombic crystal axes, respectively. As shown in Fig. 1.13a and b, upon cooling toward T_s, the nematic susceptibility of FeSe shows a Curis-Weiss temperature dependence and diverges. The arguments based on the phenomenological Ginzburg-Landau model show that the quantity ${\rm d}\psi/{\rm d}\epsilon$ can diverge as $1/T$ only in the case of electronically driven transition, and otherwise remains a constant [43]. Therefore, the $1/T$ divergent behavior observed in FeSe suggests the electronic origin of the transition.

Furthermore, in the orthorhombic phase, orbital-dependent band shifts have been observed through ARPES measurements and discussed in terms of orbital ordering.

Fig. 1.13c shows the change in energy dispersion curves (EDCs) at point M with temperature [44]. Upon cooling to below $T_s \sim 90$ K, the degeneracy between the d_{xz} and d_{yz} orbital bands is lifted, manifested as the splitting of the peaks in the EDCs (marked by orange). At the lowest temperature, the magnitude of the splitting is ~ 50 meV. It has been argued that this d_{xz}/d_{yz} energy splitting value is much larger than the one predicted by the DFT calculation (~ 10 meV), indicating the orbital origin of the structure transition.

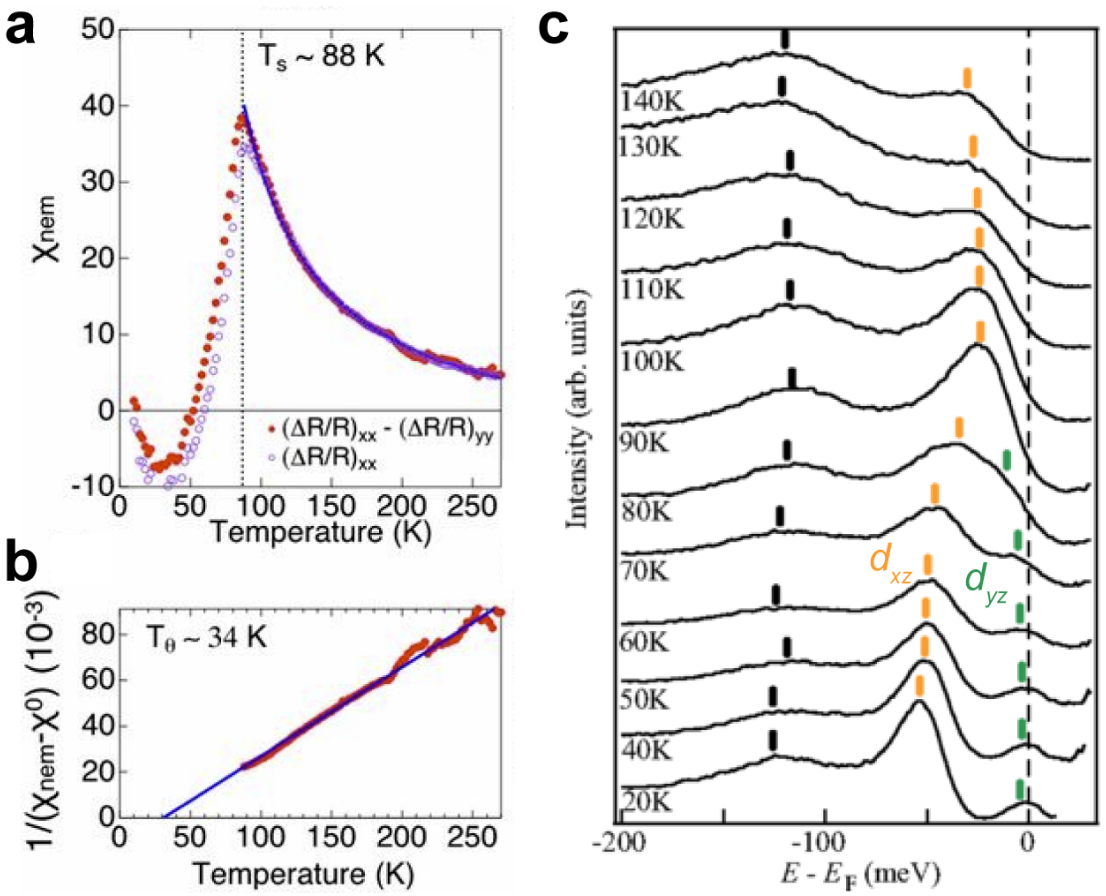

Figure 1.13: **a** Temperature dependence of the nematic susceptibility χ_{nem} for FeSe. The blue line is the fit to the Curie-Weiss formula. **b** Curie-Weiss plot of the same data shown in **a**. **c** Temperature evolution of EDCs at twinned point M measured using ARPES. Adapted from Refs. [39, 44].

1.4.4 Magnetic properties

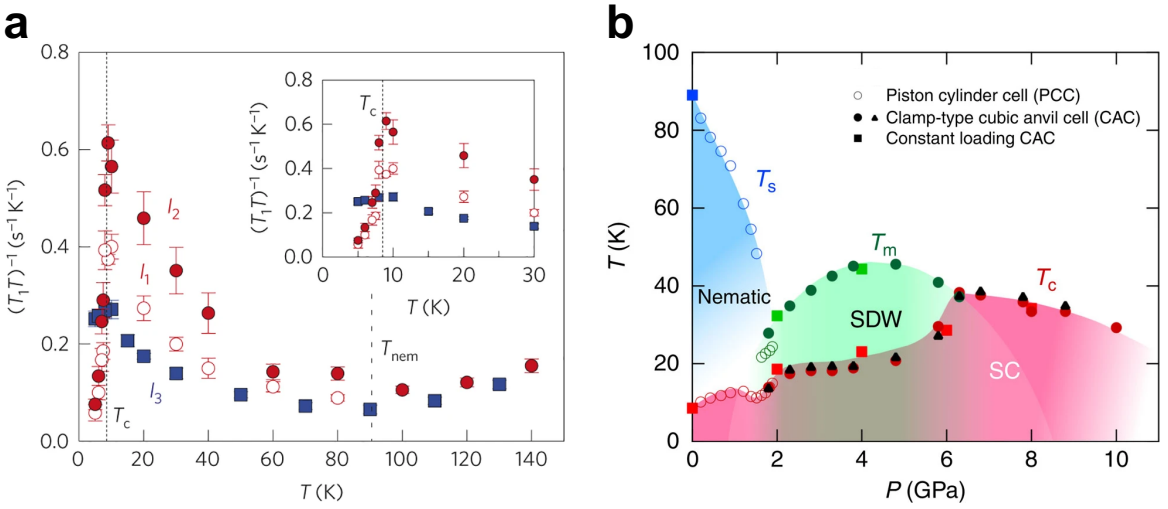

Figure 1.14: **a** Spin-lattice relaxation rate divided by temperature, $1/T_1T$, of FeSe plotted as a function of temperature T, measured using NMR at ambient pressure [25]. Here, l_1 and l_2 represent two splits of the ^{77}Se line in $\boldsymbol{H} \parallel a$, whereas l_3 is the ^{77}Se line in the $\boldsymbol{H} \parallel c$ configuration. The inset shows the same plot in a low-temperature regime. **b** The phase diagram of FeSe under pressure. Different types of the pressure cells (PCC, clamp type CAC, and constant loading CAC) are used [45]. The nematic (T_s), magnetic (T_m), and superconducting (T_c) transition temperatures are determined from the resistivity data $\rho(T)$.

Unlike other iron-based superconductors, the FeSe shows no magnetic order in the nematic phase at ambient pressure. Despite this point, it has been found that the FeSe is still closely related to magnetism.

Fig. 1.14a shows the $1/T_1T$ of ^{77}Se in FeSe measured through nuclear magnetic resonance (NMR), where $1/T_1$ is the spin-lattice relaxation rate [25]. Upon cooling below $T_s \sim 90$ K, the $1/T_1T$ gradually increases and reaches the peak at T_c. Given that $1/T_1T$ is related to the imaginary part of the dynamical susceptibility $\chi''(\mathbf{q}, \omega_0)$ by $1/T_1T \propto \sum_{\mathbf{q}} |A(\mathbf{q})|^2 \chi''(\mathbf{q}, \omega_0)/\omega_0$ (where $|A(\mathbf{q})|^2$ is hyperfine-coupling constant), the unusual enhancement at low temperature is attributed to the growing contribution from the spin fluctuations. This observation indicates that the superconducting FeSe is close to the magnetic instability. Similar results have also been reported in FeSe powders [46]. Notably, the spin fluctuations are weak near T_s, suggesting that the driving force of the

nematic transition is non-magnetic.

In addition, it was established that the magnetic order can be induced by pressure. Fig. 1.14b shows the temperature-pressure phase diagram of FeSe obtained from the resistivity measurements [45]. The magnetic order, which is possibly a spin density wave (SDW), is onset at $\sim$ 1.8 GPa and shows a dome-shaped pressure dependence. The generation of the magnetic order at low pressure supports the argument that the FeSe is nearly magnetic. Notably, near or at the boundaries of the magnetic phase, the pressure profile of T_c shows local maximums, indicating the intimate correlation between the superconductivity and the magnetism under pressure.

1.4.5 Superconducting gap

The FeSe exhibits a superconducting transition at $T_c \sim 9$ K. To unveil the nature of this superconductivity, it is essential to identify its superconducting gap structure. The measurements that are sensitive the low-energy quasiparticle DOS, such as the thermal conductivity and STM, are important tools used to study this issue.

It has been established that the superconducting gap structure in FeSe is extremely anisotropic [30, 47, 48]. Fig. 1.15a shows the thermal conductivity measurements from our group [30]. The residual linear term $\kappa_0/T \equiv \kappa/T(T \to 0)$ in the thermal conductivity, which is coupled to the zero-energy quasiparticles, shows a finite value (inset of Fig. 1.15a). This indicates the presence of a finite residual DOS at zero energy, which is typical for the nodal superconductors [49]. The same conclusion has also be obtained from scanning tunneling spectroscopy (STS) studies on the clean thin film and bulk samples [30, 47, 48]. In these experiments, the dI/dV spectrum, which is proportional to the local DOS, has a V-shaped profile (Fig. 1.15b). By contrast, the results against the nodes have been reported [50–52]. Fig. 1.16a and b show the thermal conductivity measurements reported by Bourgeois-Hope *et al.* [50]. In contrast to Fig. 1.15a, their residual κ_0/T is negligibly small (Fig. 1.16a), suggesting the absence of a gap node. This result is further confirmed by its exponential field dependence at below B^* (Fig. 1.16b). Moreover, κ_0/T increases rapidly at above B^*, indicating the presence of a small gap

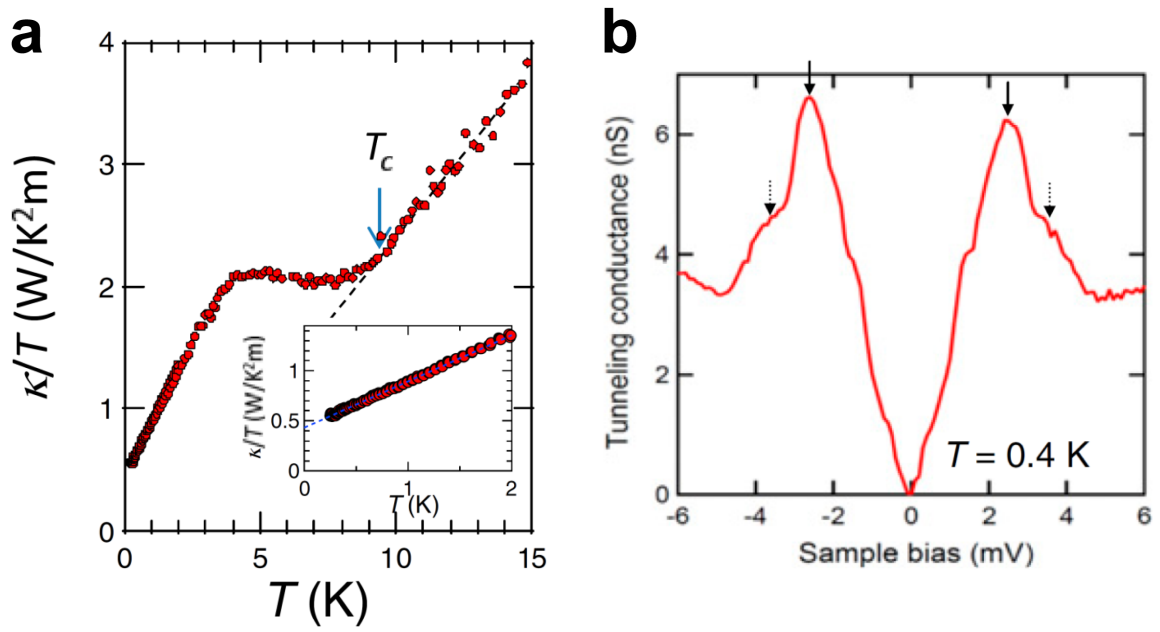

Figure 1.15: Experimental evidence for the node gap structure of FeSe [30]. **a** Temperature dependence of κ/T. Inset: the same plot in a low-temperature regime. **b** Tunneling spectroscopy measured at 0.4 K. The arrows indicate the superconducting gaps.

minimum (see section 1.5.4). Although no consensus has been reached on the presence or absence of the gap nodes, these studies agree that the superconducting gap structure of FeSe is extremely anisotropy. The disagreement between these studies might indicate that the gap nodes in FeSe are not protected by the symmetry and are thus sensitive to the amounts of the defects or twin boundaries. Indeed, near the twin boundaries, where the time reversal symmetry is broken, the suppression of the superconducting gap was observed through the STM measurement [53].

The momentum dependent gap structures of FeSe have been deduced from the Bogoliubov QPI patterns [51]. As shown in Fig. 1.16c and d, the gap structure on the hole band (labeled as α-band) and one of the electron bands (labeled as δ-band) have been detected and exhibit a two-fold symmetric anisotropy. By comparing the gap magnitude with the orbital weight of the calculated band structure (Fig. 1.16d), it was found that the gap maximums and minimums are located at the Fermi surface parts dominated by the d_{yz} and d_{xz}/d_{xy} orbital characteristics, respectively. This provides

evidence for the orbital selectivity pairing mechanism in FeSe. Moreover, these two gaps have different signs, suggesting a $s_{\pm}$ superconducting state. Notably, no gap have been assigned to the Y point. This fact is consistent with the failure of detection of one electron pocket in ARPES measurements.

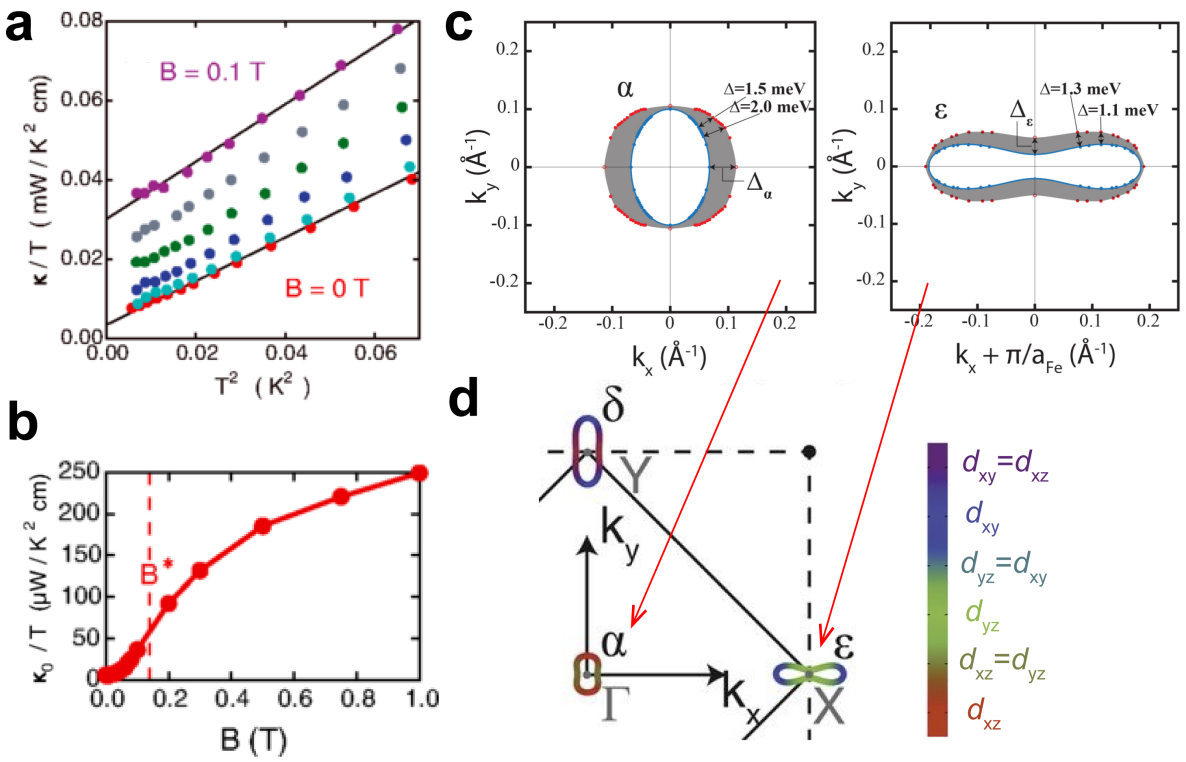

Figure 1.16: Node-less gap structure of FeSe revealed through thermal conductivity and STM measurements [50, 51]. **a** The thermal conductivity divided by temperature, κ/T, plotted as a function of T^2 at several magnetic fields. The black lines are linear fits. **b** Field dependence of the residual term in thermal conductivity, κ_0/T. Here, B^* marks a kink in the curve. **c** The gap structures inferred from Bogoliubov QPI. **d** Fermi surface of FeSe proposed by STM.

1.5 $FeSe_{1-x}S_x$

Having reviewed the basic properties of FeSe, we now turn our attention to the isoelectronic S-substituted effect in FeSe. The $FeSe_{1-x}S_x$ system is thought to have a nonmagnetic nematic QCP, providing a unique platform to study the effect of pure nematic fluctuations under both normal and superconducting states. In this section, we briefly introduce some experiment findings related to this nematic QCP.

1.5.1 Phase diagram and nematic QCP

Fig. 1.17a shows the phase diagram of $FeSe_{1-x}S_x$ [39]. As the S concentration increases, the nematic transition temperature T_s gradually decreases and becomes zero at $x_c \sim 0.17$. In contrast to the pressure effect (Fig. 1.14b), no magnetic order is induced by S substitution. These facts make $FeSe_{1-x}S_x$ a candidate system that harbors a nonmagnetic nematic QCP.

Indeed, a strong enhancement of the nematic susceptibility as concentration S approaches $x_c \sim 0.17$ has been reported. The colors in Fig. 1.17a represent the magnitude of χ_{nem} measured based on the resistivity anisotropy (see section 1.4.3). It can be seen that $\chi_{nem}(T)$ in the nematic regime of $FeSe_{1-x}S_x$ strongly increases upon cooling. In fact, these data can be fitted with the Curie-Weiss formula: $\chi_{nem}(T) = \lambda/a(T-T_\theta)+\chi^0$ (Fig. 1.17b). The obtained Weiss temperature T_θ is also plotted in Fig 1.17a. Note that T_θ is interpreted herein as the nematic transition temperature decoupled from the lattice. Upon doping, T_θ is suppressed to zero at $x_c \sim 0.17$, implying that the nematic fluctuations continuously increase to 0 K. Moreover, when approaching x_c, the magnitude of χ_{nem} shows a strong enhancement (Fig. 1.17a). These observations suggest the existence of the nematic QCP at $x_c \sim 0.17$.

Another noticeable point in this phase diagram is the evolution of the superconducting transition temperature T_c with S doping. Upon doping, T_c first shows a slight enhancement and then gradually decreases as $x > 0.08$. In contrast to the case of AFM QCP (see section 1.3.3), T_c is not peaked at this nematic QCP. Instead, it slightly

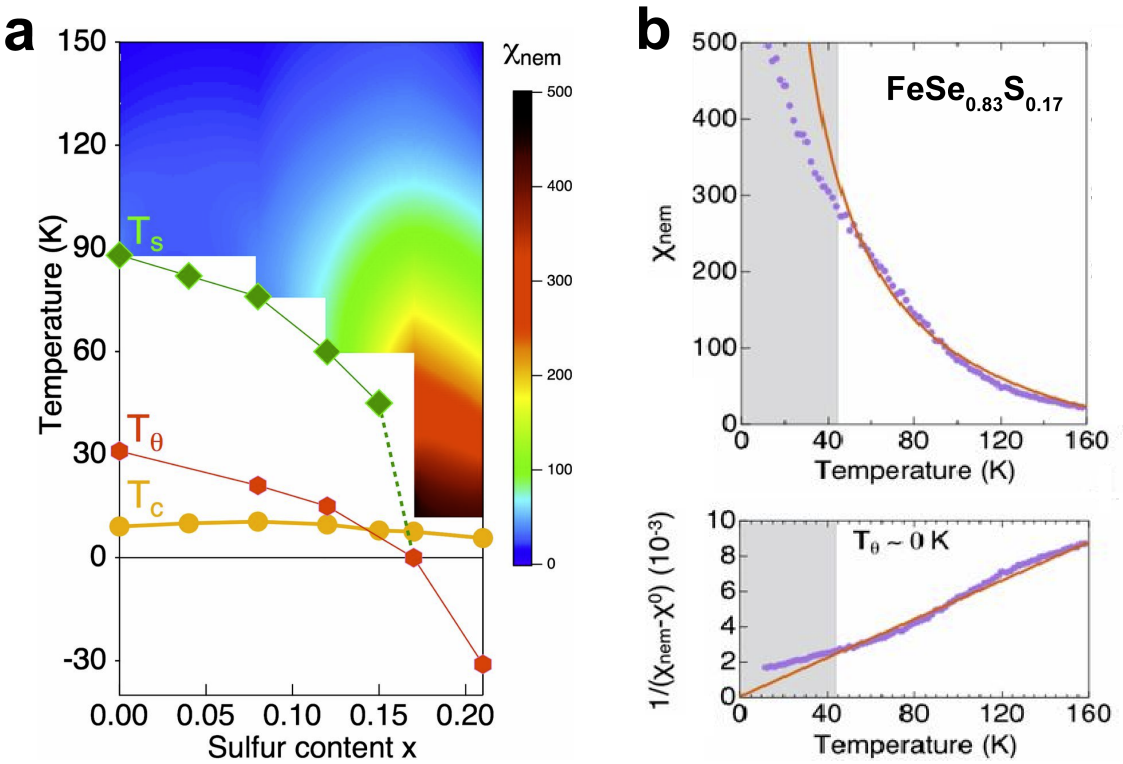

Figure 1.17: **a** Phase diagram of $FeSe_{1-x}S_x$. Colors in the tetragonal regime represent the magnitude of the nematic susceptibility $\chi_{\rm nem}$. The Weiss temperature T_θ is obtained by fitting $\chi_{\rm nem}(T)$ curves to the Curie-Weiss formula. The nematic transition $T_{\rm s}$ and superconducting transition temperature $T_{\rm c}$ are determined from the resistivity data. **b** Upper panel: Temperature dependence of $\chi_{\rm nem}$ for $x = 0.17$. Bottom panel: Temperature dependence of $1/(\chi_{\rm nem} - \chi^0)$ for $x = 0.17$. According to the Curie-Weiss formula, $1/(\chi_{\rm nem} - \chi^0)$ is proportional to $T - T_\theta$. The red lines are the fits to Curie-Weiss formula. The grey shaded regions mark the deviations of the data from the fit. Such deviations might arise from the impurities. Adapted from Ref. [39].

decreases from $\sim$ 8 K to $\sim$ 5 K when crossing x_c [54]. Interestingly, as shown in section 1.5.4, the superconducting gap structure changes dramatically when crossing the nematic QCP.

1.5.2 Fermi surface

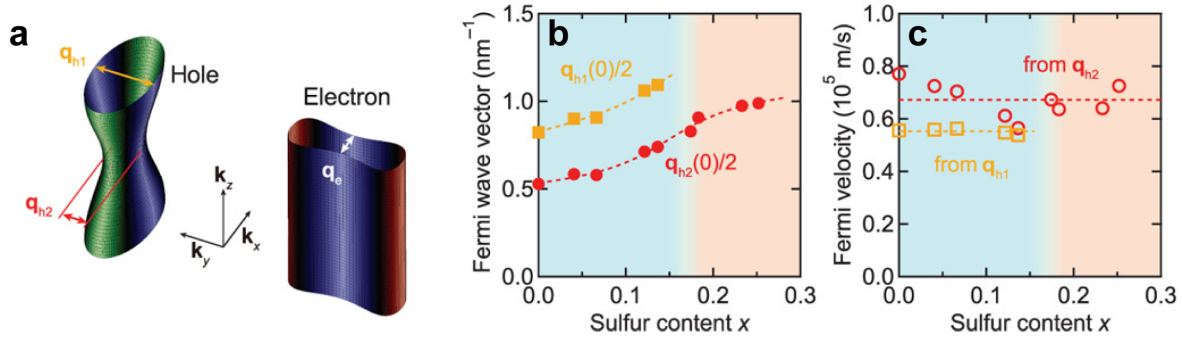

Figure 1.18: Electronic structure of $FeSe_{1-x}S_x$ detected by QPI [55]. **a** Schematic image of the proposed three-dimensional Fermi surface. $\boldsymbol{q}_{\mathrm{h1}}$, $\boldsymbol{q}_{\mathrm{h2}}$, and $\boldsymbol{q}_{\mathrm{e}}$ are the wave vectors extracted from QPI imaging. **b** S content dependence of Fermi wave vectors. **c** S content dependence of the Fermi velocities. The dotted lines are eye guides.

The electronic structure of $FeSe_{1-x}S_x$ have been detected using the QPI technique [55]. The results are summarized in Fig. 1.18. Here, $\boldsymbol{q}_{\mathrm{h1}}$ and $\boldsymbol{q}_{\mathrm{h2}}$ are the wave vectors obtained from the Fourier transform of the QPI imaging and are interpreted as the results of the backscattering (scattering from $\boldsymbol{k}$ to $-\boldsymbol{k}$ state) in the outer three-dimensional hole pocket (Fig. 1.18a). Under this scenario, $\boldsymbol{q}_{\mathrm{h1}}/2$ and $\boldsymbol{q}_{\mathrm{h2}}/2$ can be identified as the Fermi wave vectors from the hole pocket at $k_z = \pi/c$ and 0, respectively. The S content dependence of these two Fermi wave vectors and their Fermi velocities are shown in Fig. 1.18b and c, respectively. Both Fermi wave vectors increase with an increase in the concentration of S, indicating an increasing Fermi surface size. Note that $\boldsymbol{q}_{\mathrm{h1}}/2$ disappears for $x > 0.14$. This might indicate that the k_z dependence of the hole pocket becomes weaker with a higher S content. Importantly, the $\boldsymbol{q}_{\mathrm{h2}}/2$ and its Fermi velocity change continuously when crossing the nematic QCP.

The SdH measurements also show the electronic structure of $FeSe_{1-x}S_x$ [55]. Fig. 1.19a shows the S content dependence of the oscillation frequencies F. For most of the ob-

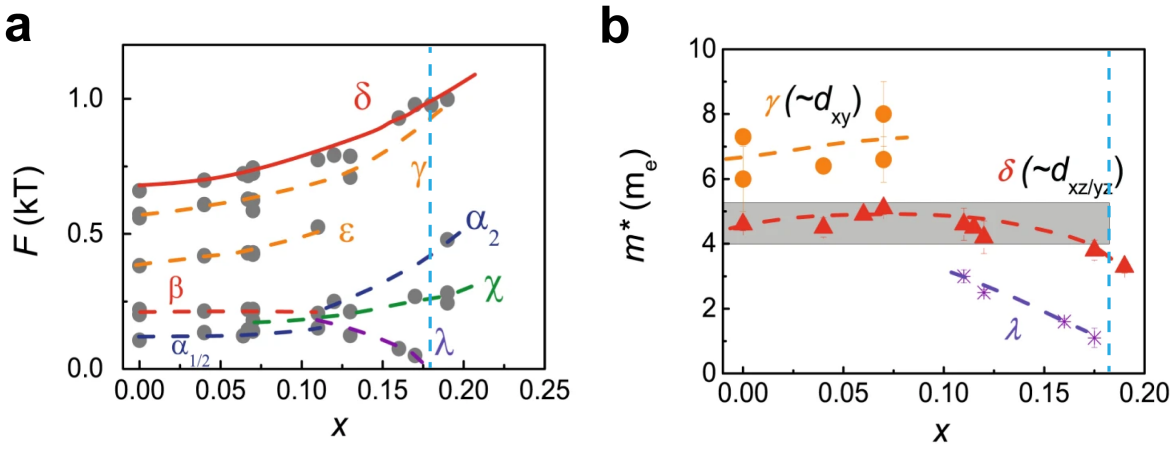

Figure 1.19: Electronic structure of $FeSe_{1-x}S_x$ detected by SdH measurements [56]. **a** Evolution of the observed oscillation frequencies with S concentration. **b** S content dependence of the estimated effective mass. The δ orbit is assigned to the outer hole pocket. The blue dotted line indicates the location of the nematic QCP.

served branches, the frequencies increase with increasing concentrations in S, indicating the expansion of the Fermi surface sizes. This trend continues when crossing the nematic QCP, suggesting the change of the Fermi surface without reconstruction. Fig. 1.19b shows the doping evolution of the effective mass m^*. Interestingly, the effective mass of the δ branch, which is assigned to the outer hole pocket, does not change dramatically near the QCP. This behavior is quite different from the situation near AFM QCP, where the strong enhancement of the quasiparticle masses are observed.

To summarize, the above experiments reveal that the Fermi surface evolves smoothly when crossing the nematic QCP.

1.5.3 AFM fluctuations

As discussed in section 1.4.4, the AFM fluctuations are still important in pure FeSe. This makes it difficult to determine the effect of solely nematic fluctuations. Fortunately, as will be shown below, the S substitution can suppress the AFM fluctuations.

Fig. 1.20 shows the phase diagram of $FeSe_{1-x}S_x$ obtained from ^{77}Se NMR measurements [57]. The $(1/T_1T)_{\mathrm{AFM}}$ is the contribution of AFM fluctuations to the $1/T_1T$. For

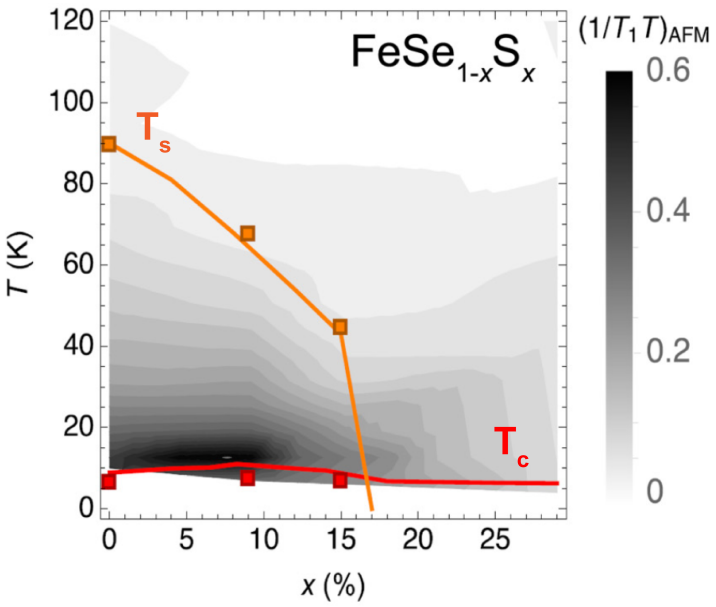

Figure 1.20: Phase diagram of $FeSe_{1-x}S_x$ obtained from ^{77}Se NMR measurements [57]. The $(1/T_1T)_{\mathrm{AFM}}$ is the AFM fluctuation term of $1/T_1T$. The values of T_s and T_c are determined from the resistivity. The AFM fluctuations are suppressed near the nematic QCP.

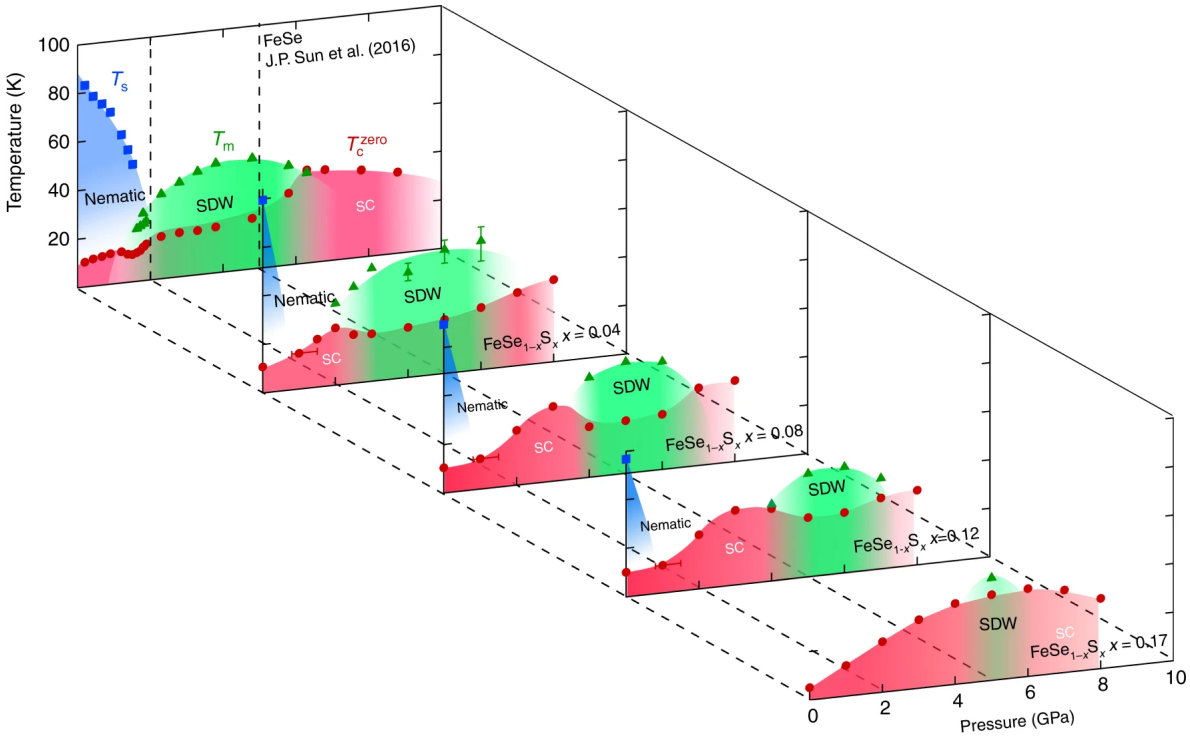

Figure 1.21: Evolution of the pressure-temperature phase diagram of FeSe with S doping [58]. The nematic (T_s), magnetic (T_m), and superconducting (T_c) transition temperatures are determined from the resistivity data.

the samples with a low S concentration ($x < 0.1$), a notable increase of $(1/T_1T)_{\mathrm{AFM}}$ at low temperatures is found and is attributed to an enhancement of the AFM fluctuations. Inside the nematic phase, the enhancement of the AFM fluctuations tracks that of T_c, suggesting the important role of AFM fluctuations in the superconductivity. However, for $x \geq 0.17$, the low-temperature enhancement is much weaker, indicating the suppression of AFM fluctuations at near the nematic QCP.

Fig. 1.21 shows a temperature-pressure-concentration phase diagram of $FeSe_{1-x}S_x$ obtained from high-pressure resistivity measurements [58]. The nematic (T_s), magnetic (T_m) and superconducting (T_c) transition temperatures are determined by the kink anomalies in the resistivity. In pure FeSe, the SDW phase is onset at a relatively low pressure and exists within a certain pressure range. With an increase in the S concentration, the SDW onset pressure goes toward a higher value and the pressure range where it occurs becomes narrower. Eventually, at $x = 0.17$, the magnetic phase is found only at ~ 5.0 GPa, suggesting that the sample is near the end of the pressure-induced magnetic order. These observations indicate that the $FeSe_{1-x}S_x$ system is driven away from the magnetic instability through S-doping.

Therefore, combined with the observation of large nematic fluctuations at around x_c, we can state that the $FeSe_{1-x}S_x$ system is a good platform for studying the effect of pure nematic fluctuations under both normal and superconducting states.

1.5.4 Superconducting state

The superconducting gap structure of $FeSe_{1-x}S_x$ has been revealed through field-dependence studies of thermal conductivity κ. In the presence of a magnetic field, the quasiparticle energy spectrum will shift as $E(\boldsymbol{k}) \rightarrow E(\boldsymbol{k}) - \hbar\boldsymbol{k} \cdot \boldsymbol{v}_s$ (where $\boldsymbol{v}_s$ is supercurrent velocity around the vortex) owing to the Doppler effect [49, 59]. As a result, the quasiparticle DOS can change significantly if the line nodes exist. It has been pointed out that, for a line node with linear energy dependent DOS, i.e., $N(E) \propto E$, $N(H)$ can change as $H^{1/2}$, leading to the $H^{1/2}$ dependent κ/T. However, for the s-wave gap structure, the κ/T changes exponentially with the field when the Doppler

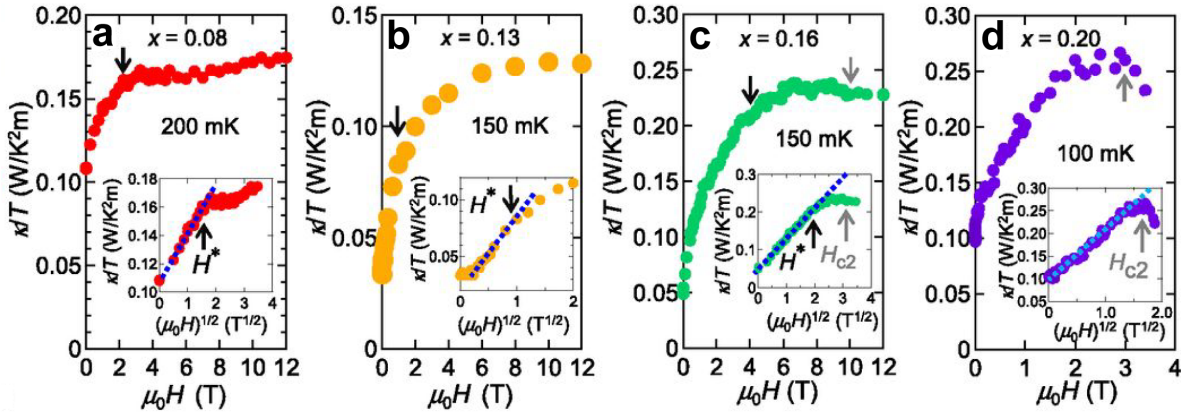

Figure 1.22: Thermal conductivity measurements for a series of $FeSe_{1-x}S_x$ [11]. The field direction is parallel to the c-axis.

shift is smaller than the gap amplitude. Fig. 1.22 shows the field dependence of κ/T for $FeSe_{1-x}S_x$ [11]. For the nematic samples ($x = 0.08, 0.13, and 0.16$), κ/T increases as $H^{1/2}$ up to a certain field H^* (below H_{c2}) and then follows a much weaker field dependence. The initial rapid increase of κ/T with the field indicates the presence of the gap node or deep gap minimum. In addition, the shoulder at field H^* has been attributed to the suppression of the smaller gap at a certain Fermi surface, suggesting a multigap characteristic. However, for the tetragonal sample ($x = 0.2$), such a multigap behavior is not observed, i.e., κ/T shows $H^{\frac{1}{2}}$ dependence at up to H_{c2}. These results suggest a dramatic gap structure change at the nematic QCP.

The above finding is consistent with the STM measurements. Fig. 1.23a shows the STS measurements of $FeSe_{1-x}S_x$ for various S concentrations [55]. The tunneling spectrum, which is proportional to the local DOS, has a V-shaped profile near the zero bias for all measured samples. This indicates the presence of the superconducting nodes in $FeSe_{1-x}S_x$ [48]. The peak features in the spectrum indicate the superconducting gap. To resolve more gap features, the authors take the second energy derivative of each tunneling spectrum. Note that the dip in the second derivative curve corresponds to the peak of the original value. As shown in Fig. 1.23b, several gaps have been resolved. These gaps change little in the nematic samples. However, when crossing the nematic

QCP ($x_c \sim 0.17$), the gap features change dramatically, indicating a superconducting phase transition at the nematic QCP. Notably, the gap size is also reduced for $x > 0.17$. This is consistent with the suppression of T_c in the tetragonal samples [54].

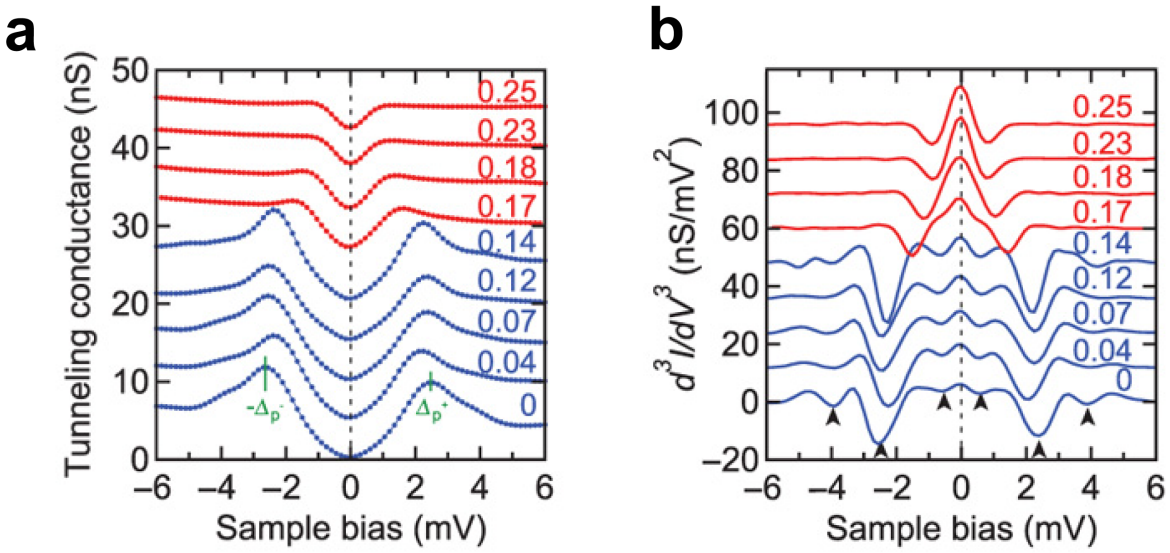

Figure 1.23: STS measurements for a series of $FeSe_{1-x}S_x$ [55]. **a** Tunneling spectrum of $FeSe_{1-x}S_x$. The green bars mark the main peaks. **b** The second derivative of the tunneling spectra with respect to the sample bias.

1.5.5 Transport properties

Although the Fermi surface changes smoothly when crossing the nematic QCP in $FeSe_{1-x}S_x$, the nematic QCP can have a significant impact on the transport properties [60–62]. Fig. 1.24a shows the low-temperature resistivity for $x = 0.16$ [60]. In a high field (35 T) parallel to the *ab* plane, the T-linear resistivity is observed down to the extremely low temperature. In the conventional Fermi-liquid theory, the resistivity is quadratic temperature dependent. Thus, the T-linear resistivity is a typical NFL behavior. Fig. 1.24b shows the phase diagram of $FeSe_{1-x}S_x$ based on such high field results for various values of x. For the samples away from the nematic QCP, the resistivity deviates from the T-linear dependence when decreasing the temperature to below T_1 and changes to the a strictly T^2 dependence at below T_2. The doping profiles

of both T_1 and T_2 have a funnel centered at $x_c \sim 0.16$, similar to the typical QCP phase diagram shown in Fig. 1.1, indicating that the nematic fluctuations extend up to a finite temperature. These results suggest that the critical fluctuations of the nematic order can indeed give rise to the NFL behavior.

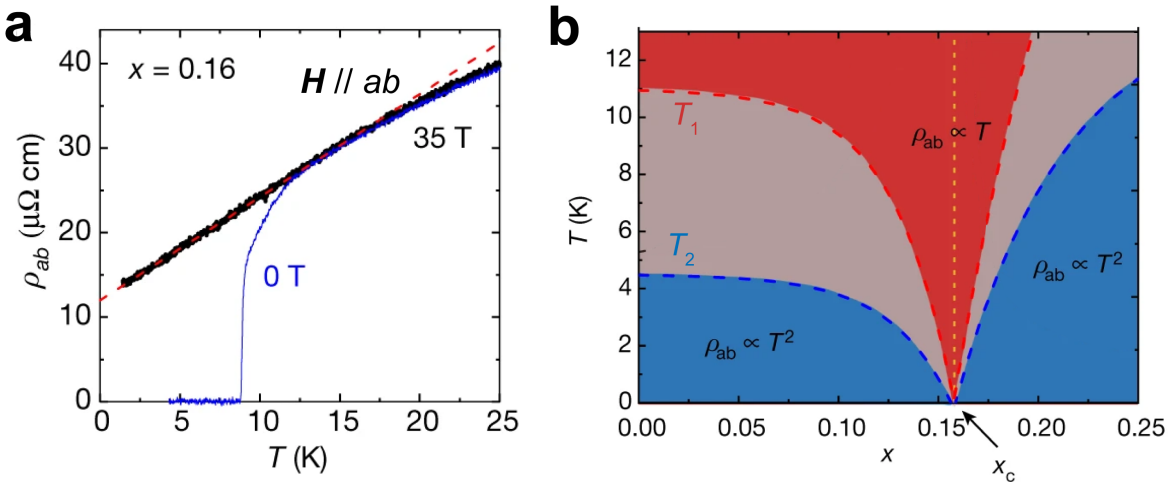

Figure 1.24: **a** Low temperature resistivity of $FeSe_{0.84}S_{0.16}$ measured at 0 and 35 T. The field is applied parallel to the ab plane. **b** Phase diagram of $FeSe_{1-x}S_x$ obtained from the high field resistivity measurements. Adapted from Ref. [60].

1.6 Purpose and organization of this study

As discussed above, quantum fluctuations emanating from a QCP are often considered a possible source for the unconventional superconductivity and NFL behaviors [63, 64]. Therefore, understanding the physics associated with quantum fluctuations is of primary importance. Looking at the specific case of iron-based superconductors, two putative QCPs are often found near the superconductivity (Fig. 1.6), i.e., the AFM and nematic QCP. It has been discussed that spin fluctuations can lead to a $s_{\pm}$ superconducting state, whereas the orbital fluctuations prefer s_{++} superconductivity. In this context, experimentally identifying the role of the nematic and AFM fluctuations is crucial to revealing an unconventional superconductivity.

In section 1.5, we demonstrated that the iron-based superconductor $FeSe_{1-x}S_x$, which has a nematic QCP without sizeable spin fluctuations, is particularly suitable to studying the nature of critical nematic fluctuations. In addition, recent transport measurements indicated a critical fan-like region of T-linear resistivity in a temperature-doping phase diagram (Fig. 1.24), indicating the influence of the nematic fluctuations on normal transport properties. Because $FeSe_{1-x}S_x$ is a multi-band system, it is important to find other evidence of NFL behaviors during charge transport. For this reason, we conducted systematic measurements of the resistivity, Hall effect, and magnetoresistance across the nematic QCP of $FeSe_{1-x}S_x$ at low fields.

The remainder of this thesis is organized as follows. In Chapter 2, we provide a background on a Fermi liquid and NFL behaviors during charge transport. In Chapter 3, we describe some experimental details, including the crystal growth and characterization, as well as the transport techniques. In Chapter 4, we discuss our transport measurements on $FeSe_{1-x}S_x$. Finally, we conclude this study in Chapter 5.

2

Non-Fermi liquid behavior in transport properties

2.1 Boltzmann transport theory

In this section, we introduce a theoretical treatment for the electrical transport phenomenon, i.e., the Boltzmann transport theory [65]. This semiclassical theory, which describes how to determine the distribution function $f(\boldsymbol{r}, \boldsymbol{k}, t)$ in a steady state, remains one of most important and straightforward theories in explaining the transport properties in solids.

Let us start from the semiclassical equation for the motion of the carriers in the presence of the electrical and magnetic fields $\boldsymbol{E}$ and $\boldsymbol{B}$, which is given by

$$\hbar \frac{d\boldsymbol{k}}{dt} = -e(\boldsymbol{E} + \boldsymbol{v_k} \times \boldsymbol{B}), \tag{2.1}$$

where $\boldsymbol{v_k} = \partial \varepsilon_{\boldsymbol{k}} / \partial \boldsymbol{k}$ is the carrier velocity (where $\varepsilon_{\boldsymbol{k}}$ is the band dispersion). With this equation, we expect that $f(\boldsymbol{r}, \boldsymbol{k}, t)$ can change as

$$\frac{\partial f(\boldsymbol{r}, \boldsymbol{k}, t)}{\partial t}|_{field} = -\frac{e}{\hbar}(\boldsymbol{E} + \boldsymbol{v_k} \times \boldsymbol{B}) \cdot \frac{\partial f(\boldsymbol{r}, \boldsymbol{k}, t)}{\partial \boldsymbol{k}}. \tag{2.2}$$

However, in a steady state, $f(\boldsymbol{r}, \boldsymbol{k}, t)$ should not vary over time. Here, we consider that the effect of scattering balances that of the external fields. Thus,

$$\frac{\partial f(\boldsymbol{r}, \boldsymbol{k}, t)}{\partial t}|_{field} + \frac{\partial f(\boldsymbol{r}, \boldsymbol{k}, t)}{\partial t}|_{scatt} = 0. \tag{2.3}$$

The scattering term in Eq. 2.3 is complex and involves various scattering mechanisms, such as the electron-phonon and inelastic electron-electron interactions. A simple method used to model this term is the relaxation time approximation.

Within the relaxation time approximation, the change in function $f(\boldsymbol{r}, \boldsymbol{k}, t)$ is assumed to be

$$\frac{\partial f(\boldsymbol{r}, \boldsymbol{k}, t)}{\partial t}|_{scatt} = -\frac{g(\boldsymbol{r}, \boldsymbol{k}, t)}{\tau} \tag{2.4}$$

Here, $g(\boldsymbol{r}, \boldsymbol{k}, t) = f(\boldsymbol{r}, \boldsymbol{k}, t) - f^0(\boldsymbol{r}, \boldsymbol{k}, t)$. In addition, $f^0(\boldsymbol{r}, \boldsymbol{k}, t)$ is the equilibrium distribution function. Moreover, τ is called the scattering time, which can be understood as the time required to return to the equilibrium when the external field is suddenly turned off. Indeed, it can be shown that in such a case $g(\boldsymbol{r}, \boldsymbol{k}, t)$ decays as

$$g(\boldsymbol{r}, \boldsymbol{k}, t) = g(\boldsymbol{r}, \boldsymbol{k}, 0)^{-t/\tau}. \tag{2.5}$$

By substituting Eqs. 2.2 and 2.4 into Eq. 2.3, and ignoring the higher order terms, we can obtain

$$\frac{g(\boldsymbol{r}, \boldsymbol{k}, t)}{\tau} + \frac{e}{\hbar}(\boldsymbol{v_k} \times \boldsymbol{B}) \cdot \frac{\partial g(\boldsymbol{r}, \boldsymbol{k}, t)}{\partial \boldsymbol{k}} = [-\frac{\partial f^0(\boldsymbol{r}, \boldsymbol{k}, t)}{\partial \varepsilon}] e\boldsymbol{E} \cdot \boldsymbol{v_k}. \tag{2.6}$$

Having known this linearized Boltzmann equation, we can calculate the conductivity $\boldsymbol{J}$ through the following formula:

$$\boldsymbol{J} = \frac{1}{4\pi^3} \int e\boldsymbol{v_k} g(\boldsymbol{r}, \boldsymbol{k}, t) d^3k. \tag{2.7}$$

For example, for an isotropic Fermi surface, the zero magnetic field conductivity is

expressed as follows:

$$\sigma = \frac{ne^2\tau}{m^*}, \tag{2.8}$$

where n is the carrier numbers. This formula is consistent with the result derived from the Drude model. Although this is based on a relatively simple assumption, Eq. 2.8 provides a useful starting point to understand the conductivity.

2.2 Transport properties in Fermi liquid

To understand the NFL behaviors that arise from the critical fluctuations, it is necessary to know the conventional Fermi liquid behaviors. In this section, we focus on three fundamental charge transport coefficients, i.e., the resistivity, Hall coefficient, and magnetoresistance, which are described well within the image of the Fermi liquid.

Resistivity

In a Fermi liquid, the resistivity that is dominated by the inelastic electron-electron scattering is expected to vary as

$$\rho = \rho_0 + AT^2, \tag{2.9}$$

where ρ_0 is the residual resistivity owing to the scattering from impurities and defects. The coefficient A reflects the strength of the electron-electron interactions. In a two-dimensional isotropic model, A can be expressed as

$$A = \frac{8\pi^3 ack_B^2}{e^2\hbar^3}\frac{m^{*2}}{k_F^3}, \tag{2.10}$$

where a and c are the lattice constants [66]. This T^2 resistivity has indeed been observed in many correlated materials, such as the high-T_c cuprates and heavy fermion compounds. Notably, in weakly correlated metals, A is usually too small to be observed. Instead, the low temperature resistivity is dominated by the electron-phonon interaction and exhibits T^5 temperature dependence.

A simple but non-rigorous way to better understand the effect of the electron-electron scattering mechanism on the resistivity is as follows [66–70]: At finite temperature T, the scattering electrons are restricted to the energy $\sim k_B T$ of the Fermi surface. Therefore, the available number of initial states, as well as the final states, of the scattering will be on the order of $\sim N(E_F)k_B T$. Because the scattering probability is proportional to the numbers of both the initial and final states, the scattering rate $1/\tau$ will vary as $\sim (N(E_F)k_B T)^2$. Thus, a T-square resistivity is expected.

Hall coefficient

The Hall effect appears when the magnetic field $\boldsymbol{H}$ is applied perpendicular to the electrical current $\boldsymbol{I}$. It gives the information on the Fermi surface topology and carrier density. In an isotropic one-band model, the Hall coefficient R_{H} is expressed as follows:

$$R_{\mathrm{H}} \equiv \frac{\rho_{xy}}{H} = \frac{1}{ne}, \tag{2.11}$$

where n is the carrier number. As shown, R_{H} depends only on the carrier numbers and does not change with temperature. Considering that $\sigma = ne^2\tau/m^*$ (Eq. 2.8), we have the following:

$$\cot\theta_{\mathrm{H}} = \frac{m^*}{eB}\frac{1}{\tau} = \frac{1}{\omega_c \tau}, \tag{2.12}$$

where ω_c is the frequency at which the magnetic field causes the electrons to sweep across the Fermi surface. It can be seen that the resistivity and Hall angle are governed by a single scattering time.

The situation becomes complex when multiple bands are involved. For simplicity, we consider the case for the two-band model [71]. The R_{H} is given by the following:

$$R_{\mathrm{H}} = \frac{(\sigma_h^2 R_h + \sigma_e^2 R_e) + \sigma_h^2 \sigma_e^2 R_h R_e (R_h + R_e) H^2}{(\sigma_h + \sigma_e)^2 + \sigma_e^2 \sigma_h^2 (R_h + R_e)^2 H^2}, \tag{2.13}$$

where σ_i and R_i are the conductivities and the Hall coefficients for the two carriers. R_{H} can vary with temperature if the conductivities of each carrier have a different temperature dependency.

In this study, we focus on $FeSe_{1-x}S_x$. This system is known to be a compensated semimetal with an equal number of electrons and holes ($n_e \approx n_h$). In a compensated two-band model with circular pockets, the R_{H} is reduced to the following:

$$R_{\mathrm{H}} = \frac{1}{ne} \times \frac{\sigma_h - \sigma_e}{\sigma_h + \sigma_e}, \tag{2.14}$$

In this case, even a slight difference in the T dependence of σ_i can produce a strong temperature dependent R_{H}, as well as a change in sign.

Orbital magnetoresistance

The orbital magnetoresistance arises from the change in the electron trajectory by the Lorentz force. For a spherical Fermi surface, the magnetoresistance is zero owing to the cancellation of the Lorentz force by the Hall electrical field. However, if more than one type of carrier is considered, the magnetoresistance can be finite.

Considering a specific case of a two-carrier model [71], according to the Boltzmann equation, the resistivity is given by

$$\rho_{xx} = \frac{(\sigma_h + \sigma_e) + \sigma_h\sigma_e(\sigma_h R_h^2 + \sigma_e R_e^2)H^2}{(\sigma_h + \sigma_e)^2 + \sigma_e^2\sigma_h^2(R_h + R_e)^2H^2}. \tag{2.15}$$

At low fields, ρ_{xx} shows a H^2 dependence, which is typical for conventional metals. By contrast, its tendency of saturation at a high field is dependent on the specific Fermi surface topology. Indeed, if the two carriers have different signs and $n_e \approx n_h$, Eq. 2.15 is reduced to the following:

$$\rho_{xx} = \frac{1 + \frac{1}{ne}\sigma_h\sigma_e H^2}{(\sigma_h + \sigma_e)}. \tag{2.16}$$

In this situation, ρ_{xx} varies quadratically with a magnetic field without saturation.

In conventional metals, the magnetoresistance is often analyzed in terms of Kohler's rule [72], which states that in a system with a single scattering time, the ratio $\frac{\Delta\rho_{xx}(T,H)}{\rho_{xx}(T,0)}$ can be expressed by $\omega_c\tau$. Here, $\Delta\rho_{xx}(T,H) \equiv \rho_{xx}(T,H) - \rho_{xx}(T,0)$ and $\omega_c \equiv eB\hbar/m^*$ is the cyclotron frequency. Because the resistivity in a zero field $\rho_{xx}(T,0)$ is inversely

proportional to τ (see Eq. 2.8), the following is obtained:

$$\frac{\Delta\rho_{xx}(T,H)}{\rho_{xx}(T,0)} = F(\omega_c\tau) = F\left(\frac{H}{\rho_{xx}(T,0)}\right), \tag{2.17}$$

where the function $F(x)$ is related to the Fermi surface. Again, we take the case of the two-carrier model as an example [65]. Following Eq. 2.15, we obtain the following:

$$\frac{\Delta\rho_{xx}(T,H)}{\rho_{xx}(T,0)} = \frac{\sigma_h\sigma_e(\sigma_h R_h - \sigma_e R_e)^2 H^2}{(\sigma_h+\sigma_e)^2 + \sigma_e^2\sigma_h^2(R_h+R_e)^2H^2}. \tag{2.18}$$

Assuming that the two carriers are governed by a single scattering time τ, the ratio $\frac{\Delta\rho_{xx}(T,H)}{\rho_{xx}(T,0)}$ can then be written as follows:

$$\frac{\Delta\rho_{xx}(T,H)}{\rho_{xx}(T,0)} = \frac{\lambda(R_h - \lambda R_e)^2(\sigma_h H)^2}{(1+\lambda)^2 + \lambda^2(R_h+R_e)^2(\sigma_h H)^2} = F(\sigma_h H). \tag{2.19}$$

Here, $\lambda = \sigma_e/\sigma_h$ is a constant. It can be seen that Kohler's rule holds. However, it should be noted that this rule can be violated if τ is strongly carrier dependent.

2.3 Anomalous transport properties near quantum critical point

As mentioned in Chapter 1, the NFL behaviors have been observed in the correlated materials at near the QCP. Among them, some common features in the charge transport properties have been recognized. In this section, these experimental results are briefly reviewed, particularly in cuprates, iron-pnictides, and heavy-fermion compounds.

2.3.1 Linear-in-temperature resistivity

One of the most well known NFL behaviors is a resistivity that varies linearly with temperature, i.e.,

$$\rho(T) = \rho_0 + AT^\alpha, \alpha = 1. \tag{2.20}$$

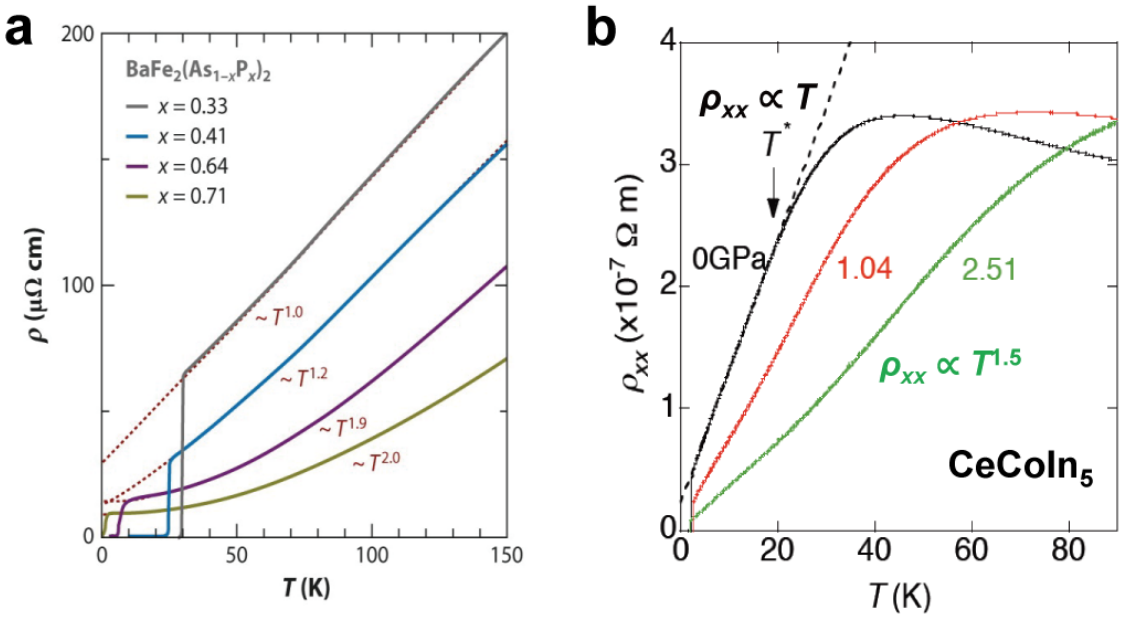

Figure 2.1: **a** Temperature dependence of resistivity for $BaFe_2(As_{1-x}P_x)_2$ [76]. **b** Temperature dependence of resistivity for heavy fermion superconductor $CeCoIn_5$ [77]. In this type of compound, the f-electrons start to couple with the conduction electrons at below $T_{\rm coh}$ and become itinerant. At ambient pressure, the resistivity exhibits T-linear dependence at below $T^* \approx T_{\rm coh}/2$.

This is initially noted in cuprate superconductors. Early experiments on optimally doped materials show that the T-linear behavior of resistivity extends over a broad temperature range, ranging from an extremely high temperature down to $T_{\rm c}$ [73, 74]. Note that the conventional electron-phonon scattering can also give rise to T-linear resistivity at $T >> \Theta_D$, where Θ_D is the Debye temperature. However, this mechanism is unlikely to be the origin in the cuprates because the T-linear resistivity discussed here starts from a much lower temperature, i.e., $T < \Theta_D/5$ [75].

Since then, the T-linear resistivity has also been observed in iron-pnictides and heavy fermion compounds. The optimally doped $BaFe_2(As_{1-x}P_x)_2$ and $CeCoIn_5$, which have AFM QCP at $x \sim 0.3$ and $P_{\rm c} \sim 0$ Pa, respectively, are two such examples [76, 77]. In Fig. 2.1a, we show the $\rho(T)$ profiles of the over-doped iron pnictide $BaFe_2(As_{1-x}P_x)_2$. At $x = 0.33$, which is near the AFM QCP, the resistivity shows linear-in-temperature dependence at above T_c. As the concentration of P increases, the T-linear dependence of

resistivity gradually evolves into the T^2 temperature dependence ($x > 0.64$), indicating a change into a Fermi liquid state. In Fig. 2.1b, we show an example of a heavy fermion compound $CeCoIn_5$. Similar to the $BaFe_2(As_{1-x}P_x)_2$ system, the T-linear dependence of the resistivity is also observed within the vicinity of the AFM QCP.

Planckian limit

In addition to the temperature dependent behavior, the resistivity also shows an anomaly in the scattering rate $1/\tau$ [78–80]. In Ref. [78], the authors estimate the scattering rate within the T-linear regime of the resistivity through

$$\frac{1}{\tau} = \frac{e^2\rho}{hd}\sum_i k_{Fi}v_{Fi} \tag{2.21}$$

for two-dimensional materials. Here, d is the distance between the layers and the summation is over all Fermi pockets i, and h is the Planck constant. Information on the Fermi wave vector k_{Fi} and Fermi velocity k_{Fi} can be obtained from other experiments, such as ARPES, the specific heat, and de Haas-van Alphen (dHvA) measurements. The

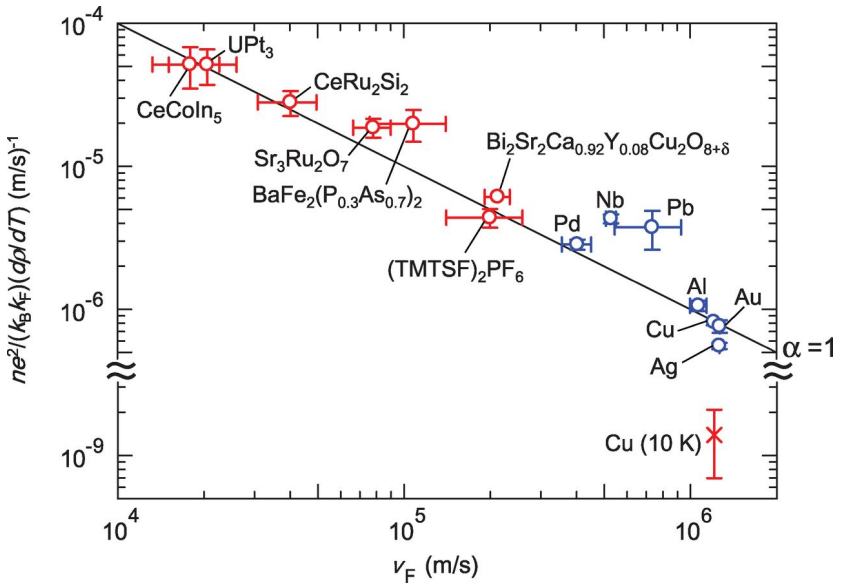

Figure 2.2: The averaged $ne^2/(k_Bk_F)(d\rho/dT)$ plotted as a function of the averaged Fermi velocity v_F for many different types of materials [78]. According to the one-band Drude model, $ne^2/(k_Bk_F)(d\rho/dT) = \alpha/v_F$. The black line corresponds to $\alpha = 1$.

results are summarized in Fig. 2.2. Interestingly, for various kinds of the correlated materials, including cuprates, iron-pnictides, heavy fermion compounds, and organic superconductors, the estimated scattering rates are near the Planckian limit, i.e.,

$$\frac{\hbar}{\tau} = \alpha k_{\mathrm{B}} T, \alpha \sim 1. \tag{2.22}$$

It was suggested that $\alpha \sim 1$ is a universal upper limit for the T-linear scattering rate [78–80]. Indeed, even in normal metals, where the dominated phonon scattering causes T-linear resistivity at high temperatures, $\alpha \sim 1$ is also observed. Although the underlying reason for the universal scattering rate is still unknown, this empirical finding provides a new insight into the problem [78, 81].

2.3.2 Unusual Hall effect

The Hall effect also shows interesting deviations from the Fermi liquid behavior. In cuprates within optimally doped and underdoped regimes, iron pnictides, and heavy fermion superconductors, R_{H} exhibits a strong temperature dependence. Fig. 2.3 shows examples of these three classes of correlated materials. As the temperature is lowered, $|R_{\mathrm{H}}|$ increases rapidly. At a low temperature, the value of $|R_{\mathrm{H}}|$ is estimated to be much larger than that obtained from a band calculation [76, 77, 82]. Notably, for $BaFe_2(As_{1-x}P_x)_2$ and $CeRhIn_5$, the enhancement of $|R_{\mathrm{H}}|$ at low temperature becomes more pronounced upon approaching the AFM QCP, suggesting the influence of the AFM fluctuations on the Hall effect.

Hall angle

In cuprates, it has been pointed out that the Hall angle $\theta_{\mathrm{H}} \equiv \tan^{-1}(\rho_{xy}/\rho_{xx})$ has a simple temperature dependent form. Fig. 2.4a shows the earlier Hall angle measurements of Zn-doped $YBa_2Cu_3O_{7-\delta}$ (YBCO) [85]. For various Zn-doped samples, the $\cot\theta_{\mathrm{H}}$ follows a T^2 dependence, i.e.,

$$\cot\theta_{\mathrm{H}} = a + bT^2, \tag{2.23}$$

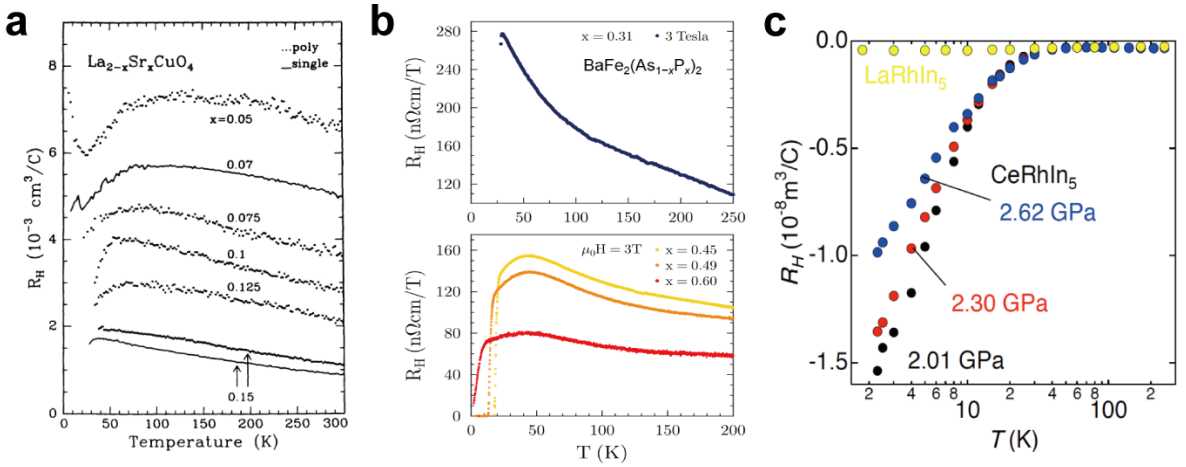

Figure 2.3: **a** Temperature dependence of $R_{\rm H}$ for optimally doped ($x \sim 0.15$) and under-doped $La_{2-y}Sr_yCuO_4$ [83]. For $x = 0.15$, $R_{\rm H}$ increases as $1/T$ with decreasing temperature. **b** Hall data for optimally doped ($x_{\rm c} \sim 0.3$) and over-doped $BaFe_2(As_{1-x}P_x)_2$ [84]. **c** Hall data for $CeRhIn_5$ at several pressures [77]. The AFM QCP of $CeRhIn_5$ is located at ~ 2 GPa. The Hall coefficient for $LaRhIn_5$ at 0 Pa is also plotted. As expected for a Fermi liquid, $R_{\rm H}$ of $LaRhIn_5$ is weakly temperature dependent.

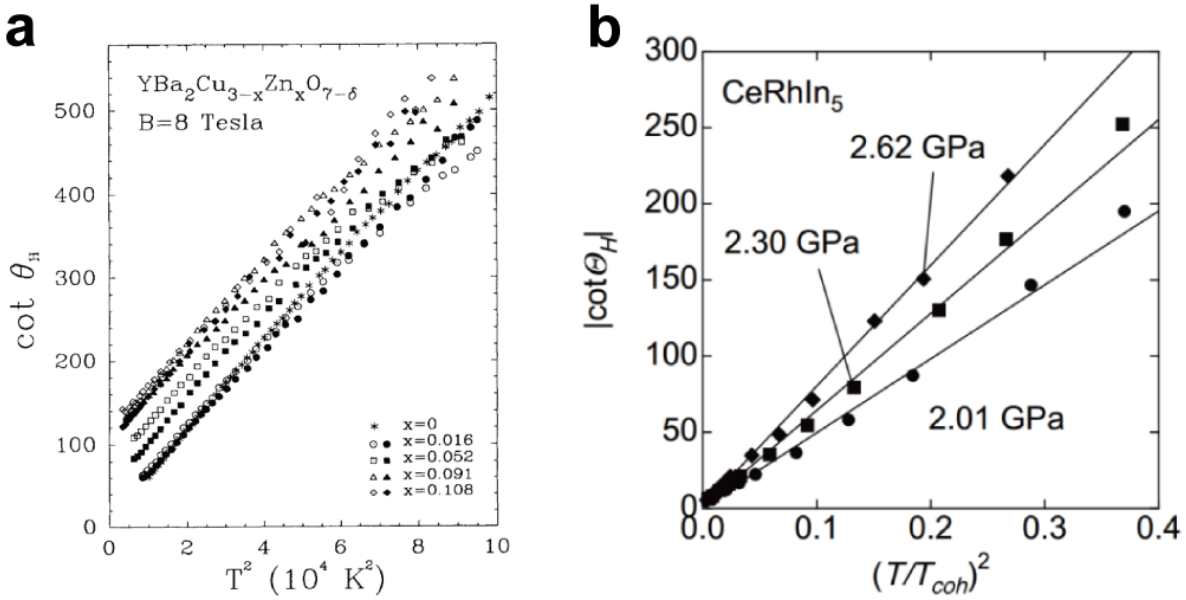

Figure 2.4: **a** Cotangent of Hall angle, i.e., $\cot\theta_{\rm H}$, plotted as a function of T^2 for various Zn-doped YBCO [85]. **b** $|\cot\theta_{\rm H}|$ plotted as a function of $(T/T_{\rm coh})^2$ for $CeRhIn_5$ under several pressure levels [77].

where a and b are constants. Given that $\rho \propto T$, this observation agrees well with the prediction made using a theoretical model in which two different scattering rates are assumed (see section 2.4). In heavy fermion superconductors $CeRhIn_5$ and $CeCoIn_5$ at near AFM QCP, the T^2-dependent $\cot\theta_H$ has also been reported within the T-linear regime of resistivity (Fig. 2.4b). Therefore, this Hall angle behavior, when combined with the T-linear resistivity, is an important hallmark of the NFL behaviors.

2.3.3 Scaling of magnetoresistance

As mentioned in section 2.2, the magnetoresistance in many conventional metals is scaled using Kohler's rule. However, in cuprates, iron pnictides, and heavy fermion compounds, the violation of this scaling relation has been reported [76, 77, 82, 86]. As an example, we show Kohler's plot for underdoped YBCO ($T_c = 60$ K) in Fig. 2.5a. The orbital component of the magnetoresistance is obtained by subtracting the longitudinal magnetoresistance $\Delta\rho/\rho_{\parallel}$ ($\boldsymbol{I} \parallel \boldsymbol{H} \perp c$) from the transverse magnetoresistance $\Delta\rho/\rho_{\perp}$

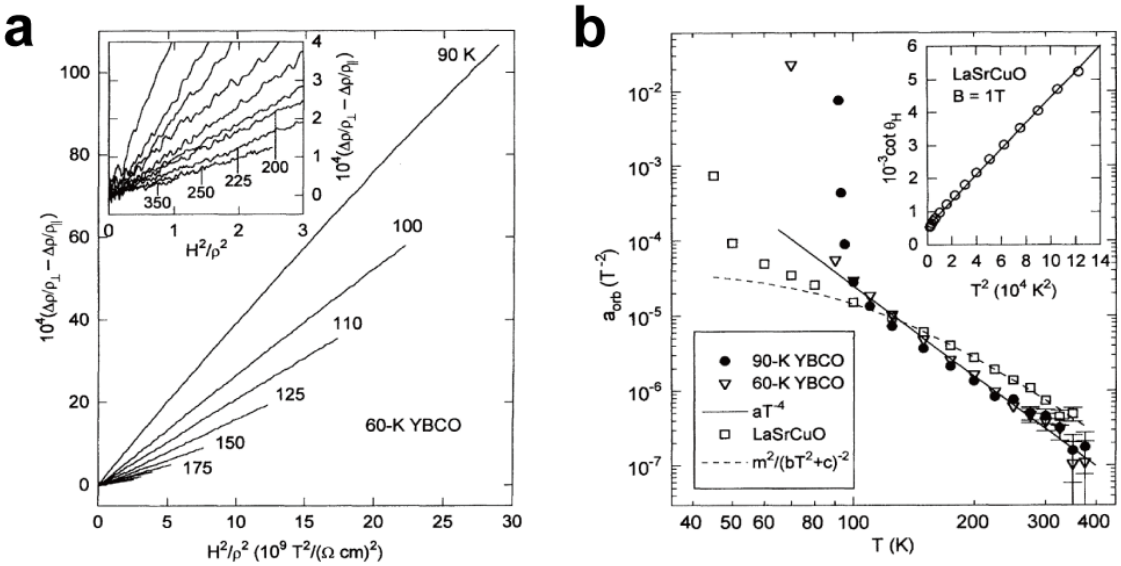

Figure 2.5: **a** The orbital magnetoresistance plotted as a function of $(H/\rho)^2$ for YBCO ($T_c = 60$ K). The inset shows the same plot at higher temperature. **b** The temperature dependence of the coefficient a_{orb} for $YBa_2Cu_3O_{6.6}$ ($T_c = 60$ K), $YBa_2Cu_3O_7$ ($T_c = 90$ K), and $La_{1.85}Sr_{0.15}CuO_4$ ($T_c = 28$ K). The inset shows the $\cot\theta_H$ plotted as a function of T^2 for $La_{1.85}Sr_{0.15}CuO_4$. Adapted from Ref. [86].

($\boldsymbol{I} \perp \boldsymbol{H} \parallel c$). The distinct curves shown in Fig. 2.5a clearly indicate that Kohler's rule is not obeyed.

To understand the origin of the anomaly in the magnetoresistance, identifying the valid scaling law is important. A new scaling law, which scales the magnetoresistance in term of the Hall angle, i.e.,

$$\frac{\Delta\rho_{xx}(T,H)}{\rho_{xx}(T,0)} \propto \tan^2\theta_{\mathrm{H}}, \tag{2.24}$$

has been reported in cuprates, iron pnictides, and heavy fermion superconductors [76, 77, 86, 87]. Historically, this so-called modified Kohler's rule is first recognized in cuprates [86]. Harris *etal*. measured the magnetoresistance in optimally doped YBCO ($T_{\mathrm{c}} = 90$ K), underdoped YBCO ($T_{\mathrm{c}} = 60$ K), and optimally doped LSCO ($T_{\mathrm{c}} = 38$ K). In these materials, the orbital part of transverse magnetoresistance is found to vary quadratically with the field, i.e., $\Delta\rho_{xx}/\rho_{xx} \sim a_{\mathrm{orb}}H^2$. The temperature dependence of the coefficient a_{orb} for the three samples is shown in Fig. 2.5b. At above ~100 K, the coefficient a_{orb} varies as $\sim aT^4$ for the two YBCO samples and as $\sim m^2/(bT^2+c)^2$ for the LSCO sample. Intriguingly, the authors found that, in these samples, the temperature dependence of the a_{orb} follows that of $\tan^2\theta_{\mathrm{H}}$. This indicates that the magnetoresistance

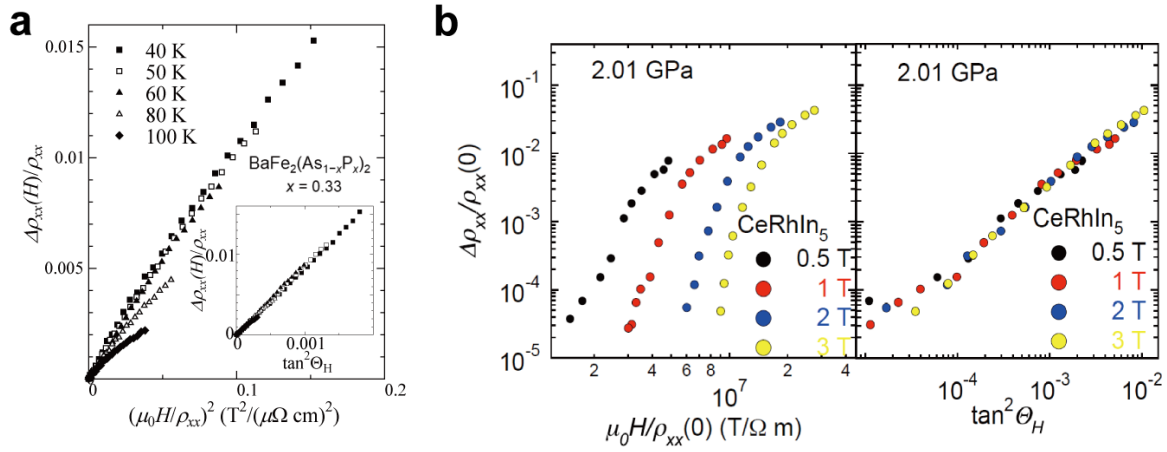

Figure 2.6: **a** Kohler's plot for optimally doped $BaFe_2As_{1-x}P_x$. The inset shows the modified Kohler's plot from the same data [76]. **b** Kohler's plot (left panel) and modified Kohler's plot (right panel) for $CeRhIn_5$ [77].

is proportional to $\tan^2\theta_{\rm H}$, i.e., $\Delta\rho_{xx}/\rho_{xx} \propto \tan^2\theta_{\rm H}$.

2.4 Theoretical studies

Many theoretical models have been proposed to explain these NFL transport properties. Broadly speaking, these theories are classified into two categories:

One category is models based on the NFL physics, in which the carriers are exotic objects. One famous example is Anderson's spin-charge separation model that was originally proposed for cuprates [88]. Here, the elementary excitations of an electron are fractionalized into the spin (spinons) and charge (holons). This introduces two different scattering times for momentum displacements parallel and perpendicular to the Fermi surface. It can be seen that the Hall scattering rate $1/\tau_{\rm H}$ owing to the spinon-spinon scattering varies as T^2, and the transport scattering rate $1/\tau_{\rm tr}$ owing to the backflow of spinons (scattering the holons) varies with T. As a result, the resistivity, Hall angle and magnetoresistance behave as $\rho_{xx} \propto \tau_{\rm tr}^{-1} \propto T$, $\cot^2\theta_{\rm H} \propto \tau_{\rm H}^{-1} \propto T^2$, and thus $\Delta\rho_{xx}/\rho_{xx} \propto \tau_{\rm H}^2 \propto \tan^2\theta_{\rm H}$, respectively. Although this model successfully predicts the transport results in optimal cuprates, it has not explained the evolution of the transport properties with doping [82]. In addition, it is unlikely that this model based on the CuO_2 plane is realized in heavy fermion CeMIn$_5$ (M= Co and Rh) [77].

The other category is models based on the Fermi liquid physics, for which the concept of the Landau quasiparticles is still useful. With this approach, the NFL behaviors arise from the anisotropic scattering times owing to the electron-electron correlations. For example, in the presence of large AFM fluctuations, the Fermi surface regions connected by the nesting vectors $\boldsymbol{q}_{\rm AF}$ are strongly scattered, and hence have unusual short scattering times (see Fig. 4.16). Such Fermi surface regions are called "hot spots." In the simplest case, the unusual Hall effect can be understood as follows: The Fermi surface parts with longer scattering times will short out the transport contribution from the hot spots, and thus the effective carrier density $n_{\rm eff}$ decreases. It therefore follows from $R_{\rm H} = 1/ne$ that $R_{\rm H}$ will enhance. This anisotropic scattering time model can also give rise to the T-linear resistivity and the modified Kohler's scaling of the

magnetoresistance [89, 90]. However, for some materials, such as underdoped YBCO and CeMIn$_5$, it fails to give the quantitatively correct results [91, 92].

It was pointed out that the current vertex correction effect should be included in the Fermi liquid approach [92]. This correlation effect modifies both the magnitude and direction of the currents at the hot spots, significantly influencing the transport properties. The theory quantitatively explains the NFL behaviors observed in cuprate superconductors and CeMIn$_5$. We will consider this effect in chapter 4.

3

Experiments

3.1 Single crystalline samples of $FeSe_{1-x}S_x$

All samples were provided by Prof. Shigeru Kasahara in our group. The details of the crystal growth and characterization are presented in this section.

3.1.1 Crystal growth

The single crystals of $FeSe_{1-x}S_x$ were made through a chemical vapor transport (CVT) method. The Fe, Se, and S powders were mixed with the atomic ratio of $1.1 : 1 - x : x$ and then loaded into an SiO_2 ampoule together with a mixture of KCl and $AlCl_3$ powders (ratio of 3 : 7). In this configuration, the mixture of KCl and $AlCl_3$ serves as the transport agent. The slightly excess of Fe powder can reduce the number of Fe defects. To avoid contamination, this procedure was conducted in a glove box filled with pure Ar gas. The SiO_2 ampoule was subsequently sealed under a high vacuum ($\sim 10^{-4}$ Pa). During the CVT process, one end of the ampoule (so-called source zone) was kept at $\sim$ 390–450 °C, whereas the other end (the so-called deposition zone) was kept at $\sim$ 140–200 °C. After 2–4 weeks, millimeter-sized plate-like single crystals of $FeSe_{1-x}S_x$ can be obtained.

Most of the samples used in this study were cut into a regular shape with typical

sizes of $2 \times 1 \times 0.05$ mm^3, as shown in Fig. 3.1. The actual x values were determined through an energy dispersive X-ray analysis.

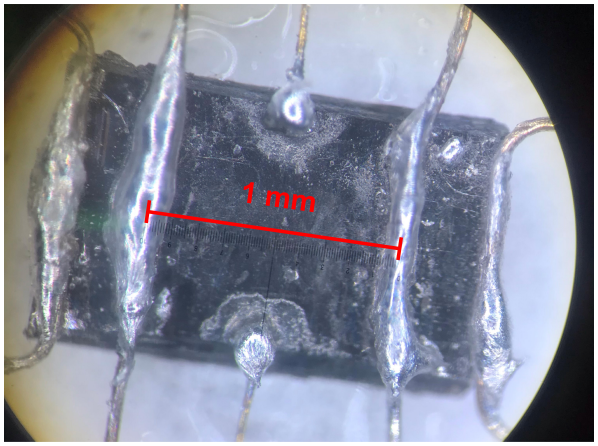

Figure 3.1: Single crystal of $FeSe_{0.82}S_{0.18}$. The contacts were made using indium-soldering.

3.1.2 Characterization

Following the success of crystal growth, we turn our attention to characterizing the grown $FeSe_{1-x}S_x$. There have been several experiments examining the quality of the grown crystals including STM, quantum oscillations, and magnetic susceptibility measurements.

STM

STM is a powerful tool for characterizing a surface. Fig. 3.2 (A to E) shows the STM images of the surfaces of $FeSe_{1-x}S_x$ within a range of $0 \leq x \leq 0.25$ [55]. In pure FeSe, the topmost Se atoms are clearly shown. However, in the S-doped samples, sulfur atoms are imaged as depressions owing to the smaller atomic radius than Se atoms. The locations of sulfur atoms can be determined by analyzing these atomic-resolution topographic images. As shown in Fig. 3.2 (F to J), the red dots that represent S atoms are uniformly distributed. No apparent segregation is observed. These STM results indicate a good homogeneity of crystals obtained through our CVT method.

Quantum oscillations

The observation of quantum oscillations in $FeSe_{1-x}S_x$ confirms the low level of impurities and defects in our sample. Indeed, as one major condition for the observation of quantum oscillations, the broadening of Landau levels owing to impurity scattering should be smaller than the cyclotron energy ($\hbar\omega_c \equiv eB\hbar/m^*$). Thus, only pure crystals with long mean free paths show quantum oscillations. Fig. 3.3 shows the first derivative of magnetoresistance at high magnetic fields [56]. The oscillatory part of the resistivity can be clearly visualized up to $x \sim 0.19$, demonstrating that the crystals are clean and the substituted-sulfur atoms do not act as strong scattering centers.

Magnetic susceptibility

In this study, we picked out samples from the same bathes as those characterized above. This ensures a high quality of our crystals. Before conducting the electrical transport experiments, we measured the low temperature magnetization using a magnetic property measurement system (MPMS) (Quantum Design, Inc.). The results are shown in Fig. 3.4a. For all samples, the measured magnetic susceptibility exhibits a sharp decrease when entering the superconducting state, which indicates the homogeneous nature of our single crystals of $FeSe_{1-x}S_x$.

Residual resistivity ratio

A simple estimation for the degree of purity is the residual resistivity ratio (RRR). Here, we use the ratio $\rho_{xx}(250\ \mathrm{K})/\rho_{xx}(11\ \mathrm{K})$ for the RRR value. In conventional metals, the resistivity at a sufficient high temperature is dominated by the scattering from phonons and seems to not change between samples of specific materials. By contrast, the resistivity at 0 K (i.e., residual resistivity) depends on the purity of the sample. Thus, the higher this ratio is, the lower the number of impurities. As shown in Fig. 3.4b, the RRR values varies between 11 and 30. These values are comparable with those reported in Ref. [62], indicating the high quality of our measured crystals.

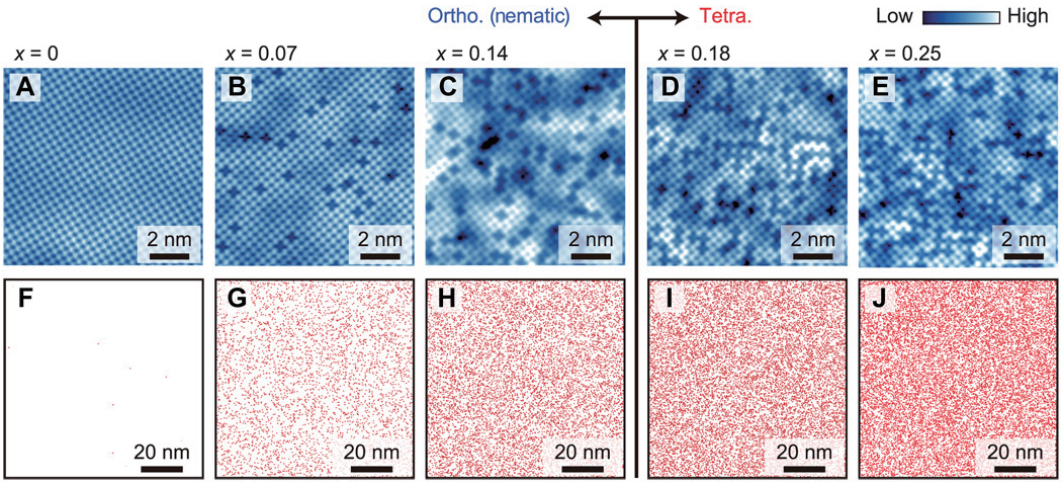

Figure 3.2: Characterization of $FeSe_{1-x}S_x$ by STM [55]. (**A** to **E**) Topographic images of $FeSe_{1-x}S_x$. Sulfur atoms are imaged as depressions. (**F** to **J**) Distributions of sulfur atoms in wider fields of view. Each red dot denotes a sulfur atom.

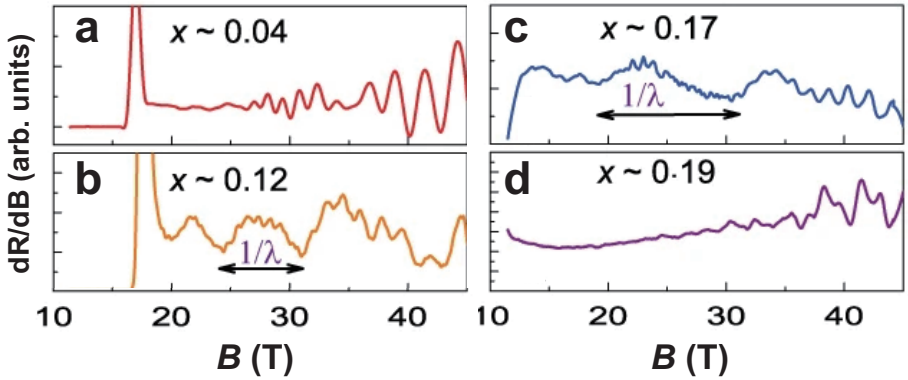

Figure 3.3: The first derivative of magnetoresistance plotted as a function of the magnetic field [56]. The oscillatory part of the resistivity of $FeSe_{1-x}S_x$ can be visualized.

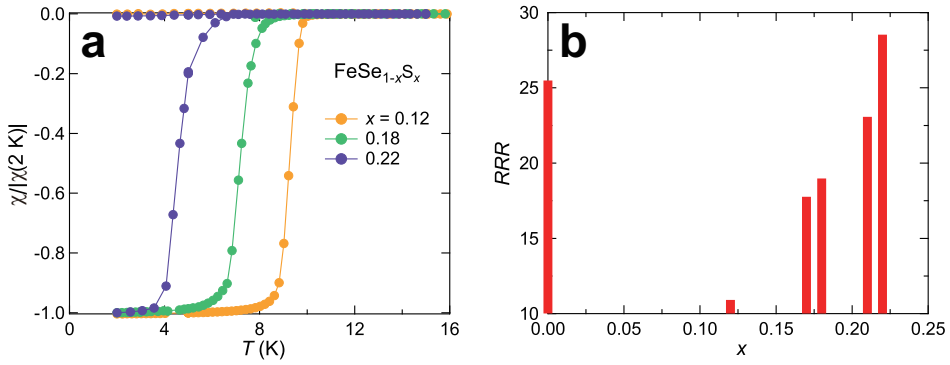

Figure 3.4: **a** Temperature dependence of zero-field-cool and field-cooled magnetization at 5 Oe for $FeSe_{1-x}S_x$. The magnetic fields were applied along the c-axis of $FeSe_{1-x}S_x$. **b** The residual resistivity ratio RRR (defined as $\rho_{xx}(250\ \mathrm{K})/\rho_{xx}(11\ \mathrm{K})$) plotted as a function of x.

3.2 Electrical transport measurements

Preparation

To measure the resistivity and Hall resistivity in the same cooling run, we made six contacts on each sample (Fig. 3.1). To obtain good electrical contacts, we soldered Ag/Au wires with indium onto the sample. A soldering iron with a small tip ($\sim$ 0.3 mm) is used. To avoid the possible damage to the sample surface, we used a non-acid flux to remove the oxidized surface and kept the soldering temperature at $\sim$ 200 °C (the melting point of indium is 156 °C). The resulting contact resistance is less than 100 mΩ. Note that using the usual silver paste technique may result in a resistance of several kilo-ohms owing to the oxidized surface of the $FeSe_{1-x}S_x$. After the soldering, we washed the sample with acetone and/or ethyl alcohol to remove the residual flux.

The dimensional factors, i.e., l, w and t (where l is the distance between the longitudinal voltage contacts and w, t are width and thickness of a crystal, respectively.), are measured using optical microscopy (Leica M205C). The ruler etched on the optical microscopy allows us to resolve the factors within an accuracy of 10 μm.

The samples were then put onto the measurement cell. As illustrated in Fig. 3.5, one end of the sample is fixed to a Ag heat bath using Ag paste. To monitor the temperature of the sample, we thermally connect one inner voltage lead to the Cernox thermometer through an Ag wire (with the Cernox thermometer fixed to a Kapton tube). Actually, this setup was originally designed to measure the kappa, seebeck, and Nernst coefficients. Here, it is used to measure the resistivity, Hall resistivity, and magnetoresistance.

Magnets and Cryogenics

Because $FeSe_{1-x}S_x$ has a relatively high T_c, the lowest temperature needed is $\sim$ 2 K. This temperature can be achieved through our superconducting magnet system (SM6). Fig. 3.6 shows a schematic of SM6. The variable temperature insert (VTI) is connected to helium (He) reservoir through the capillary. By adjusting the needle

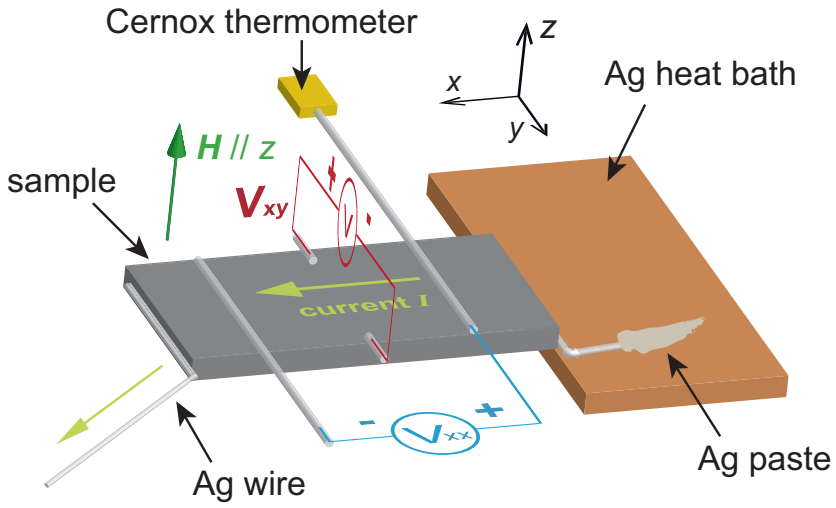

Figure 3.5: Schematic of the setup used for electrical transport measurements.

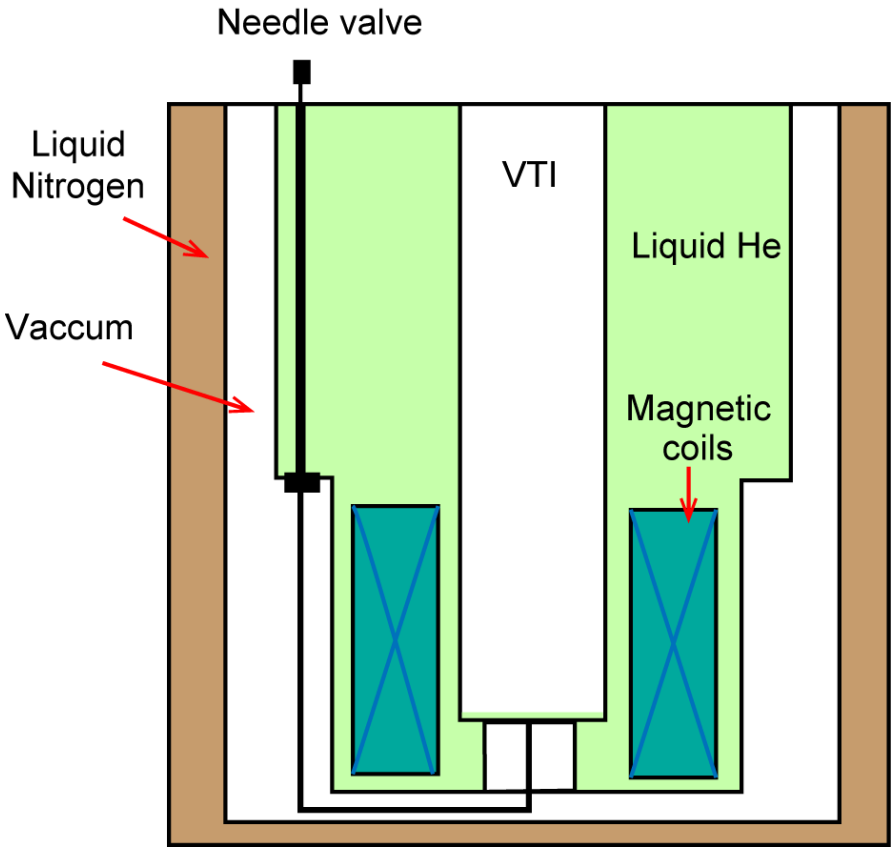

Figure 3.6: Schematic used in superconducting magnet system.

value and pumping, the sample can be cooled to $\sim$ 1.6 K. The superconducting coils are submerged in the liquid He and can generate a magnetic field in the longitudinal direction. Outside the vacuum jacket, there is a liquid nitrogen reservoir that can reduce the heat radiation from the helium reservoir.

Measurement

We used Labview Programs (National Instruments, Inc.) to control the measurements and acquire the data. Each component is connected through a General Purpose Interface Bus (GPIB) interface. Fig. 3.7 shows a schematic of the circuit. Because the computer and magnetic controller can produce noise, we electrically isolated them from the other measurement components using a GPIB-120A bus expander/isolator (National Instruments Inc).

The temperature measurement and control are regulated using Labview software. The software obtains the Cernox thermometer resistance measured through an Model 350 Temperature Controller (LakeShore Cryotronics, Inc.) and converts the resistance into temperature. To stabilize the temperature, the software set the heater power on the sample stage with a 7651 dc current source (Yokogawa, Inc.).

To measure the resistivity and Hall effect, we used the AC resistance bridge Model 372 paired with a Model 3780 preamp (LakeShore Cryotronics, Inc.) or the delta model method applying a Model 6200/2182A combination (Keithley Instruments, Inc.). The choice depends on the signal-to-noise ratio. In addition, for all measurements, electrical currents $\boldsymbol{I}$ of up to 3 mA were used to avoid self-heating.

When measuring the Hall effect and magnetoresistance, we cannot ignore the misalignment of the contacts. Indeed, in practice, the contacts are not perfectly aligned in the transverse (longitudinal) direction perpendicular (parallel) to the current flow. As a result, the actual measured voltage contains both the longitudinal and transverse components. To overcome this problem, we sweep the magnetic field from positive to negative and then antisymmetrize (symmetrize) the data to cancel the longitudinal (transverse) component of the measured voltage. Therefore, the electrical and Hall

voltage can be calculated as

$$V_{xx}(|H|) = \frac{V_{xx}(H) + V_{xx}(-H)}{2}, \tag{3.1}$$

$$V_{xy}(|H|) = \frac{V_{xy}(H) - V_{xy}(-H)}{2}. \tag{3.2}$$

We then obtain the electrical and Hall resistivity as follows:

$$\rho_{xx}(|H|) = \frac{V_{xx}(|H|)}{I}\frac{wt}{l}, \tag{3.3}$$

$$\rho_{xy}(|H|) = \frac{V_{xy}(|H|)t}{I}, \tag{3.4}$$

where I is the electrical current, l is the distance between the longitudinal voltage contacts, and l, w are the width and thickness of a crystal, respectively.

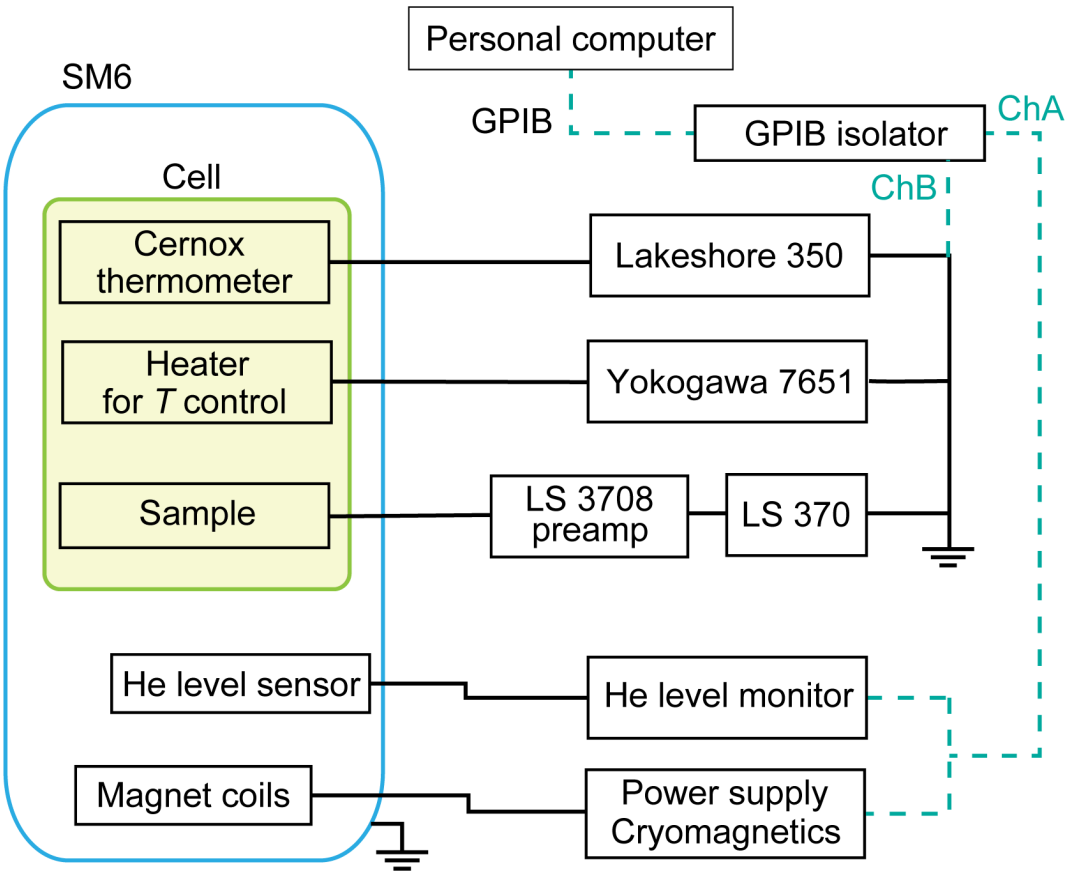

Figure 3.7: Schematic of the circuit for electrical transport measurements.

4

Evolution of charge transport properties across the nematic quantum critical point of $FeSe_{1-x}S_x$

4.1 Resistivity

4.1.1 Temperature dependence of zero-field resistivity

Fig. 4.1a shows the temperature dependence of the resistivity ρ_{xx} normalized by ρ_{xx} at 250 K in a zero field for a series of $FeSe_{1-x}S_x$. For $x = 0$, ρ_{xx} has a kink at $T_s \approx 90$ K owing to the nematic transition. As the concentration of S increases, T_s is suppressed to ~ 62 K for $x = 0.12$ and finally disappears for $x \geq 0.17$, indicating that the system is in a tetragonal phase.

The evolution of the transition temperature T_s can be more clearly seen in the temperature derivative of the resistivity, as shown in Fig. 4.1b. For $x = 0$ and 0.12, the nematic transition temperature T_s is accurately determined by the dip position. For $x = 0.17$ and 0.18, the derivative curves evolve more smoothly. No obvious anomalies are observed. We believe these two samples are near the nemtaic QCP. For $x = 0.22$, no anomalies are observed as well.

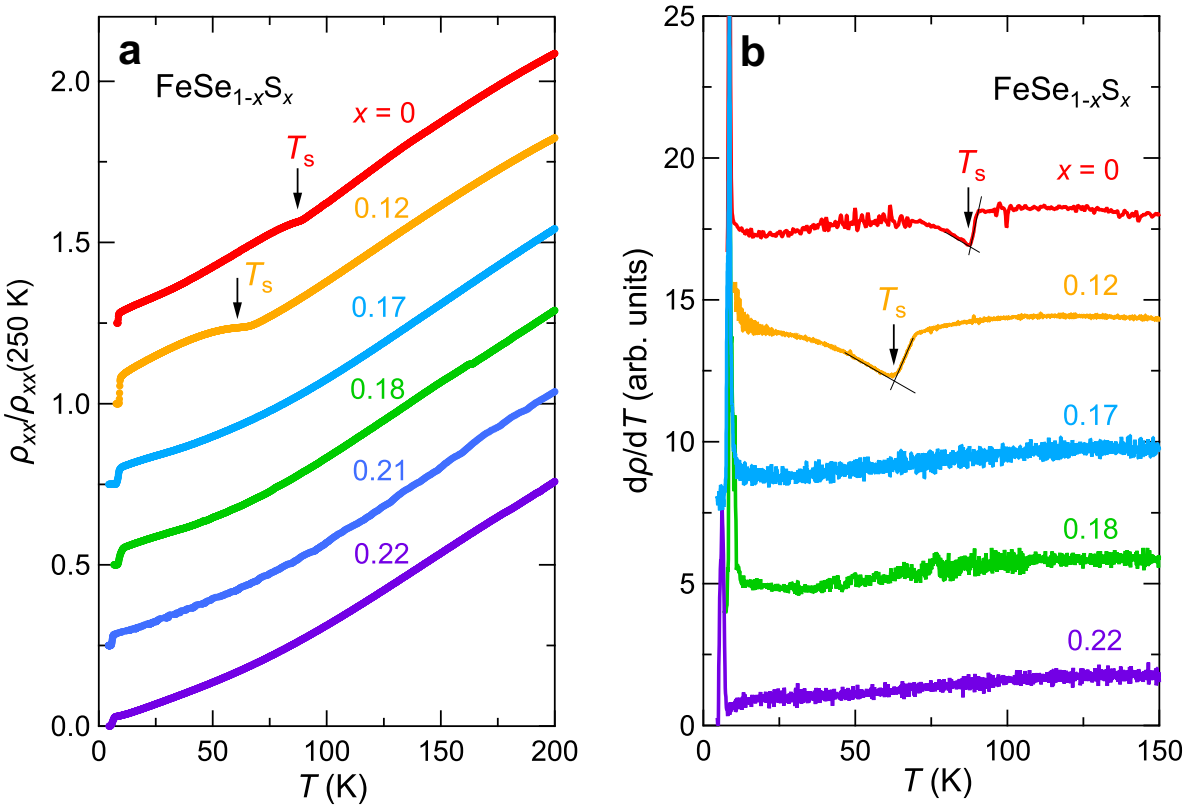

Figure 4.1: **a** Temperature dependence of the resistivity ρ_{xx} normalized by ρ_{xx} at 250 K in zero field of $FeSe_{1-x}S_x$ for various S substitution levels [93]. The arrows indicate the nematic transition temperature T_s. Data are shifted vertically for clarity. **b** The derivative of the resistivity with respect to temperature. The nematic transition temperature T_s is defined by the dip position.

4.1.2 Low temperature resistivity

We now focus on the resistivity below 40 K, where the temperature is sufficiently below the Fermi energy of each pocket (see section 4.1.3). Fig. 4.2 depicts the low temperature behavior of ρ_{xx} for $FeSe_{1-x}S_x$. The most distinct feature is the linear-in-temperature resistivity typical to the NFL behavior down to low temperatures at $x = 0.17$ and 0.18, at or slightly above the nematic QCP. For $x = 0.22$, the T-linear dependence of the resistivity changes to approximately the T^2-dependence as expected for a Fermi liquid at lower temperatures. Similar behavior has been reported by several other groups [62, 94].

The crossover from the NFL to the Fermi liquid can be more clearly seen in the

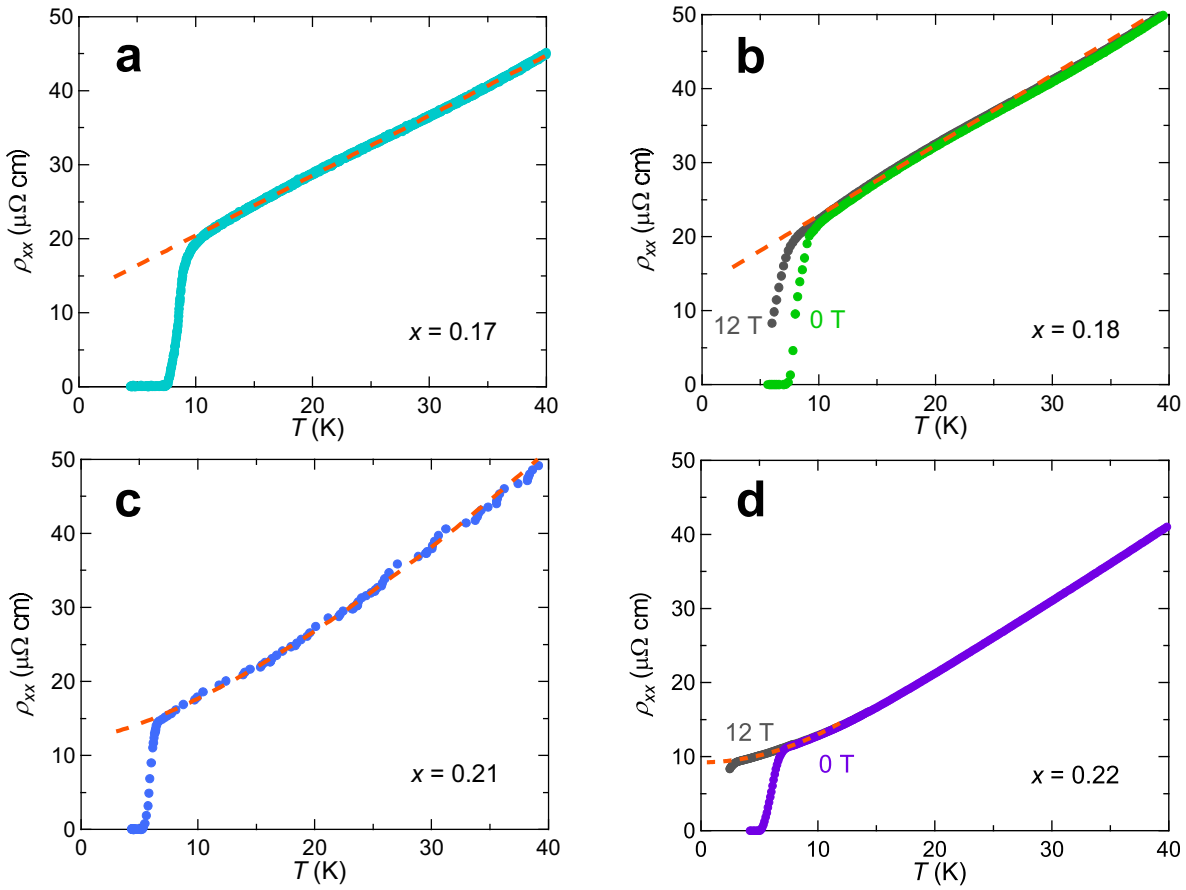

Figure 4.2: Temperature dependence of zero-field resistivity for $FeSe_{1-x}S_x$ at below 40 K [93]. **a** Zero field resistivity at temperature of below 40 K for $x = 0.17$. The red dashed line represents a line fitted by $\rho_{xx} \propto T$. **b** The same plot in the zero field and at $\mu_0 H = 12\ T$ applied parallel to the ab plane for $x = 0.18$. The red dashed line represents a line fitted by $\rho_{xx} \propto T$. **c** The same plot in the zero field for $x = 0.21$. The red dashed curve represents a fitting curve $\rho_{xx} \propto T^{1.5}$. **d** The same plot in the zero field for $x = 0.22$. The red dashed curve represents a fitting curve $\rho_{xx} \propto T^2$.

color plot of the exponent α in the T-dependence of the resistivity,

$$\rho_{xx} = \rho_0 + AT^{\alpha} \tag{4.1}$$

shown in Fig. 4.3. Blue and red show the regions in which the Fermi liquid ($\alpha \approx 2$) and NFL ($\alpha \approx 2$) behaviors are observed, respectively. In the nematic regime below T_s, the T-dependence of ρ_{xx} exhibits a concave downward curvature, which is likely to be caused by a change in the carrier scattering time τ associated with orbital ordering

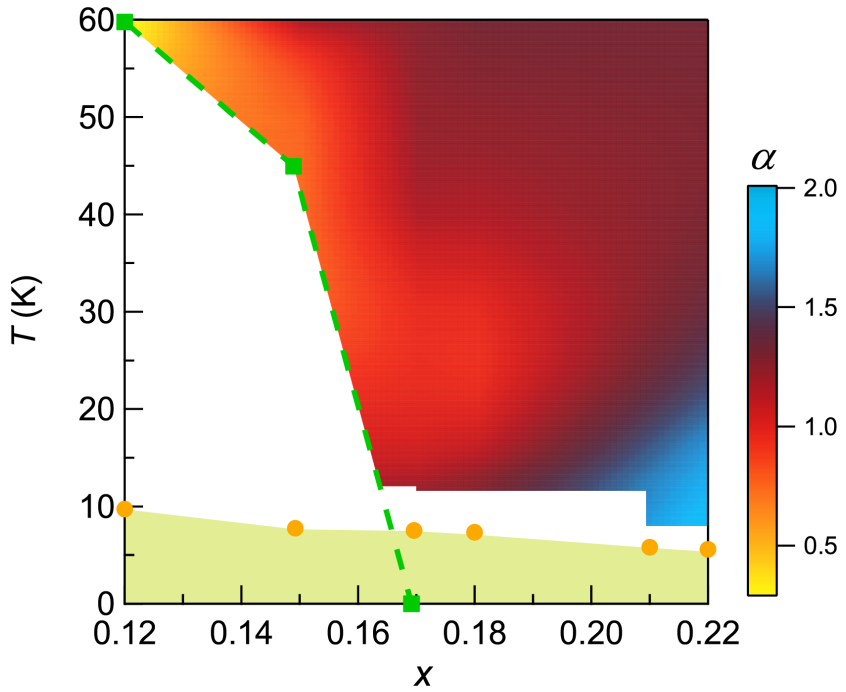

Figure 4.3: Phase diagram of $FeSe_{1-x}S_x$ [93]. The colors in the tetragonal state represent the evolution of the exponent α in the resistivity fitted by Eq. 4.1. The green dashed line represents the tetragonal-orthorhombic (nematic) transition temperature T_s determined by the resistivity measurements. Solid orange circles represent the superconducting transition temperature. The T-dependent exponent $\alpha(T)$ is estimated by the logarithmic derivative of the measured quantity, i.e., $\alpha(T) = d\ln[\rho(T) - \rho_0]/d\ln T$. The ρ_0 values are estimated by the extrapolation of the zero-field resistivity (see the dashed red lines in Fig. 4.2). The resulting $\alpha(T)$ curves are highly smoothed for the color plot.

at T_s. We do not discuss the temperature dependence of ρ_{xx} at below T_s in detail. The Fermi liquid regime with $\alpha \approx 2$ is seen within the low temperature regime at large x values. The phase diagram also includes a funnel of T-linear resistivity centered on $x \approx 0.17$, indicating that the critical fluctuations originating from the nematic QCP extend up to a finite temperature.

4.1.3 Planckian limit

In addition to the temperature dependence of the resistivity, the absolute magnitude of the scattering rate is also an important quantity. In cuprates and other correlated

systems, the T-linear scattering rate reaches the Planckian limit, where $\hbar/\tau = \Lambda k_B T$ with $\Lambda \approx 1$ is fulfilled, despite the different nature of the QCP (see chapter 2). If this empirical fact is the fundamental principle, new theoretical approaches are needed to understand how it works.

To examine whether $FeSe_{1-x}S_x$ is within the Planckian limit, we use a standard Fermi-liquid approach to estimate $\hbar/\tau$, as in Ref. [80]. From the Drude expression for the two-dimensional system (see Eq. 2.21), we can obtain the following expression:

$$\frac{d(\hbar/\tau)}{dT} = \frac{e^2}{2\pi d} \sum_i k_{Fi} v_{Fi} \frac{d\rho}{dT}. \tag{4.2}$$

Here, d is the interlayer distance and the summation is over all the pockets i. Note that the scattering rate $1/\tau$ is linear-in-temperature dependent, i.e., $\hbar/\tau = \Lambda k_B T$, when $\rho_{xx} = \rho_0 + AT$. Given that $\varepsilon_F^i = (\hbar/2)(k_{Fi} v_{Fi})$, this expression is reduced to the following:

$$\Lambda(\frac{h}{2e^2}) = \sum_i \frac{A}{d}(\frac{\varepsilon_F^i}{k_B}), \tag{4.3}$$

where A is the slope of the T-linear resistivity.

Next, we estimate Λ for the sample near the nematic QCP ($x = 0.17$). First, we try to obtain the Fermi energies from other experiments. In FeSe in the nematic phase, the Fermi energies of both the hole and the electron pockets are extremely small: $\varepsilon_F^h \approx 10$ meV and $\varepsilon_F^e \approx 5$ meV, respectively (see section 1.4.2). As the concentration of S increases, ε_F^h increases gradually without exhibiting an abrupt change at the nematic QCP [55]. In the tetragonal phase at $x \geq 0.17$, the Fermi surfaces consist of two hole and two electron pockets [95, 96]. The ARPES measurements report $\varepsilon_F^h \approx 14$ meV for both hole pockets [97]. However, direct measurements of the electron pockets by ARPES are lacking. As discussed in section 1.5.2, the Fermi surface of $FeSe_{1-x}S_x$ evolves smoothly when crossing the nematic QCP, no dramatic change in Fermi wave vectors and Fermi velocities is observed. Therefore, we speculate that the Fermi energy for both electron pockets is on the order of 5−15 meV. Here, for simplicity, we assume that $\varepsilon_F^{e,h} \sim 10 - 15$ meV for all pockets. In addition, from the T-linear resistivity of

$x = 0.17$, $A \approx 1.0$ $\mu\Omega$cm/K is obtained. By using these values, we obtain $\Lambda = 0.7 - 0.9$ from Eq. 4.3. An earlier analysis of the coefficient of the T-linear resistivity also found that $\Lambda \sim 1$ [60], implying that scattering within the quantum critical fan of a nematic QCP is indeed close to the Planckian limit. A comparison of the estimated value of Λ with those reported in other correlated materials is shown in Fig. 4.4.

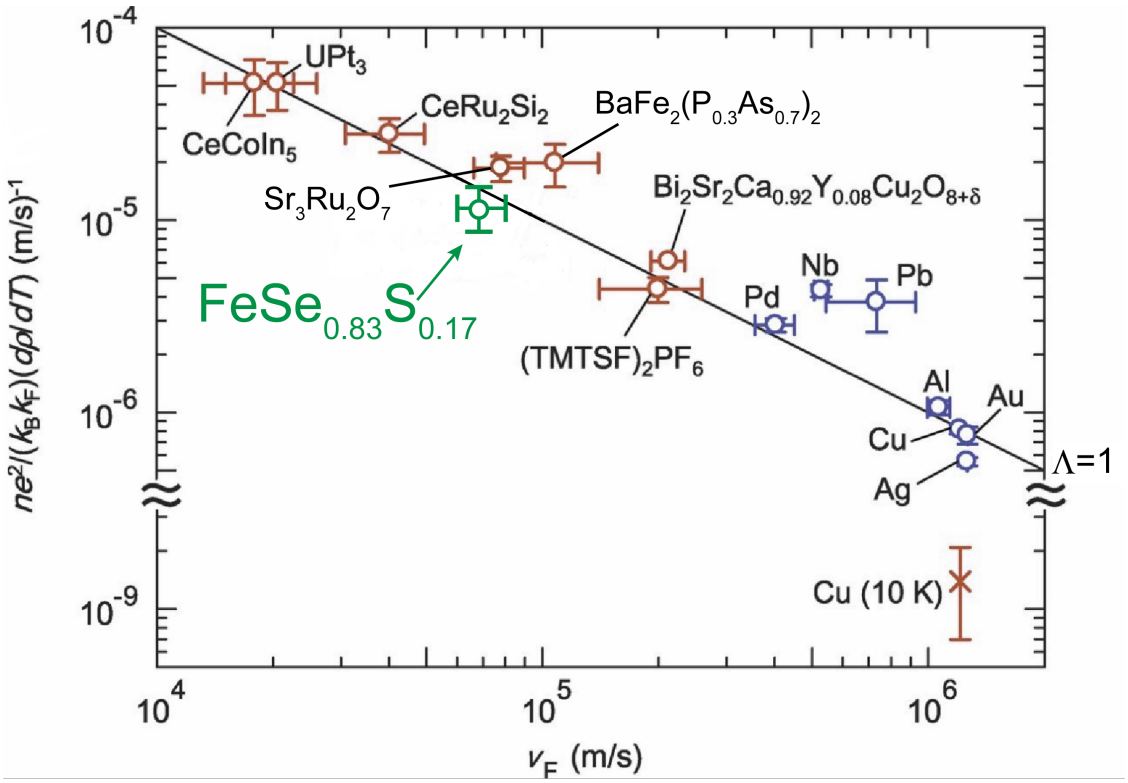

Figure 4.4: A comparison of our estimated value of Λ in $FeSe_{0.83}S_{0.17}$ with those reported in other materials that present T-linear resistivity. The averaged Fermi velocity of $FeSe_{0.83}S_{0.17}$ is estimated from the STM measurements [55]. Adapted from Ref. [78].

4.2 Hall effect

Because S-doped FeSe is a multiband system, it is important to find other evidence of NFL transport behaviors in addition to the T-linear resistivity. Therefore, we measured the Hall effect and magnetoresistance across the nematic QCP of $FeSe_{1-x}S_x$. In this section, the Hall results are described. The magnetoresistance results are presented in

the following section.

4.2.1 Hall resistivity at low fields

Fig. 4.5 and 4.6 show the magnetic field dependence of Hall resistivity ρ_{xy} up to 7 T at several doping levels. The field is parallel to the c axis.

Fig. 4.5 displays ρ_{xy} for $x = 0.12$. At above 50 K ($T_s \approx 62$ K), ρ_{xy} has a positive sign and shows a linear-in-field dependence. Note that in a compensated two-band model, the Hall resistivity varies linearly with increasing magnetic field (see Eq. 2.14). In contrast, at a temperature of below 50 K, inside the nematic phase, ρ_{xy} shows a non-linear field dependence, changing the sign from negative to positive at a higher field. It has been pointed out that the compensated three-band model with an additional high mobility small electron pocket can describe this non-linear behavior. However, the origin of this small pocket is still under debate. One possible reason is the emergence of the Dirac-cone like pockets at the corner of the Brillouin zone owing to the band shifts in a nematic state [98, 99]. We do not discuss this herein. A related discussion can be found in Refs. [37, 100, 101].

For samples with $x \geq 0.17$, ρ_{xy} exhibits H-linear dependence in the present temperature and magnetic field regions, as shown in Fig. 4.6 (b-e), reflecting the compensate nature of the materials. Another common feature in the tetragonal samples is the sign of ρ_{xy} being positive at below 100 K, indicating the dominate contribution from the hole bands. In addition, it is worth mentioning that these ρ_{xy} behaviors are extremely similar to that of the $x = 0.12$ sample within the tetragonal regime.

4.2.2 Temperature dependence of Hall coefficient

By estimating the zero-field slope of ρ_{xy} at each temperature, we can obtain the temperature profile of Hall coefficient R_{H} (Here, $R_{\mathrm{H}} \equiv \lim_{H\to 0} \frac{d\rho_{xy}}{dH}$). The R_{H} curves for a range of x are depicted in Fig. 4.7.

For $x = 0.12$, within the tetragonal regime, R_{H} increases as the temperature decreases. Below the nematic transition temperature T_s, it rapidly decreases to a nega-

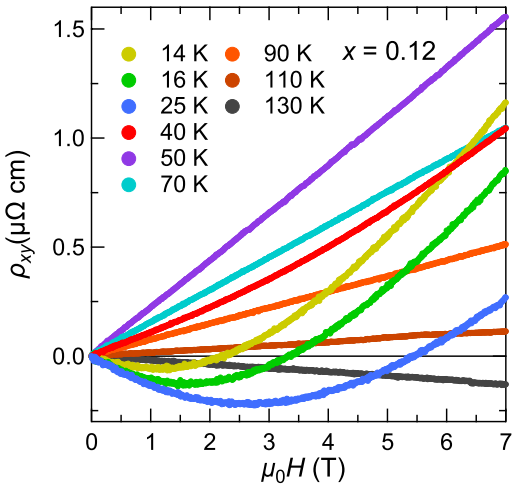

Figure 4.5: Field dependence of the Hall resistivity ρ_{xy} for $x = 0.12$ at different temperatures. At below T_s, ρ_{xy} becomes nonlinear.

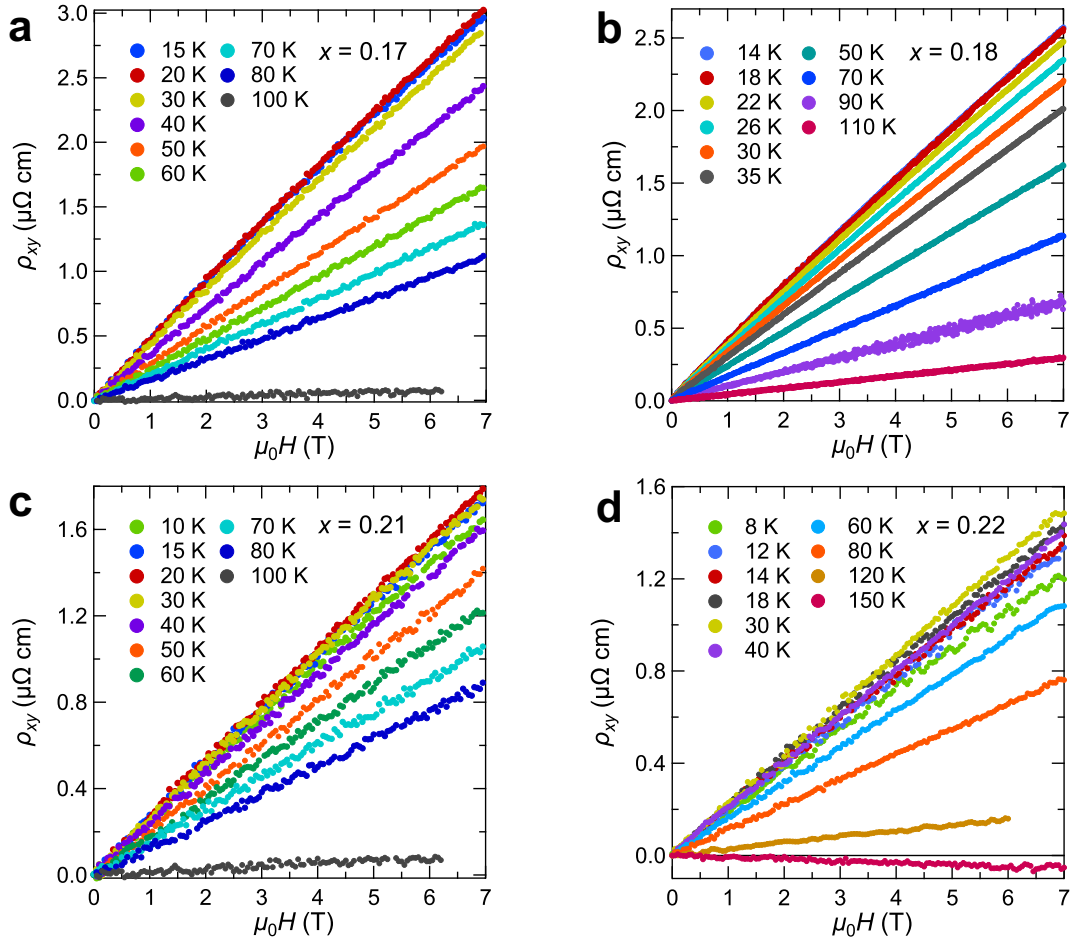

Figure 4.6: Field dependence of the Hall resistivity ρ_{xy} for $x =$ **a** 0.17, **b** 0.18, **c** 0.21, and **d** 0.22. In tetragonal samples, ρ_{xy} varies linearly with an increasing field.

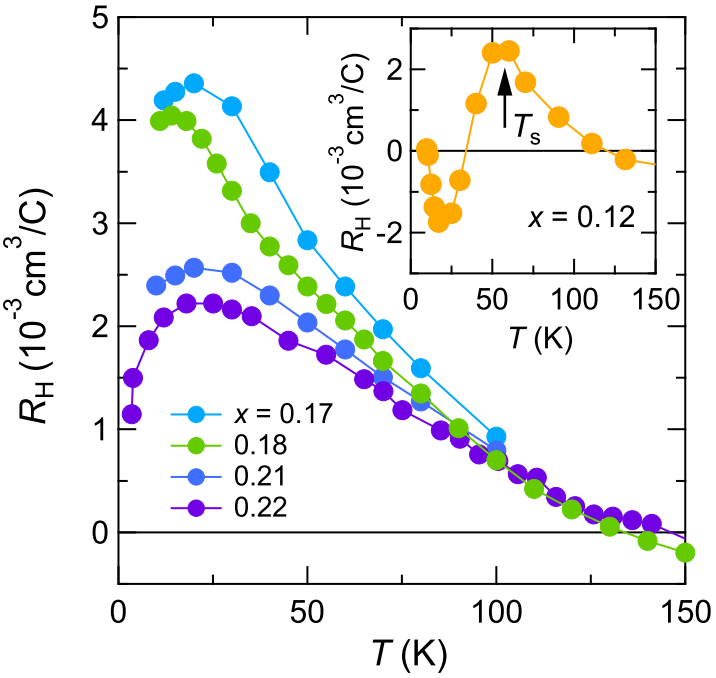

Figure 4.7: Temperature dependence of the Hall coefficient R_H for $x \geq 0.17$ [93]. The inset shows R_H for $x = 0.12$. The nematic transition temperature T_s is indicated by the black arrow.

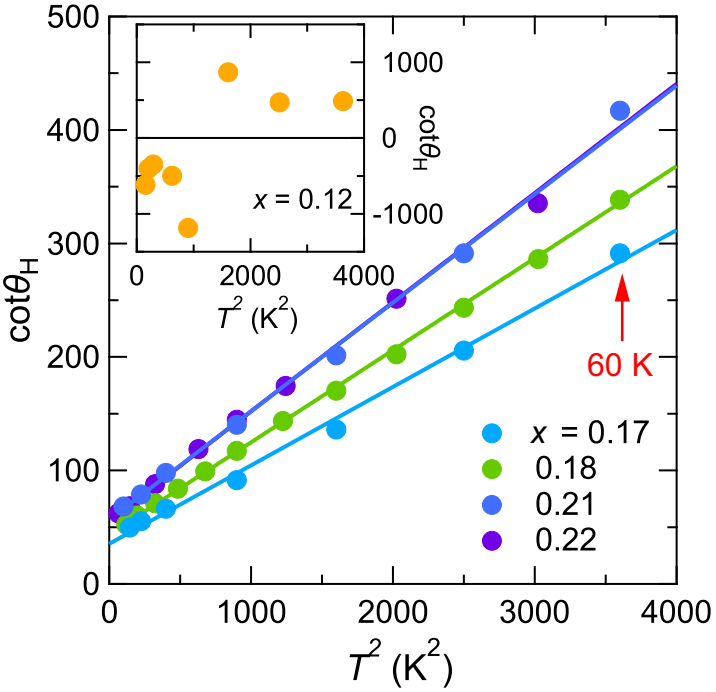

Figure 4.8: Cotangent of the Hall angle, cotθ_H, plotted as a function of T^2 for $x \geq 0.17$ at below 60 K [93]. The color lines are simply visual guides. Inset: the same plot for $x = 0.12$.

tive value and shows a minimum at lower temperatures. The drop of R_{H} indicates the growing contribution of the electron carriers to the transport properties in the nematic phase.

For the tetragonal samples ($x \geq 0.17$), the temperature dependent behaviors are similar to each other. At high temperatures, R_{H} is close to zero, reflecting nearly equal mobilities of the electron and hole carriers. As the temperature goes down, it increases rapidly. Slightly above T_c, at proximal 25 K, a maximum value is shown followed by a decrease. The behavior of R_{H} is complex. Here, we only note that the absolute values of R_{H} at low temperatures are enhanced when approaching the nematic QCP ($x = 0.17$), which might be attributed to the critical nematic fluctuations.

4.2.3 Hall angle

As mentioned in Chapter 2, in some cuprates and heavy fermion compounds, the Hall problem can be simplified by analyzing the Hall angle. In these materials, the cotangent of the Hall angle, $\cot\theta_{\mathrm{H}}$, is proportional to T^2. Following the same procedure, we plot the Hall angle as a function of T^2, as depicted in Fig. 4.8. Here, the cotangent of the Hall angle is defined as

$$\cot\theta_{\mathrm{H}} \equiv \frac{\rho_{xx}(0)}{R_{\mathrm{H}} \times 1\,\mathrm{T}} \tag{4.4}$$

The inset of Fig. 4.8 displays the Hall angle behavior for a 12% S-doped sample. It has a change in sign and does not vary as T^2. By contrast, for the samples with $x \geq 0.17$, the cotangent of the hall angle varies as T^2 at below 60 K. It should be noted that this Hall angle behavior cannot be described by the compensated two-band model if the T-linear resistivity is involved (see section 4.4.1). Thus, the simultaneously observed quadratic temperature dependence of $\cot\theta_{\mathrm{H}}$ and the T-linear resistivity in the tetragonal samples are important evidence of the NFL behavior.

4.3 Magnetoresistance

4.3.1 Transverse magnetoresistance

Figs. 4.9 and 4.10 show the field dependence of the normalized magnetoresistance, $\Delta\rho_{xx}/\rho_{xx}(0) \equiv [\rho_{xx}(H) - \rho_{xx}(0)]/\rho_{xx}(0)$, for a range of x at up to 7 T. The magnetic field $\boldsymbol{H}$ is parallel to the c-axis, whereas the current $\boldsymbol{I}$ is in the ab plane. The transverse magnetoresistance is positive for all samples at below 70 K.

To obtain a qualitative understanding of the field-dependent behavior of the transverse magnetoresistance, we simply fit the data using the formula $\Delta\rho_{xx}/\rho_{xx}(0) = aH^{\beta}$. For $x = 0.12$, the magnetoresistance is roughly $H^{1.52}$ dependent at 14 K and gradually evolves into an H^2 dependence when approaching the tetragonal phase. By contrast, for the tetragonal samples, the magnetoresistance is approximately quadratic field dependent in the present temperature region.

Next, we try to scale the magnetoresistance in terms of Kohler's rule and the modified Kohler's rule. To do so, we need the orbital part of the transverse magnetoresistance, which can be obtained by subtracting the longitudinal from the transverse magnetoresistance. Note that the Lorenze force does not exist in longitudinal geometry ($\boldsymbol{I} \parallel \boldsymbol{H} \perp c$) if the system is two dimensional. As reported in Ref. [60], the longitudinal magnetoresistance of $FeSe_{1-x}S_x$ in the tetragonal samples is negligibly small even at a high field of up to 35 T. To verify this point, we measured the temperature dependence of the resistivity at 12 T with $\boldsymbol{H} \perp c$ for $x = 0.18$ and 0.22. As shown in Fig. 4.2, in both samples, the resistivity at 12 T is nearly the same as its corresponding zero-field value. Thus, we believe that the orbital part of the transverse magnetoresistance is dominant for $x \geq 0.17$. For completeness, we also analyze the scaling behavior of the transverse magnetoresistance for the $x = 0.12$ sample.

4.3.2 Kohler's plot

To see whether the Kohler's rule is obeyed, we plot the magnetoresistance as a function of $(\mu_0 H/\rho_{xx}(0))^2$ for various values of x, as illustrated in Figs. 4.11 and 4.12.

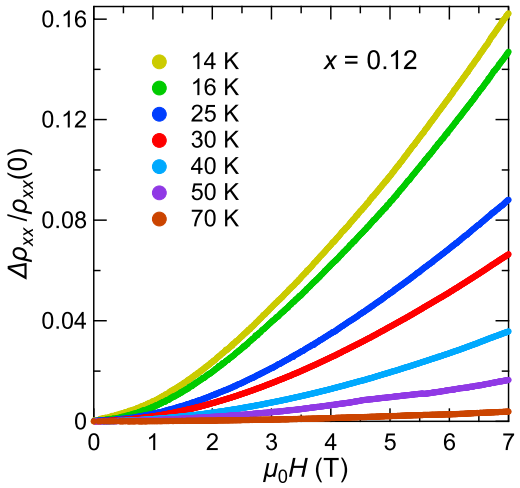

Figure 4.9: Field dependence of the transverse magnetoresistance $\Delta\rho_{xx}/\rho_{xx}(0)$ for $x = 0.12$ at different temperatures.

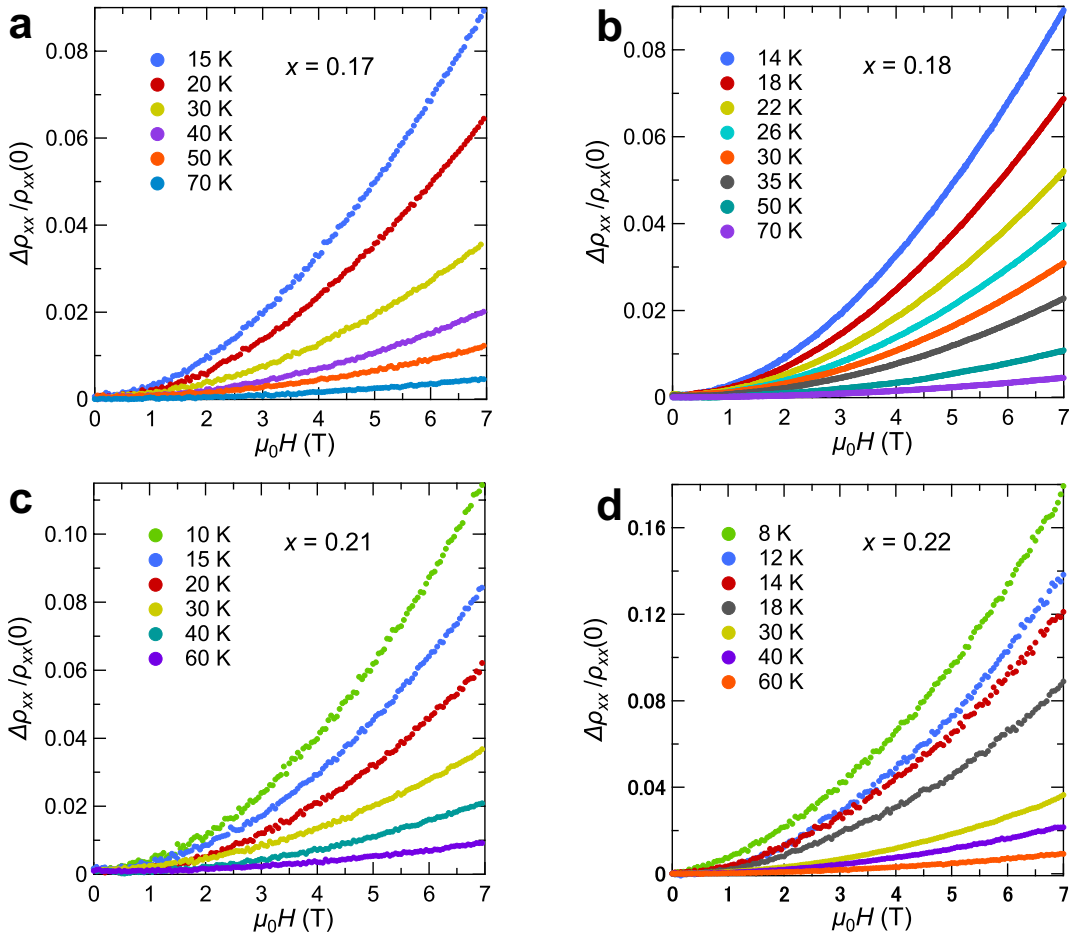

Figure 4.10: Field dependence of the transverse magnetoresistance $\Delta\rho_{xx}/\rho_{xx}(0)$ for $x =$ **a** 0.17, **b** 0.18, **c** 0.21, and **d** 0.22.

For the nematic sample ($x = 0.12$), the magnetoresistance curves fall on a single curve below 25 K, which means the Kohler's rule is obeyed. However, at higher temperatures, the magnetoresistance curves become different, which means the Kohler's rule is not obeyed.

For the tetragonal samples near the nematic QCP ($x = 0.17$ and 0.18), the distinct magnetoresistance curves with different temperatures are clearly shown, which indicates the violation of Kohler's rule. For samples with a higher S concentration ($x = 0.21$ and 0.22), the Kohler's rule holds at above 30 K, implying that the magnetoresistance is dominated by a single scattering time.

It should be noted that the violation of Kohler's rule here cannot be viewed as a definite evidence of the anomalous transport behavior. This is because the S-doped FeSe is a multiband material, and Kohler's rule cannot be held even in conventional metals if the scattering time is band-dependent. Thus, it is necessary to search for a new scaling law.

4.3.3 Modified Kohler's plot

As mentioned previously, in certain strongly correlated materials, the magnetoresistance cannot be scaled by Kohler's rule and a new scaling relationship called modified Kohler's rule, i.e., $\Delta\rho_{xx}/\rho_{xx}(0) \propto \tan^2\theta_{\mathrm{H}}$, has been observed. Herein, to investigate whether this modified Kohler's scaling is valid in our system, we plot the magnetoresistance as a function of $\tan^2\theta_{\mathrm{H}}$ for various x, as shown in Figs. 4.13 and 4.14.

For the sample with $x = 0.12$, it is clear that the magnetoresistance cannot be scaled by $\tan^2\theta_{\mathrm{H}}$ in the nematic phase. By contrast, for the samples with $x = 0.17$ and 0.18, the positions of which are near the nematic QCP, the magnetoresistance curves collapse onto one straight line of below 40 K, indicating the validation of the modified Kohler's scaling. At above 40 K, the slope of the curves increases with increasing temperature, which indicates that modified Kohler's scaling is invalid. For the higher S-doping sample with $x = 0.21$, the modified Kohler's scaling is valid within a narrower temperature range of below 30 K. For $x = 0.22$, the magnetoresistance curves can be

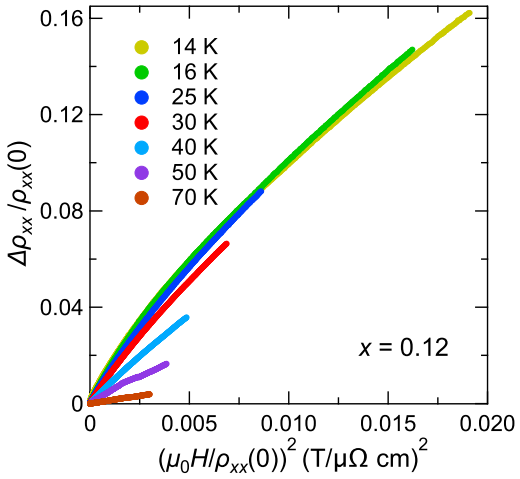

Figure 4.11: Kohler's plot for $x = 0.12$ at different temperatures [93].

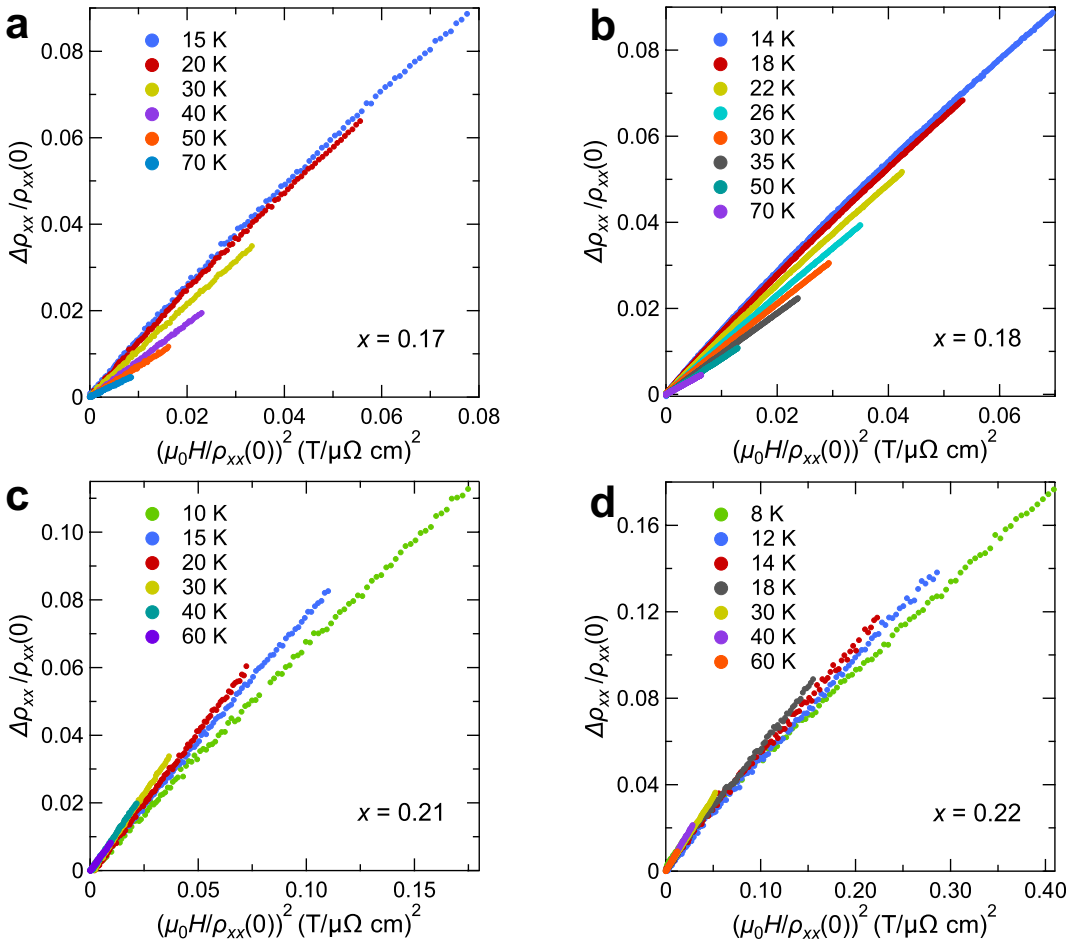

Figure 4.12: Kohler's plot for $x =$ **a** 0.17, **b** 0.18, **c** 0.21 and **d** 0.22 [93].

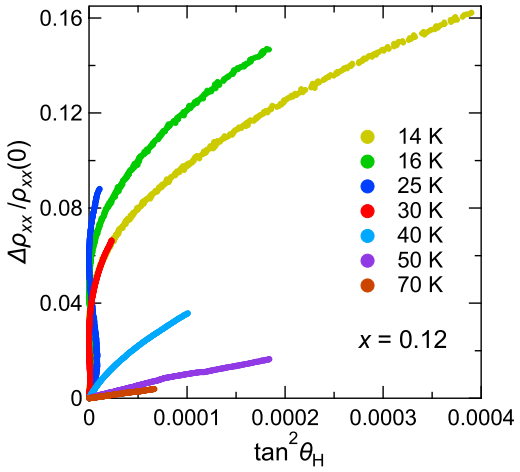

Figure 4.13: Magnetoresistance $\Delta\rho_{xx}/\rho_{xx}(0)$ plotted as a function of $\tan^2\theta_H$ for $x = 0.12$ at below 70 K [93].

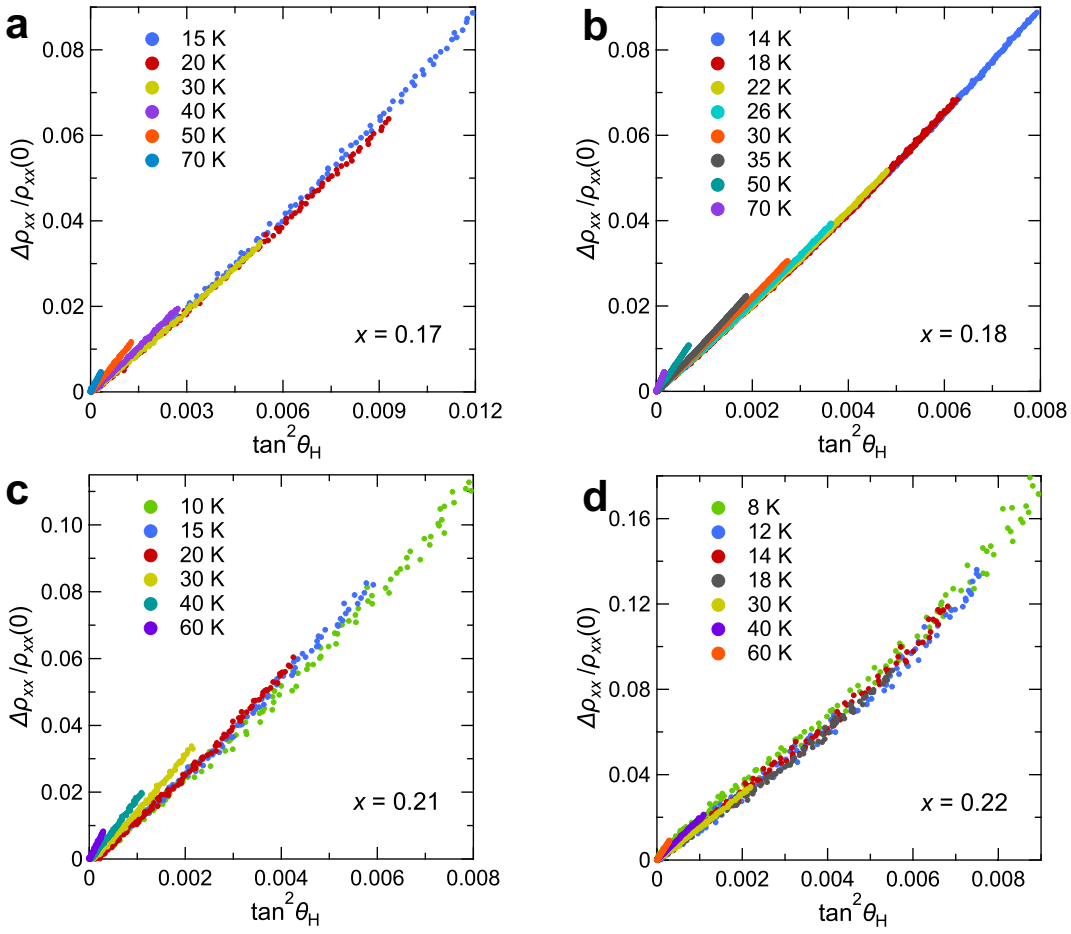

Figure 4.14: Magnetoresistance $\Delta\rho_{xx}/\rho_{xx}(0)$ plotted as a function of $\tan^2\theta_H$ for $x =$ **a** 0.17, **b** 0.18, **c** 0.21 and **d** 0.22 [93].

scaled as a function of $\tan^2\theta_H$ at below 30 K, whereas the curves are slightly non-linear in $\tan^2\theta_H$.

The observation of the modified Kohler's scaling at below 40 K for $x = 0.17$ and 0.18 is unexpected and possibly provides evidence of the anomaly in the magnetoresistance when combined with the violation of Kohler's rule. Another important point is that, within the same temperature range of below 40 K, we also observed the linear-in-temperature resistivity and the quadratic temperature dependent $\cot\theta_H$. As discussed in the next section, this set of transport properties cannot be described using a compensated two-band model, implying the charge anomaly observed.

4.4 Possible origin of the anomalous transport properties

In previous sections, we show the transport results across the nematic QCP in $FeSe_{1-x}S_x$. Herein, we highlight a set of anomalous transport behaviors observed at below 40 K within the vicinity of nematic QCP ($x \sim 0.17$):

- The zero-field resistivity shows a linear temperature dependence, the scattering rate of which is estimated to be close to the Planckian limit.
- The value of $\cot\theta_H$ shows a quadratic temperature dependence.
- The magnetoresistance violates Kohler's scaling. Instead, it obeys the modified Kohler's rule.

In this section, the possible interpretation for this set of transport results is discussed.

4.4.1 Multiband effect

Because S-doped FeSe is a compensated multi-band material, one might consider the multiband effect to be the origin of the anomalous transport properties. To check this possibility, the calculation based on the compensated two band model was conducted

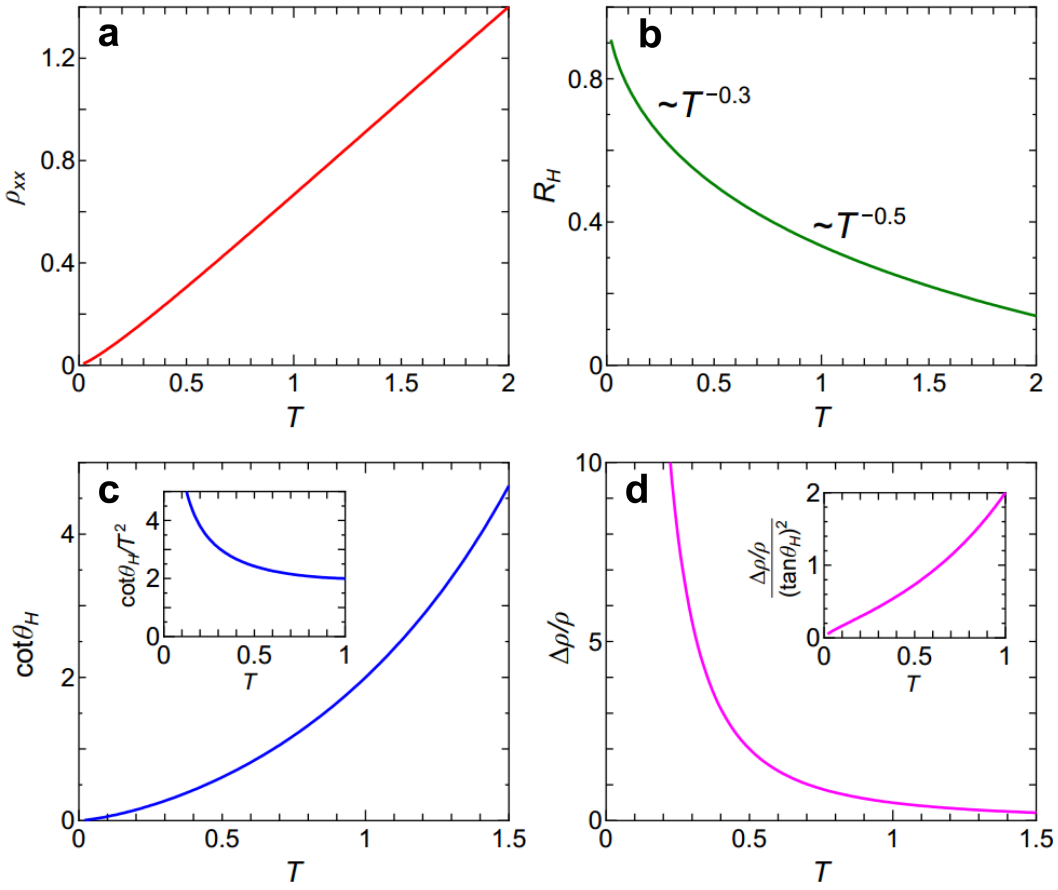

Figure 4.15: Transport coefficients calculated using compensated two-band model [93]. Temperature dependences of **a** zero-field resistivity ρ_{xx}, **b** Hall coefficient $R_{\rm H}$, **c** cotangent of the Hall angle $\cot\theta_{\rm H}$, and **d** magnetoresistance $\Delta\rho_{xx}/\rho_{xx}(0)$ are shown. The inset in panel **c** shows the plot of $\cot\theta_{\rm H}/T^2$ versus T. It is clear that $\cot\theta_{\rm H}$ is not T^2 dependence. The inset in panel **d** shows the temperature dependence of $\Delta\rho_{xx}/\rho_{xx}(0))/\tan^2\theta_{\rm H}$. The strong temperature dependence of $\Delta\rho_{xx}/\rho_{xx}(0))/\tan^2\theta_{\rm H}$ implies the violation of the modified Kohler's rule.

by our collaborator, Prof. Kontani. The results are summarized in Fig. 4.15. The details can be found in Ref. [93]. As shown in Fig. 4.15a and Fig. 4.15b, we obtain a T-linear profile of the zero-field resistivity ρ_{xx} and a low-temperature enhancement of Hall coefficient $R_{\rm H}$. However, the profile of $\cot\theta_{\rm H}$ shown in Fig. 4.15c is quantitatively different from the quadratic temperature dependence. This is apparent from the inset of Fig. 4.15c, where the strong temperature dependent $\cot\theta_{\rm H}/T^2$ is shown. Moreover, the magnetoresistance calculated from the same parameters (Fig. 4.15d) cannot be scaled

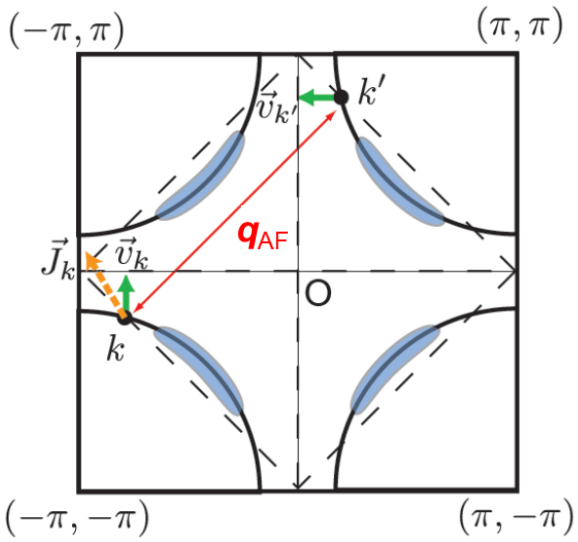

Figure 4.16: Schematic of the vertex correlations to the conductivity [77]. The two-dimensional Fermi surface shown here is typical for cuprates. Because the AFM fluctuations are peaked at the nesting wave vector $\boldsymbol{q}_{\mathrm{AF}}$, the Fermi surface spots with moment $\mathbf{k}$ and $\mathbf{k}'=\mathbf{k}+\boldsymbol{q}_{\mathrm{AF}}$ are strongly correlated. As a result, the Fermi velocity $\vec{v}_{\mathbf{k}}$ should be modified into $\vec{J}_{\mathbf{k}}$.

by $\tan^2\theta_{\mathrm{H}}$. Indeed, the temperature profile of the ratio $(\Delta\rho_{xx}/\rho_{xx}(0))/\tan^2\theta_{\mathrm{H}}$ (inset of Fig. 4.15d) deviates from the flat line, demonstrating the violation of the modified Kohler's rule. These calculated results have us believe that the experimentally observed transport behaviors within the vicinity of nematic QCP in $FeSe_{1-x}S_x$ cannot be simply attributed to the multiband effect.

4.4.2 Possible vertex corrections

Because the observed deviations from the Fermi liquid behavior are pronounced near the nematic QCP, we speculate that the nematic fluctuations can play an important role in the transport properties. However, it is difficult to tell what effect the nematic fluctuations can have on the charge transport properties. As mentioned previously, this set of anomalous transport behaviors has already been observed in cuprates, $CeMIn_5$ (M= Co and Rh) and iron-pnictides. Hence, it is natural to expect that the relevant theoretical scenarios proposed for these materials might be applied to our system.

Among others, one likely scenario is the vertex corrections to the conductivity [91, 92, 102]. This effect is briefly reviewed herein.

As described in Chapter 1, the quasiparticle energy with moment $\boldsymbol{k}$ depends not only on its renormalized single-particle energy $\epsilon_{\boldsymbol{k}}$, but also on the distribution of the other quasiparticles owing to the interaction, i.e.,

$$\tilde{\epsilon}_{\boldsymbol{k}} = \epsilon_{\boldsymbol{k}} + \sum_{\boldsymbol{k}'} f(\boldsymbol{k}, \boldsymbol{k}')\delta n_{\boldsymbol{k}'}, \tag{1.1}$$

where $\delta n_{\boldsymbol{k}} = n_{\boldsymbol{k}} - n^0_{\boldsymbol{k}}$ is the change in the distribution function with respect to the ground state and $f(\boldsymbol{k}, \boldsymbol{k}')$ is the effective two-particle interaction function. Based on Eq. 1.1, the current at each moment $\boldsymbol{k}$ can be calculated as follows:

$$\begin{aligned} \boldsymbol{J}_{\boldsymbol{k}} &= ne\nabla\tilde{\epsilon}_{\boldsymbol{k}} \\ &= ne\boldsymbol{v}_{\boldsymbol{k}} + neN(0)\int_{FS} dk'_{\parallel} f(\boldsymbol{k}, \boldsymbol{k}')\boldsymbol{v}_{\boldsymbol{k}'} \end{aligned} \tag{4.5}$$

where $\boldsymbol{v}_{\boldsymbol{k}} = \nabla\epsilon_{\boldsymbol{k}}$ is the carrier velocity, $N(0)$ is the density of states at the Fermi level. The second term is called a vertex correction. In the presence of large AFM fluctuations, $f(\boldsymbol{k}, \boldsymbol{k}')$ is proportional to the spin susceptibility $\chi(\boldsymbol{k} - \boldsymbol{k}')$, which peaked at the nesting vector $\boldsymbol{q}_{\mathrm{AF}}$. As a result, for the Fermi surface spots connected through $\boldsymbol{q}_{\mathrm{AF}}$, the second term in Eq. 4.5 cannot be ignored and is proportional to $\boldsymbol{v}_{\boldsymbol{k}+\boldsymbol{q}_{\mathrm{AF}}}$. Such a vertex correction can give rise to a T-linear resistivity, $\cot\theta_{\mathrm{H}} \propto T^2$ and modified Kohler's scaling of the magnetoresistance.

However, this scenario requires a finite value of $|\boldsymbol{q}_{\mathrm{AF}}|$. In the case of nematic fluctuations, $\boldsymbol{q}_{\mathrm{nem}} \approx 0$ as the order parameter preserves the transnational symmetry. Thus, it is an open question whether vertex corrections with $\boldsymbol{q}_{\mathrm{nem}} \approx 0$ can give rise to the observed anomalous transport behaviors. Further theoretical study is therefore needed.

5

Conclusion

In summary, we conducted resistivity, Hall effect, and magnetoresistance measurements for a series of $FeSe_{1-x}S_x$. We highlighted a set of transport behaviors observed at near $x_c = 0.17$: (i) The zero-field resistivity shows a linear dependence on temperature at well below the Fermi energy ($\sim$ 40 K). The associated scattering rate is close to the Planckian limit. (ii) Within the T-linear regime of resistivity, the cotangent of Hall angle $\cot\theta_{\mathrm{H}}$ ($=\rho_{xy}/\rho_{xx}$) is proportional to T^2. (iii) In the T-linear regime of resistivity, the magnetoresistance violates Kohler's rule. Instead, it can be scaled by the modified Kohler' s rule, i.e., $\Delta\rho_{xx}/\rho_{xx}(0) \propto \tan^2\theta_{\mathrm{H}}$. Because this set of transport behaviors are pronounced at near the nematic QCP and cannot be reproduced by the conventional compensated two-band model, we conclude that the critical nematic fluctuations are responsible for the observed behaviors.

Notably, these transport phenomena are similar to those reported in cuprate, iron-pnictide, and heavy fermion systems. However, in these cases, the possible origin has been discussed in terms of AFM fluctuations. Different from AFM fluctuations with finite momentum $\boldsymbol{q}_{\mathrm{AF}}$, the nematic fluctuations are peaked at $\boldsymbol{q}_{\mathrm{nem}} \approx 0$. Further theoretical work is needed to clarify how the $\boldsymbol{q}_{\mathrm{nem}} \approx 0$ fluctuations lead to the observed NFL behaviors. Our results suggest that different types of quantum fluctuations might result in the same anomalous charge transport behaviors.

References

[1] L. Landau, J. Exp. Theor. Phys. **30**, 1058 (1956).

[2] P. W. Anderson, *Basic Notions of Condensed Matter Physics* (Benjamin/Cummings, 1984).

[3] A. J. Schofield, Contemp. Phys. **40**, 95–115 (1999).

[4] H. v. Löhneysen, A. Rosch, M. Vojta, and P. Wölfle, Rev. Mod. Phys. **79**, 1015–1075 (2007).

[5] T. Shibauchi, A. Carrington, and Y. Matsuda, Annu. Rev. Condens. Matter Phys. **5**, 113–135 (2014).

[6] P. Coleman and A. J. Schofield, Nature **433**, 226–229 (2005).

[7] S. Sachdev and B. Keimer, Phys. Today **64**, 29–35 (2011).

[8] S. Sachdev, *Quantum Phase Transitions* (Cambridge University Press, 2011).

[9] T. Park, F. Ronning, H. Q. Yuan, M. B. Salamon, R. Movshovich, J. L. Sarrao, and J. D. Thompson, Nature **440**, 65–68 (2006).

[10] C. M. Varma, Rev. Mod. Phys. **92**, 031001 (2020).

[11] Y. Sato, S. Kasahara, T. Taniguchi, X. Xing, Y. Kasahara, Y. Tokiwa, Y. Yamakawa, H. Kontani, T. Shibauchi, and Y. Matsuda, Proc. Natl. Acad. Sci. **115**, 1227–1231 (2018).

[12] Y. Kamihara, H. Hiramatsu, M. Hirano, R. Kawamura, H. Yanagi, T. Kamiya, and H. Hosono, J. Am. Chem. Soc. **128**, 10012–10013 (2006).

[13] A. Chubukov and P. J. Hirschfeld, Phys. Today **68**, 46–52 (2015).

[14] M. Yi, Y. Zhang, Z.-X. Shen, and D. Lu, npj Quantum Mater. **2**, 57 (2017).

[15] V. Cvetkovic and Z. Tesanovic, Europhys. Lett. **85**, 37002 (2009).

[16] P. J. Hirschfeld, M. M. Korshunov, and I. I. Mazin, Rep. Prog. Phys. **74**, 124508 (2011).

[17] R. M. Fernandes and A. V. Chubukov, Rep. Prog. Phys. **80**, 014503 (2017).

[18] I. R. Fisher, L. Degiorgi, and Z. X. Shen, Rep. Prog. Phys. **74**, 124506 (2011).

[19] T.-M. Chuang, M. P. Allan, J. Lee, Y. Xie, N. Ni, S. L. Bud'ko, G. S. Boebinger, P. C. Canfield, and J. C. Davis, Science **327**, 181–184 (2010).

[20] S. Kasahara, H. J. Shi, K. Hashimoto, S. Tonegawa, Y. Mizukami, T. Shibauchi, K. Sugimoto, T. Fukuda, T. Terashima, A. H. Nevidomskyy, and Y. Matsuda, Nature **486**, 382–385 (2012).

[21] R. M. Fernandes and J. Schmalian, Supercond. Sci. Technol. **25**, 084005 (2012).

[22] R. M. Fernandes, A. V. Chubukov, and J. Schmalian, Nat. Phys. **10**, 97–104 (2014).

[23] A. V. Chubukov, M. Khodas, and R. M. Fernandes, Phys. Rev. X **6**, 041045 (2016).

[24] S. Onari and H. Kontani, Phys. Rev. Lett. **109**, 137001 (2012).

[25] S.-H. Baek, D. V. Efremov, J. M. Ok, J. S. Kim, J. van den Brink, and B. Büchner, Nat. Mater. **14**, 210–214 (2015).

[26] H. Kontani and S. Onari, Phys. Rev. Lett. **104**, 157001 (2010).

[27] F.-C. Hsu, J.-Y. Luo, K.-W. Yeh, T.-K. Chen, T.-W. Huang, P. M. Wu, Y.-C. Lee, Y.-L. Huang, Y.-Y. Chu, D.-C. Yan, and M.-K. Wu, Proc. Natl. Acad. Sci. **105**, 14262–14264 (2008).

[28] A. E. Böhmer and A. Kreisel, J. Phys.: Condens. Matter **30**, 023001 (2018).

[29] S. Margadonna, Y. Takabayashi, M. T. McDonald, K. Kasperkiewicz, Y. Mizuguchi, Y. Takano, A. N. Fitch, E. Suard, and K. Prassides, Chem. Commun., 5607–5609 (2008).

[30] S. Kasahara, T. Watashige, T. Hanaguri, Y. Kohsaka, T. Yamashita, Y. Shimoyama, Y. Mizukami, R. Endo, H. Ikeda, K. Aoyama, T. Terashima, S. Uji, T. Wolf, H. von Löhneysen, T. Shibauchi, and Y. Matsuda, Proc. Natl. Acad. Sci. **111**, 16309–16313 (2014).

[31] M. D. Watson, T. K. Kim, L. C. Rhodes, M. Eschrig, M. Hoesch, A. A. Haghighirad, and A. I. Coldea, Phys. Rev. B **94**, 201107 (2016).

[32] M. D. Watson, T. Yamashita, S. Kasahara, W. Knafo, M. Nardone, J. Béard, F. Hardy, A. McCollam, A. Narayanan, S. F. Blake, T. Wolf, A. A. Haghighirad, C. Meingast, A. J. Schofield, H. v. Löhneysen, Y. Matsuda, A. I. Coldea, and T. Shibauchi, Phys. Rev. Lett. **115**, 027006 (2015).

[33] M. Yi, H. Pfau, Y. Zhang, Y. He, H. Wu, T. Chen, Z. R. Ye, M. Hashimoto, R. Yu, Q. Si, D.-H. Lee, P. Dai, Z.-X. Shen, D. H. Lu, and R. J. Birgeneau, Phys. Rev. X **9**, 041049 (2019).

[34] M. D. Watson, A. A. Haghighirad, L. C. Rhodes, M. Hoesch, and T. K. Kim, New J. Phys. **19**, 103021 (2017).

[35] Y. Suzuki, T. Shimojima, T. Sonobe, A. Nakamura, M. Sakano, H. Tsuji, J. Omachi, K. Yoshioka, M. Kuwata-Gonokami, T. Watashige, R. Kobayashi, S. Kasahara, T. Shibauchi, Y. Matsuda, Y. Yamakawa, H. Kontani, and K. Ishizaka, Phys. Rev. B **92**, 205117 (2015).

[36] S. Onari, Y. Yamakawa, and H. Kontani, Phys. Rev. Lett. **116**, 227001 (2016).

[37] A. I. Coldea and M. D. Watson, Annu. Rev. Condens. Matter Phys. **9**, 125–146 (2018).

[38] T. Terashima, N. Kikugawa, A. Kiswandhi, E.-S. Choi, J. S. Brooks, S. Kasahara, T. Watashige, H. Ikeda, T. Shibauchi, Y. Matsuda, T. Wolf, A. E. Böhmer, F. Hardy, C. Meingast, H. v. Löhneysen, M.-T. Suzuki, R. Arita, and S. Uji, Phys. Rev. B **90**, 144517 (2014).

[39] S. Hosoi, K. Matsuura, K. Ishida, H. Wang, Y. Mizukami, T. Watashige, S. Kasahara, Y. Matsuda, and T. Shibauchi, Proc. Natl. Acad. Sci. **113**, 8139–8143 (2016).

[40] M. D. Watson, T. K. Kim, A. A. Haghighirad, N. R. Davies, A. McCollam, A. Narayanan, S. F. Blake, Y. L. Chen, S. Ghannadzadeh, A. J. Schofield, M. Hoesch, C. Meingast, T. Wolf, and A. I. Coldea, Phys. Rev. B **91**, 155106 (2015).

[41] A. E. Böhmer, T. Arai, F. Hardy, T. Hattori, T. Iye, T. Wolf, H. v. Löhneysen, K. Ishida, and C. Meingast, Phys. Rev. Lett. **114**, 027001 (2015).

[42] P. Massat, D. Farina, I. Paul, S. Karlsson, P. Strobel, P. Toulemonde, M.-A. Méasson, M. Cazayous, A. Sacuto, S. Kasahara, T. Shibauchi, Y. Matsuda, and Y. Gallais, Proc. Natl. Acad. Sci. **113**, 9177–9181 (2016).

[43] J.-H. Chu, H.-H. Kuo, J. G. Analytis, and I. R. Fisher, Science **337**, 710–712 (2012).

[44] T. Shimojima, Y. Suzuki, T. Sonobe, A. Nakamura, M. Sakano, J. Omachi, K. Yoshioka, M. Kuwata-Gonokami, K. Ono, H. Kumigashira, A. E. Böhmer, F. Hardy, T. Wolf, C. Meingast, H. v. Löhneysen, H. Ikeda, and K. Ishizaka, Phys. Rev. B **90**, 121111 (2014).

[45] J. P. Sun, K. Matsuura, G. Z. Ye, Y. Mizukami, M. Shimozawa, K. Matsubayashi, M. Yamashita, T. Watashige, S. Kasahara, Y. Matsuda, J. .-Q. Yan, B. C. Sales, Y. Uwatoko, J. .-G. Cheng, and T. Shibauchi, Nat. Commun. **7**, 12146 (2016).

[46] T. Imai, K. Ahilan, F. L. Ning, T. M. McQueen, and R. J. Cava, Phys. Rev. Lett. **102**, 177005 (2009).

[47] T. Hanaguri, S. Kasahara, J. Böker, I. Eremin, T. Shibauchi, and Y. Matsuda, Phys. Rev. Lett. **122**, 077001 (2019).

[48] C.-L. Song, Y.-L. Wang, P. Cheng, Y.-P. Jiang, W. Li, T. Zhang, Z. Li, K. He, L. Wang, J.-F. Jia, H.-H. Hung, C. Wu, X. Ma, X. Chen, and Q.-K. Xue, Science **332**, 1410–1413 (2011).

[49] H. Shakeripour, C. Petrovic, and L. Taillefer, New J. Phys. **11**, 055065 (2009).

[50] P. Bourgeois-Hope, S. Chi, D. A. Bonn, R. Liang, W. N. Hardy, T. Wolf, C. Meingast, N. Doiron-Leyraud, and L. Taillefer, Phys. Rev. Lett. **117**, 097003 (2016).

[51] P. O. Sprau, A. Kostin, A. Kreisel, A. E. Böhmer, V. Taufour, P. C. Canfield, S. Mukherjee, P. J. Hirschfeld, B. M. Andersen, and J. C. S. Davis, Science **357**, 75–80 (2017).

[52] L. Jiao, C.-L. Huang, S. Rößler, C. Koz, U. K. Rößler, U. Schwarz, and S. Wirth, Sci. Rep. **7**, 44024 (2017).

[53] T. Watashige, Y. Tsutsumi, T. Hanaguri, Y. Kohsaka, S. Kasahara, A. Furusaki, M. Sigrist, C. Meingast, T. Wolf, H. v. Löhneysen, T. Shibauchi, and Y. Matsuda, Phys. Rev. X **5**, 031022 (2015).

[54] T. Shibauchi, T. Hanaguri, and Y. Matsuda, J. Phys. Soc. Jpn. **89**, 102002 (2020).

[55] T. Hanaguri, K. Iwaya, Y. Kohsaka, T. Machida, T. Watashige, S. Kasahara, T. Shibauchi, and Y. Matsuda, Sci. Adv. **4**, eaar6419 (2018).

[56] A. I. Coldea, S. F. Blake, S. Kasahara, A. A. Haghighirad, M. D. Watson, W. Knafo, E. S. Choi, A. McCollam, P. Reiss, T. Yamashita, M. Bruma, S. C. Speller, Y. Matsuda, T. Wolf, T. Shibauchi, and A. J. Schofield, npj Quantum Mater. **4**, 2 (2019).

[57] P. Wiecki, K. Rana, A. E. Böhmer, Y. Lee, S. L. Bud'ko, P. C. Canfield, and Y. Furukawa, Phys. Rev. B **98**, 020507 (2018).

[58] K. Matsuura, Y. Mizukami, Y. Arai, Y. Sugimura, N. Maejima, A. Machida, T. Watanuki, T. Fukuda, T. Yajima, Z. Hiroi, K. Y. Yip, Y. C. Chan, Q. Niu, S. Hosoi, K. Ishida, K. Mukasa, S. Kasahara, J.-G. Cheng, S. K. Goh, Y. Matsuda, Y. Uwatoko, and T. Shibauchi, Nat. Commun. **8**, 1143 (2017).

[59] Y. Matsuda, K. Izawa, and I. Vekhter, J. Phys.: Condens. Matter **18**, R705–R752 (2006).

[60] S. Licciardello, J. Buhot, J. Lu, J. Ayres, S. Kasahara, Y. Matsuda, T. Shibauchi, and N. E. Hussey, Nature **567**, 213–217 (2019).

[61] S. Licciardello, N. Maksimovic, J. Ayres, J. Buhot, M. Čulo, B. Bryant, S. Kasahara, Y. Matsuda, T. Shibauchi, V. Nagarajan, J. G. Analytis, and N. E. Hussey, Phys. Rev. Res. **1**, 023011 (2019).

[62] M. Bristow, P. Reiss, A. A. Haghighirad, Z. Zajicek, S. J. Singh, T. Wolf, D. Graf, W. Knafo, A. McCollam, and A. I. Coldea, Phys. Rev. Res. **2**, 013309 (2020).

[63] E. Berg, S. Lederer, Y. Schattner, and S. Trebst, Annu. Rev. Condens. Matter Phys. **10**, 63–84 (2019).

[64] S. Lederer, Y. Schattner, E. Berg, and S. A. Kivelson, Proc. Natl. Acad. Sci. **114**, 4905–4910 (2017).

[65] J. M. Ziman, *Principles of the Theory of Solids* (Cambridge University Press, July 1972).

[66] C. Proust, B. Vignolle, J. Levallois, S. Adachi, and N. E. Hussey, Proc. Natl. Acad. Sci. **113**, 13654–13659 (2016).

[67] J. Paglione, "Quantum Criticality in the Heavy-Fermion Superconductor $CeCoIn_5$", PhD thesis (University of Toronto, 2005).

[68] X. Lin, B. Fauque, and K. Behnia, Science **349**, 945–948 (2015).

[69] J. C. Garland and R. Bowers, Phys. Kondens. Materie **9**, 36–44 (1969).

[70] H. K. Pal, V. I. Yudson, and D. L. Maslov, Lith. J. Phys. **52**, 142–164 (2012).

[71] N. W. Ashcroft and N. D. Mermin, *Solid State Physics* (Thomson Learning, 1976).

[72] Alfred Brian Pippard, *Magnetoresistance in Metals*, 1st edition (Cambridge University Press, 2009).

[73] A. P. Mackenzie, S. R. Julian, D. C. Sinclair, and C. T. Lin, Phys. Rev. B **53**, 5848–5855 (1996).

[74] M. Gurvitch and A. T. Fiory, Phys. Rev. Lett. **59**, 1337–1340 (1987).

[75] J. Tahir-Kheli, New J. Phys. **15**, 073020 (2013).

[76] S. Kasahara, T. Shibauchi, K. Hashimoto, K. Ikada, S. Tonegawa, R. Okazaki, H. Shishido, H. Ikeda, H. Takeya, K. Hirata, T. Terashima, and Y. Matsuda, Phys. Rev. B **81**, 184519 (2010).

[77] Y. Nakajima, H. Shishido, H. Nakai, T. Shibauchi, K. Behnia, K. Izawa, M. Hedo, Y. Uwatoko, T. Matsumoto, R. Settai, Y. Ōnuki, H. Kontani, and Y. Matsuda, J. Phys. Soc. Jpn. **76**, 024703 (2007).

[78] J. A. N. Bruin, H. Sakai, R. S. Perry, and A. P. Mackenzie, Science **339**, 804–807 (2013).

[79] J. Zaanen, Nature **430**, 512–513 (2004).

[80] A. Legros, S. Benhabib, W. Tabis, F. Laliberté, M. Dion, M. Lizaire, B. Vignolle, D. Vignolles, H. Raffy, Z. Z. Li, P. Auban-Senzier, N. Doiron-Leyraud, P. Fournier, D. Colson, L. Taillefer, and C. Proust, Nat. Phys. **15**, 142–147 (2019).

[81] M. V. Sadovskii, Phys.-Usp. **64**, 175 (2020).

[82] N. E. Hussey, J. Phys.: Condens. Matter **20**, 123201 (2008).

[83] H. Y. Hwang, B. Batlogg, H. Takagi, H. L. Kao, J. Kwo, R. J. Cava, J. J. Krajewski, and W. F. Peck, Phys. Rev. Lett. **72**, 2636–2639 (1994).

[84] I. M. Hayes, N. Maksimovic, G. N. Lopez, M. K. Chan, B. J. Ramshaw, R. D. McDonald, and J. G. Analytis, Nat. Phys. **17**, 58–62 (2020).

[85] T. Chien, Z. Wang, and N. Ong, Phys. Rev. Lett. **67**, 2088–2091 (1991).

[86] J. M. Harris, Y. F. Yan, P. Matl, N. P. Ong, P. W. Anderson, T. Kimura, and K. Kitazawa, Phys. Rev. Lett. **75**, 1391–1394 (1995).

[87] N. E. Hussey, J. R. Cooper, J. M. Wheatley, I. R. Fisher, A. Carrington, A. P. Mackenzie, C. T. Lin, and O. Milat, Phys. Rev. Lett. **76**, 122–125 (1996).

[88] P. Anderson, Phys. Rev. Lett. **67**, 2092–2094 (1991).

[89] R. Hlubina and T. M. Rice, Phys. Rev. B **51**, 9253–9260 (1995).

[90] N. Hussey, Eur. Phys. J. B **31**, 495–507 (2003).

[91] H. Kontani, K. Kanki, and K. Ueda, Phys. Rev. B **59**, 14723–14739 (1999).

[92] H. Kontani, Rep. Prog. Phys. **71**, 026501 (2008).

[93] W. K. Huang, S. Hosoi, M. Čulo, S. Kasahara, Y. Sato, K. Matsuura, Y. Mizukami, M. Berben, N. E. Hussey, H. Kontani, T. Shibauchi, and Y. Matsuda, Phys. Rev. Res. **2**, 033367 (2020).

[94] T. Urata, Y. Tanabe, K. K. Huynh, H. Oguro, K. Watanabe, and K. Tanigaki, arXiv:1608.01044v1.

[95] P. Reiss, M. D. Watson, T. K. Kim, A. A. Haghighirad, D. N. Woodruff, M. Bruma, S. J. Clarke, and A. I. Coldea, Phys. Rev. B **96**, 121103 (2017).

[96] M. D. Watson, T. K. Kim, A. A. Haghighirad, S. F. Blake, N. R. Davies, M. Hoesch, T. Wolf, and A. I. Coldea, Phys. Rev. B **92**, 121108 (2015).

[97] T. Hashimoto, Y. Ota, A. Tsuzuki, T. Nagashima, A. Fukushima, S. Kasahara, Y. Matsuda, K. Matsuura, Y. Mizukami, T. Shibauchi, S. Shin, and K. Okazaki, Sci. Adv. **6**, eabb9052 (2020).

[98] Y. Sun, S. Pyon, and T. Tamegai, Phys. Rev. B **93**, 104502 (2016).

[99] K. K. Huynh, Y. Tanabe, T. Urata, H. Oguro, S. Heguri, K. Watanabe, and K. Tanigaki, Phys. Rev. B **90**, 144516 (2014).

[100] S. Y. Tan, Y. Fang, D. H. Xie, W. Feng, C. H. P. Wen, Q. Song, Q. Y. Chen, W. Zhang, Y. Zhang, L. Z. Luo, B. P. Xie, X. C. Lai, and D. L. Feng, Phys. Rev. B **93**, 104513 (2016).

[101] Y. A. Ovchenkov, D. A. Chareev, V. A. Kulbachinskii, V. G. Kytin, D. E. Presnov, O. S. Volkova, and A. N. Vasiliev, Supercond. Sci. Technol. **30**, 035017 (2017).

[102] B. P. Stojkovic-acute and D. Pines, Phys. Rev. B **55**, 8576–8595 (1997).

Acknowledgements

Finally, I completed this study. At the end of the thesis, I would like to thank the people who helped me.

First and foremost, I would like to thank my advisor, Prof. Yuji Matsuda, for giving me the opportunity. Without his support, I cannot finish this work. I would also like to express my deep gratitude to Prof. Shigeru Kasahara. He taught me the experimental techniques and provided me with a lot of advice throughout the project. In addition, I have to thank Prof. Yuichi Kasahara. The discussion with him benefits me a lot.

I am also grateful to the collaborators related to this work for their experimental supports and helpful discussion. Namely, Prof. Takahito Terashima, Prof. Nigel Hussey, Prof. Hiroshi Kontani, Prof. Takasada Shibauchi, Dr. Suguru Hosoi, Dr. Matija Čulo, Dr. Kohei Matsuura, Dr. Yuta Mizukami and Dr. Maarten Berben.

Over the years, I have received a lot of help from many other researchers. They are Dr. Yuki Sato, Ms. Hinako Murayama, Dr. Xiangzhuo Xing, Dr. Masahiro Naritsuka and Dr. Shota Suetsugu.

I want to thank the current and former members of our group for the fun and games. Here, I mention Dr. Masahiro Haze, Mr. Tomohiro Ishii, Mr. Yohei Torii, Mr. Sohei Miyake, Mr. Hironori Hashimoto, Mr. Ma Sixiao, Ms. Tomoka Suematsu, Mr. Tomoya Taniguchi, Mr. Ryo Kurihara, Mr. Daiki Sano, Dr. Lang Peng, Mr. Takahiro Tominaga, Mr. Hiroki Suzuki, Mr. Takahito Ii, Mr. Andre de Oliveira Silva, Mr. Yuzuki Ukai, Mr. Taichi Yokoi, Mr. Takahiro Ono and Mr. Masaki Shimomura.

Besides, I thank my old friend Hengyue Li, whom I can confide in when I was depressed.

Lastly, thanks to my family for their support in every aspect of my life.

I want to acknowledge the financial support from China Scholarship Council.